9950-640

DOE/JPL-954685-81/5
Dist. Category UC-63

STUDY OF THE EFFECTS OF IMPURITIES ON THE PROPERTIES OF SILICON MATERIALS AND PERFORMANCE OF SILICON SOLAR CELL

FIFTH TECHNICAL REPORT
FINAL TECHNICAL REPORT

October 1981

By C. T. Sah

Contract No. 954685

The JPL Flat-Plate Solar Array (FSA) Project is sponsered by the U. S. Department of Energy and forms a part of the Solar Photovoltaic Conversion Program to initiate a major effort toward the development of low-cost and high-efficiency solar arrays. This work was performed for the Jet Propulsion Laboratory, California Institute of Technology by agreement between NASA and DOE.

DOE/JPL-954685-81/2
Dist. Category UC-63

STUDY OF THE EFFECTS OF IMPURITIES ON THE PROPERTIES OF SILICON MATERIALS AND PERFORMANCE OF SILICON SOLAR CELL

FIFTH TECHNICAL REPORT
FINAL TECHNICAL REPORT

October 1981

By C. T. Sah

Contract No. 954685

The JPL Flat-Plate Solar Array (FSA) Project is sponsered by the U. S. Department of Energy and forms a part of the Solar Photovoltaic Conversion Program to initiate a major effort toward the development of low-cost and high-efficiency solar arrays. This work was performed for the Jet Propulsion Laboratory, California Institute of Technology by agreement between NASA and DOE.

TECHNICAL CONTENT STATEMENT

This report was prepared as an account of work sponsered by the United States Government. Neither the United States nor the United States Department of Energy, nor any of their employees, nor any of their contractors, sub-contractors, or their employees, makes any warranties, express or implied, or assumes any legal liability or responsibility for the accuracy, completeness or usefulness of any information, apparatus, product or process disclosed, or represents that its use would not infringe privately owned rights.

NEW TECHNOLOGY

No new technology is reportable for the period covered by this report.

TABLE OF CONTENT

LIST OF ILLUSTRATIONS

LIST OF TABLES

ABSTRACT

This fifth technical report, also the final report, covers studies on the effect of impurities and defects on the performance of silicon solar cells which were not reported in the previous four technical reports. It describes a theoretical study of the effect of defects across the back-surface-field junction on the performance of high-efficiency and thin solar cells, using a *developed-perimeter* device model for the three-dimensional defects. It shows that very significant degradation of open-circuit voltage can occur even if there are only a few defects distributed in the bulk of the solar cell. Two new features in the thickness dependences of the fill factor and efficiency in impurity-doped back-surface-field solar cells are discovered in the exact numerical solution which are associated with the high injection level effect in the base and not predicted by the low-level analytical theory. What are believed to be the most accurate recombination parameters at the Ti center to date are also given and a new theory is developed which is capable of distinguishing an acceptor-like deep level from a donor-like deep level using the measured values of the thermal emission and capture cross sections. Using the measured emission-capture cross section ratio, this theory can also provide information concerning the magnitude of the lattice distortion around an impurity atom before and after the capture or emission of an electron or a hole at the impurity center.

I. INTRODUCTION

The objective of this program is to determine the effects of impurities and defects on the performance and permanence of silicon solar cells. It includes theoretical (computer-aided-design techniques) and experimental studies of the effects of impurities on the electrical properties of silicon material intentionally doped with specific impurity elements, and the effects of these impurities on the impurity related energy level positions, the concentration of these energy levels and the recombination-generation-trapping rates of electrons and holes at these energy levels.

This technical report is the fifth of five annual reports and it is also the final report of this contract. Studies performed prior to the fourth technical report have been reported in the first four technical reports and the results have been submitted for publication or published in engineering journals. This report contains studies not reported in the previous four reports. Reference to the work of the earlier technical reports are made from time to time but no attempt is made to make a detailed review of these previous work since they are documented in the four previous reports and in open literature.

The first two chapters of this report (Chapter II and III) contain the results of a theoretical study of the effects of defects across the back-surface-field junction of high-efficiency thin-base silicon solar cells doped with recombination impurity elements. Since the geometry of the defect and its effect on the cell are three-dimensional which defy exact numerical or exact analytical solution, a departure from the exact transmission line method employed in the previous four reports has been undertaken. A developed perimeter device model is employed around the defective regions of the cell and one-dimensional low-level diffusion solutions of the dark current-voltage

characteristics are applied to the regions of cell of this model. A two-region model is developed for defects on the edge of the cell and a three-region model is developed for defects which are distributed in the bulk. Chapter II gives the results of the edge defects while chapter III gives the results of the bulk defects. It is shown in Chapter III that volume distributed bulk defects across the back-surface-field junction can seriously degrade or reduce the open circuit voltage of a high-efficiency thin cell even only a few defects are present. The edge defects have less degrading effect if the area is large or the area-to-circumference ratio is large. However, performance degradation due to bulk defects is relatively insensitive to the area of the cell and depends only on the areal density of the defect.

The third chapter of this report (Chapter IV) contains a short study of the effect of thickness on the solar cell performance parameters, the short-circuit current, the open-circuit voltage, the fill factor and the efficiency. The results were computed from the numerical solution of the Shockley Equations for one-dimensional cell structures with and without back-surface field, using the transmission line circuit model technique. New features in the thickness dependence of the fill factor and the efficiency are presented for thick and very thin cells which are related to high injection level and conductivity modulation conditions in the base region. These features were not observed in the thickness dependence curves given in Hovel's book which used the low-level analytical solution.

The fourth chapter of this report (Chapter V) contains a review of the literature data on the recombination-generation-trapping parameters of electrons and holes at the Ti center in silicon and also gives the latest and we feel to be the most reliable data on the majority carrier thermal emission and capture rates and thermal activation energies at the two Ti levels. A new theoretical

development is also presented to show how we can deduce the charge states or the acceptor-donor nature of the deep level using the measured nonequilibrium emission cross section and the measured equilibrium capture cross section of the majority carriers. It is shown that this emission-capture cross section ratio can also provide information on the lattice relaxation around the impurity atom and provide the configuration entropy in a situation where the emission cross section is nearly equal to its equilibrium value.

Plans are made to publish these four chapters as separate papers in open literature so that they are written as independent chapters with their own literature references and equation and figure numbering system.

II. REDUCTION OF SOLAR CELL EFFICIENCY BY EDGE DEFECTS ACROSS THE BACK-SURFACE-FIELD JUNCTION:- A DEVELOPED PERIMETER MODEL#

1. INTRODUCTION

Back-surface-field solar cell contains a high-low junction near the back surface. The potential barrier of the space-charge layer of this high-low junction prevents the emitter-junction-injected minority carrier from reaching the ohmic contact on the back surface. This greatly reduces the total base recombination current and gives a substantial increase of the open-circuit voltage over a comparable cell which has no back-surface-field high-low junction [1]. A typical result obtained using the computer-aided-design algorithm based on the transmission-line-circuit model is summarized in Table 1 [2]. It shows that the presence of the back-surface-field

TABLE 1 EFFECT OF BACK-SURFACE-FIELD ON SILICON SOLAR CELL PERFORMANCE AT ONE AM1 SUN AND 297°K.

Computer Run No.	Cell Type	Impurity Profiles[a]		VOC mV	JSC mA/cm^2	FF	EFF %
		Emitter	BSF				
RUN555	P+/N	$\exp(-X^2)$	none	554.11	32.456	0.8028	16.236
RUN335	P+/N/N+	$\exp(-X^2)$	$\exp(-X^2)$	672.32	33.954	0.7629	19.587

[a]Surface concentration=1.25×10^{20}, bulk concentration=$5\times10^{14}cm^{-3}$, thickness=300μm.

high-low junction, n/n+, on a p+/n junction silicon solar cell improves the open-circuit voltage by 672.32-554.11=118.21 mV or a factor of 672.32/554.11 =1.21. The AM1 peak efficiency, EFF, is also improved by this factor, from 16.236% to 19.587%. However, there is little increase of the short-circuit current, only 1.498 mA/cm^2 or 1.498/32/456=0.046 or 4.6%. This is expected since the cell thickness is kept constant in this comparison so that the

This chapter will be published in Solid-State Electronics, 1982 under the same title.

total absorption or photocurrent density is a constant. The fill factor is decreased slightly when the back surface field is added to the cell. This is due to the high-level effect or higher minority carrier concentration in the BSF cell than the non-BSF cell because the low/high or n/n+ junction reduces the minority carrier recombination rate, resulting in an increase of the minority carrier concentration in the base region of the p+/n/n+ cell.

In the above comparison, an ideal impurity diffusion profile, given by $\exp(-x^2/4Dt)$, is assumed for boron in the diffusion p+ emitter and also for phosphorus in the diffused n+ back surface field layer. More realistic diffusion profiles, such as $\exp(-x^6/L_1^6)$ for phosphorus and $[1 - (x/L_2)^{2/3}]$ for boron , which were used to study the effect of zinc recombination centers on silicon solar cell performance [2], do not change the conclusion that the BSF increases the open-circuit voltage substantially.

This dramatic improvement of the open-circuit voltage was first explained correctly in 1972 by Mandelkorn and Lamneck in series of experiments on silicon n+/p/p+ BSF cells whose top junction was made by phosphorus diffusion and whose BSF junction was made by alloying an evaporated layer of aluminum metal onto the back silicon surface [3]. A comprehensive theoretical analysis was then given by Godlewski, Baraona and Brandhorst in 1973 [1]. They employed the one-dimensional model and the analytical solution is based on constant impurity doping in each layer, low level condition (minority carrier concentration much smaller than the majority carrier or dopant impurity concentration) and finite surface recombination velocity at the metal-silicon interface on the back surface. In this n+/p/p+/m model for the experimental alloyed junction cells of Mandelkorn and Lamneck [3], the p+ layer contains two regions: the silicon regrowth layer which contains a high concentration of aluminum (7×10^{18} to 1×10^{19} Al/cm^3 from Al-Si phase diagram)

and an aluminum diffused silicon layer of about 1 μm thick from the 4-hour aluminum alloying at 800°C . The m layer is the aluminum-silicon alloy which contains about 12 atomic percent of silicon. The surface recombination velocity is that at the p+/m interface. It is evident that the Godlewski-Baraona-Brandhorst model is only an approximation to the alloyed BSF junction solar cell. The GBB model is also an approximate model for an all-diffused BSF cell in which both the n+ emitter and p+ back surface field layers are obtained by impurity diffusion.

An earlier analysis of the back surface field was made by R. N. Hall in 1953 [4] who called a n/n+ junction in a p+/n/n+ diode a donor contact. The earlier applications were mainly for power rectifiers where the BSF layer would reduce the series contact resistance, increase the base layer conductivity modulation by getting into high injection condition at lower forward bias, and decrease reverse leakage current.

In practice, the highest open-circuit voltage that has been obtained was from a silicon p+/n/n+ BSF cell made on 10 ohm-cm ($5x10^{14}$ cm^{-3}) float-zone silicon, reported by Fossum, Burgess and Nasby [5] in 1978. This cell has an open-circuit voltage of 622 mV, short-circuit current of 34.3 mA/cm^2, fill factor of 0.796 and efficiency of 16.8% under a 92.9 mW/cm^2 simulated AM1 solar illuminator. This experimental open-circuit voltage of 622 mV is substantially smaller than that predicted by the theory, 672 mV, shown in Table 1, Neither interband Auger recombination nor energy gap narrowing in the heavily doped emitter seem to be able to account for the entire 50 mV difference between theory and experiments.

For production n+/p/p+ back-surface-field silicon solar cells of high efficiency (14 to 16%), the open circuit voltage rarely exceeds 600 mV. For some of the earlier production cells, the back surface field p/p+ junction is

formed by aluminum alloying, similar to the method employed by Mandelkorn and Lamneck [3]. More recent BSF silicon cells are produced by diffusion.

A number of theoretical analyses has been advanced to account for the small experimental value of the open circuit voltage [6,7]. The general consensus is that in these high-efficiency silicon solar cells made on the high-resistivity base material (10 ohm-cm), base recombination rather than emitter recombination is the limiting factor. The dominance of base recombination would place further emphasis on the importance of employing the back-surface-field low-high junction to block the minority carriers from reaching the high-recombination-rate ohmic contact on the back surface of silicon. This importance of the BSF for the same reason is also evident for thin-film cells in space applications due to their power/weight ratio advantage and for terrestrial applications due to their potential low manufacturing costs.

The analyses made for the back-surface-field junction in the past have focused on an areally uniform BSF high-low junction. In the most general analysis made so far that has an explicit analytical solution, given by Godlewski, Baraona and Brandhorst [1], the ohmic contact on the back surface is represented by a surface recombination velocity and the p+ layer of the p/p+ junction is assumed to have a finite minority carrier lifetime. These realistic assumptions made the low-high junction not a perfect minority-carrier-reflecting potential barrier. However, the potential barrier of the low-high junction is usually several tenths of electron-volt or many kT/q. Such a 'high' potential barrier would reduce the effect of both the bulk recombination in the p+ layer as well as the surface recombination on the back surface. Thus, a well-designed and fabricated low-high junction would usually shield the minority carriers almost completely from these regions

of high recombination rates, the p+ layer and the p+/m interface.

This ideal areally homogeneous model for the BSF junction overlooks some very important defective conditions which invariably occur in production or even in experimental solar cells, due to cell geometry, material defects, as well as inhomogeneities. These defects are divided into two groups according to their locations and are illustrated in Fig. 1: (A) perimeter or edge defects and (B) bulk defects. The origin and causes of these defects are given below.

(A) Perimeter or Edge Defects

(1) Overflow of solder

(2) Imperfect perimeter surface etch

(3) Poor encapsulation

(B) Bulk Defects

(1) Poor alloying of the BSF junction

(2) Poor diffused BSF junction due to diffusion pipes

(3) Random back contact metal penetration

(4) Impurity segregation and cluster

These defects are electrical short circuits or resistive shunts across BSF junction. They can greatly reduce the effectiveness of the BSF potential barrier to shield the minority carriers from the recombination centers in the p+ region and on the p+/m interface.

These defects are even more detrimental to the cell performance if they appear across the front junction. However, their degradation influence on the front junction is well known and manufacturing procedures are developed to minimize their appearance across the front junction. Their influence on the performance of BSF junction have not been generally recognized nor analyzed.

In this paper, we shall analyze the effects of these electric defects across the BSF junction. We shall show that they can significantly reduce the

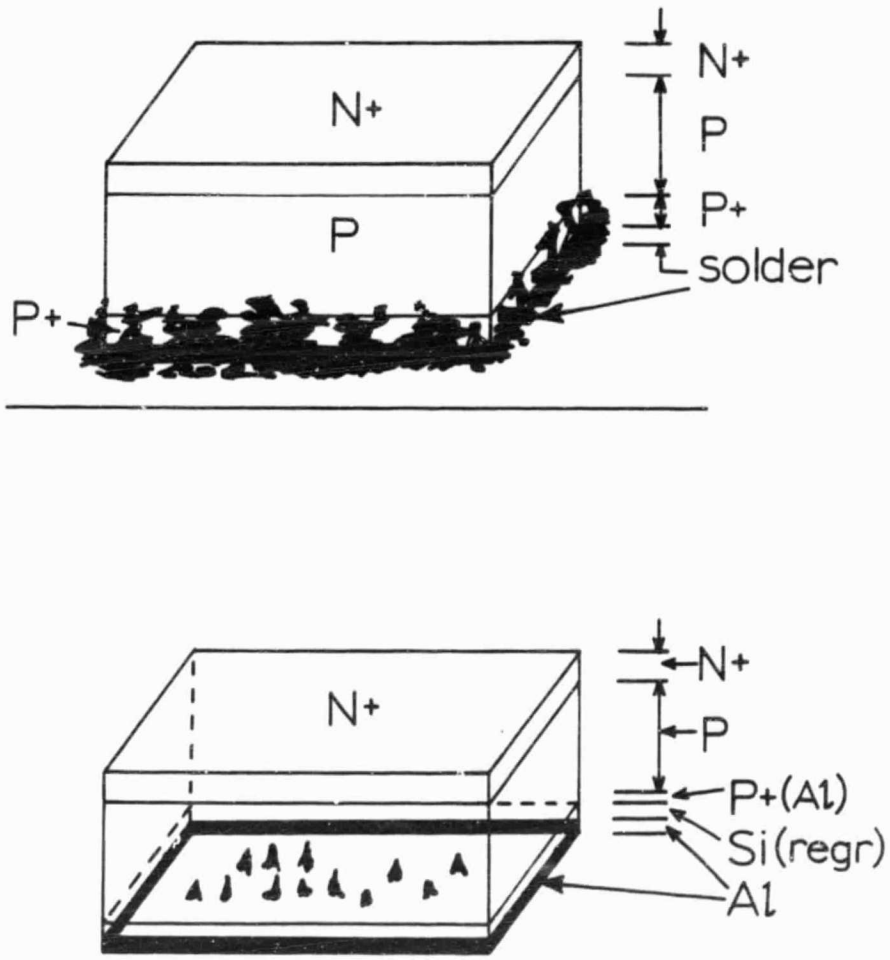

Fig. 1 (a) Edge and (b) bulk defects across the back-surface-field junction of a n+/p/p+ junction solar cell.

open-circuit voltage, hence the efficiency.

The device models used in this analysis are analytical models rather than the exact computer models since the localized defect problem is inherently a three-dimensional problem which cannot be solved exactly and numerically at present due to computer size and speed limitations. Although the models to be used are approximate one-dimensional analytical models, the results should provide accurate qualitative understanding and good quantitative estimate of the effects of defects on the solar-cell open-circuit voltage and performance.

Of the two locations of the defects, edge and bulk, the edge defects will be analyzed in this paper. Both a perfect short-circuit patch around the entire perimeter and an imperfect patch characterized by a finite surface recombination velocity will be analyzed. The second group of defects, present in the bulk, will be analyzed in a subsequent paper [8].

2. ENTIRE PERIMETER SHORT CIRCUITED - DEVICE MODEL AND ANALYSES

The back surface field is normally a very thin layer of about one micrometer thick fabricated either by aluminum alloying in earlier n+/p/p+ silicon cells or by diffusion in recent p+/n/n+ and n+/p/p+ silicon cells. The rather thin back surface-field layer is mainly from two reasons. It is fabricated at a low temprature (alloying at 800°C or diffusion at 900 to 1000°C) to preserve the minority carrier lifetime in the base region. This low temperature process gives a thin layer. The second reason is that the effectiveness of the low-high junction as a potential barrier for the emitter-injected minority carrier is the best when the low-high junction transition occurs in a very small distance or is very abrupt. This would mean that the n/n+ low-high junction should have a high impurity concentration in the n+ layer as well as a very thin space-charge layer to give a large and abrupt potential barrier across the n/n+ junction.

In practice, the perimeter of this thin back-surface-field layer can be short-circuited by the alloy used to solder the cell to a heat sink. Such a perimeter short-circuit can significantly reduce the open-circuit voltage since these shorts will substantially increase the minority carrier recombination current in the perimeter region. In this section, we shall treat the perimeter patch by a short-circuit so the perimeter of the cell is degraded from a p+/n/n+ diode to a p+/n diode. In a later section, a finite surface-recombination velocity will be used to characterize the perimeter shunt.

This is a two-dimensional problem if the cell is perfectly circular. It is a three-dimensional problem if the cell has a square, rectangular or other geometries. In the low-level and contant base-dopant-impurity concentration case, the analytical solutions in series forms can be obtained for the minoirty-carrier diffusion equation in the base region. However, the

analytical solutions cannot be extended to nor used for a cell with a random distribution of patchy defects across the perimeter or the bulk of its back-surface-field low-high junction. Thus, we shall use an approximate model by dividing a cell of arbitrary shape into two regions, the perimeter region and the central region and use the one-dimensional analytical solutions for these two regions.

Two examples of this two-region model are illustrated in Figure 2. One is the square cell and the other is the circular cell. The mathematical models of the two regions are as follows. The central region (Region I) is assumed to have the original p+/n/n+ BSF cell characteristics. The perimeter region (Region II) is assumed to experience the full influence of the short-circuit patch around the entire perimeter of the low-high junction due to soldering shorts or mechanical damage. This is the extreme or worst case of a defective perimeter cell. The intermediate case is modeled by a finite surface recombination velocity across the perimeter, analyzed in a later section.

From Fig. 2(b),it is evident that the perimeter region has a triangular cross section. The width of this triangular belt is assumed to be given by $\sqrt{L_I^2 - X_B^2}$ as indicated in Fig. 2(b). It is the width of the p/n junction of this perimeter region. Here, L_I is a few times of the base minority carrier diffusion length, $L_I = nL_B$ where $L_B = \sqrt{D_B \tau_B}$ is the minority carrier diffusion length whose diffusivity is D_B and lifetime τ_B. n is a number of the order of one and in the numerical solutions to be presented graphically, n is varied from 1 to 4 to show that its value does not have a large effect on the degradation of the open-circuit voltage. L_B would become the ambipolar diffusion length if we are in high injection level. X_B in Fig. 2(b) is the thickness of the base region and it is approximately the cell thickness since

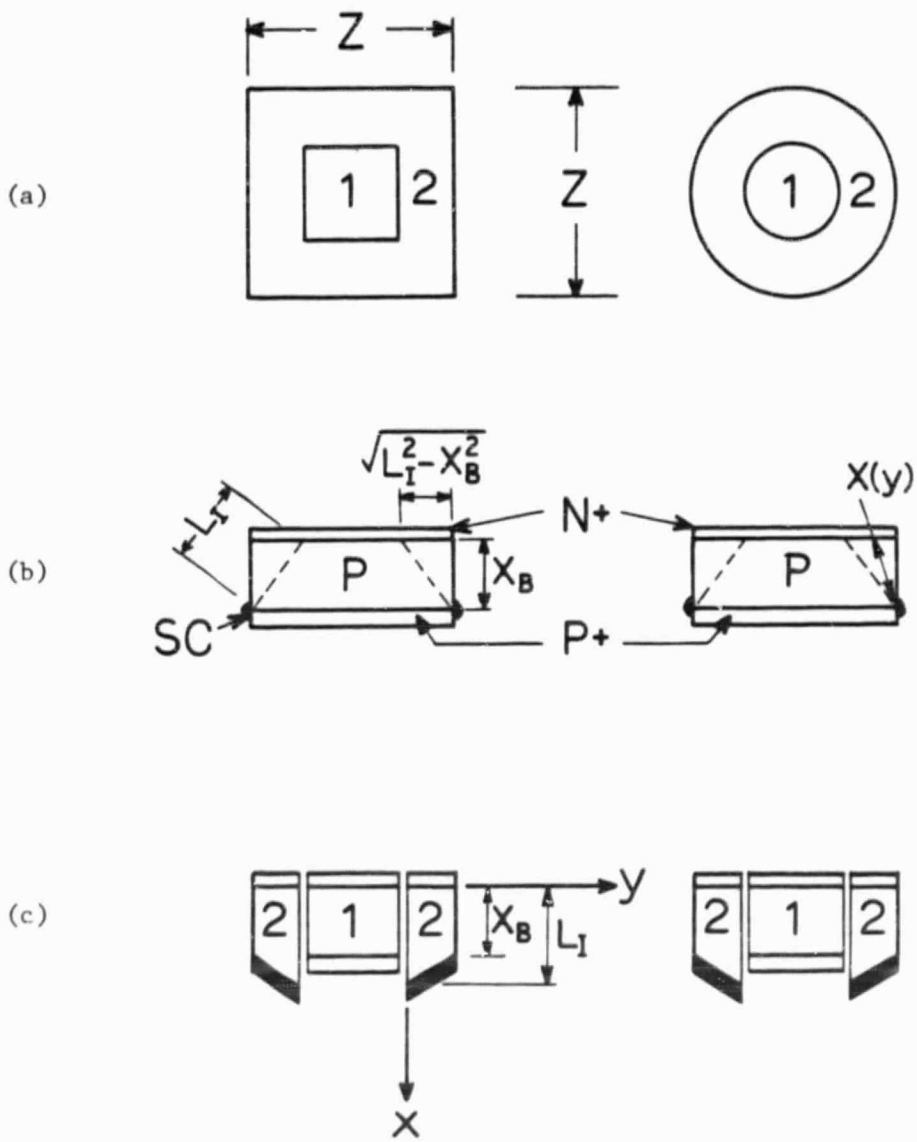

Fig 2 (a) The top view, (c) the cross sectional view and (c) the cross sectional view of the developed perimeter model of a n+/p/p+ back-surface-field solar cell with edge defect across the back-surface-field junction.

the diffused emitter and back-surface-field layers are usually very thin compared with the cell thickness.

The significance of L_I, which is the length of the side of the triangular cross section of the perimeter region as shown in Fig. 2(b), is as follows. All the minority carriers injected by the p/n junction will be influenced by the short-circuit at the defective perimeter if they are injected within a distance of L_I from the short-circuit. We call L_I the distance of influence or the range of the defect. A one-diffusion-length model is one with $n=1$ or $L_I=nL_B=L_B$. Using $n=1$ would underestimate the effect of the perimeter short-circuit since when the cell is thick or $X_B > L_I=L_B$, we will have no edge short-circuit effect even if the low-high junction around the cell perimeter is completely short-circuited. Thus, the one-diffusion-length model will provide a lower estimate of the degradation effect on the open-circuit voltage due to perimeter short-circuits.

The current-density equations for the minority carriers injected by the emitter junction in regions I and II, which are now treated as one-dimensional diodes, are the well-known Shockley diode equation at low injection level, modified by the effect of the ohmic (infinite surface recombination) short-circuit in region II or the back surface-field in region I. These are given by

$$J_I = q(D_B P_0/L_B)\tanh(X_B/L_B) \tag{1}$$

and

$$J_{II} = q(D_B P_0/L_B)\operatorname{ctnh}(X/L_B). \tag{2}$$

The symbols here follow the conventional usuage. $P_0=P_B[\exp(qV/kT)-1]$. q is the magnitude of the electron charge, k is the Boltzmann constant. T is the cell temperature, P_B is the minority carrier concentration in the uniformly doped base, and V is the terminal voltage or the difference between the quasi-Fermi or electrochemical potentials of holes and electrons across the emitter-junction space-charge layer.

X_B is the base layer thickness. X is the distance between an elemental junction area in Region II and the nearest short-circuit point at the perimeter as shown on the right cross-sectional picture in Fig. 2(b). Thus, Region II has an effective variable base layer thickness, X(y), where y is a direction in the plane of the p/n junction.

The current density of Region I, given by Equation (1), assumes that the low-high junction is perfectly minority-carrier-reflecting, that is, it has an infinite potential barrier height so that no minority carriers can cross this low-high junction boundary. This assumption is an excellent approximation for all practical cases of well designed and carefully fabricated cells. Neither Fermi-Dirac statistics nor energy-gap narrowing in the diffused or alloyed p+ back-surface-field layer of a n+/p/p+ diode, or in the n+ diffused BSF layer of p+/n/n+ diode, can change the numerical results given by Eq. (1) significantly. This can be demonstrated numerically by evaluating the more complete equation of J_I given by Godlewski, Baraona and Brandhorst [1] and assuming (i) a perfect ohmic contact (infinite surface recombination) on the back surface of the cell and (ii) as much as 100 mV reduction of the energy gap in the n+ or p+ region of the BSF layer.

The total diode current from the two regions are obtained by integrating the current densities, Equations (1) and (2), over the cross-sectional areas of the two regions. With the aid of Figs. 2(a) and 2(b), they are given by

$$I_1 = q(D_B P_0/L_B)\tanh(X_B/L_B)A_1 \tag{3}$$

and

$$I_2 = q(D_B P_0/L_B)\int_0^{\sqrt{L_I^2-X_B^2}} \operatorname{ctnh}(X/L_B)dx\ Z_{II} \tag{4}$$

The symbols used here were defined after Equations (1) and (2).

The current in Region I, given by Equation (3), is just the current density, J_I, times the area of Region I, A_1.

The current in Region II is given by Equation (4) where Z_{II} is the effective length of the circumference of the perimeter region which is defined by the area of Region II after Equation (4) is evaluated. For simple geometries such as the square and the circular cells, it can be obtained geometrically and is

$$Z_{II} = 4(Z - \sqrt{L_I^2 - X_B^2}) \tag{5}$$

for a square cell and

$$Z_{II} = (D - \sqrt{L_I^2 - X_B^2}) \tag{6}$$

for a circular cell. Here, Z is the edge dimension of the square cell and D is the diameter of the circular cell.

The integral in Equation (4) can be evaluated numerically. Since the model is approximate and an one-dimensional approximation was already employed in the current densities given by Equations (1) and (2), the integral in Equation (4) is also evaluated approximately to give an analytical solution. To this aim, the triangular cross section of Region II is *unfolded* or *developed* into a trapezoidal cross section shown in Fig. 2(c). This is reminiscent of the developed helix model used in the early theory of helix traveling wave tubes [9]. The trapezoidal or linear transformation for region II is given by

$$X(y) \approx x = X_B + [(L_I - X_B)/\sqrt{L_I^2 - X_B^2}]y \tag{7}$$

which is used to evaluate the integral in Equation (4) in order to give an analytical solution. In the appendix, it is shown that the linear approximation gives numerical solutions which differ from the exact evaluation of the integral using the quadratic transformation, $X^2 = X_B^2 + y^2$, by less than 14%.

After regrouping terms and taking out the voltage dependent factor, $[\exp(qV/kT) - 1]$, the total current flowing in the these two regions are given by

$$I_1 = J_1 A_1 [\exp(qV/kT) - 1] \tag{8}$$

and

$$I_2 = J_2 A_2 [\exp(qV/kT) - 1] \tag{9}$$

Here, the current density coefficients are defined by

$$J_1 = (qD_BP_B/L_B)\tanh(X_B/L_B) \tag{10}$$

and

$$J_2 = [qD_BP_B/(L_I-X_B)]\ \log_e[\sinh(L_I/L_B)/\sinh(X_B/L_B)]. \tag{11}$$

The current flowing in an ideal cell without any edge short is given by

$$I_0 = J_1A_0[\exp(qV/kT) - 1]. \tag{12}$$

The areas, A_0, A_1 and A_2, are the total area and the area of regions I and II respectively. $A_0=A_1+A_2$. For a square cell, these are given by

$$A_0 = Z^2 \tag{13}$$

$$A_1 = (Z - 2\sqrt{L_I^2 - X_B^2})^2 \tag{14}$$

and

$$A_2 = \sqrt{L_I^2 - X_B^2}\ [4(Z - \sqrt{L_I^2 - X_B^2})]. \tag{15}$$

For a circular cell with diameter D, these areas are given by

$$A_0 = \pi D^2/4 \tag{16}$$

$$A_1 = \pi(D - 2\sqrt{L_I^2 - X_B^2})^2/4 \tag{17}$$

and

$$A_2 = \sqrt{L_I^2 - X_B^2}[\pi(D - \sqrt{L_I^2 - X_B^2})]. \tag{18}$$

Note that the area ratio, A_1/A_0, for the circuit and square cells are identical. This is also true for the area ratio A_2/A_0.

The degradation of the open-circuit voltage, $-\Delta V_{OC}$, can be computed by comparing the total current of a perfect cell, I_0, with the total current of a defective cell, $I_1 + I_2$. The result is independent of the cell operating condition or the magnitude of the open-circuit voltage if the open-circuit voltage is large compared with kT/q or about 25 mV so that the approximation, $[\exp(qV/kT) - 1] \simeq \exp(qV/kT)$, is accurate. For a photocurrent or short-circuit current of I_L from the solar illumination, the defective cell gives

$$I_L = I_1 + I_2 = (J_1A_1 + J_2A_2)\{\exp[q(V_{OC}+\Delta V_{OC})/kT] - 1\} \tag{19}$$

and the perfect cell gives

$$I_L = I_0 = J_0A_0\ \{\exp[q(V_{OC}/kT)] - 1\} \tag{20}$$

Dropping 1 compared with $\exp(qV_{OC}/kT)$ and eliminating V_{OC} between Equations (19) and (20), the reduction of the open-circuit voltage is then given by

$$- \Delta V_{OC} = (kT/q) \log_e[(A_1/A_0) + (J_2A_2/J_1A_0)] \qquad (21)$$

where J_1 and J_2 are given by Equations (10) and (11) and the areas are given by Equations (13) to (15) for the square cell and (16) to (18) for the circular or round cell.

As stated after Equation (18), the area ratios A_1/A_0 and A_2/A_1 are independent of whether the cell is square or round. Thus, the degradation of the open-circuit voltage, given by Equation (21), is the same for these two cell geometries using the developed perimeter model. However, we would expect V_{OC} degradation to have some dependences on the cell geometry in general but such differences are probably not very large for the perimeter or edge defects.

3. EFFECT OF THICKNESS IN PERIMETER DEFECTIVE CELLS

The analytical solution for the developed perimeter model just obtained provides a quantitative estimate of the importance of a short-circuiting defect across the entire perimeter of the BSF junction on the open-circuit voltage and cell performance. When the cell is thin compared with the diffusion length, $X_B << L_B$, the BSF layer gives a high V_{OC} compared with a cell without the BSF. Thus, we would expect the perimeter short-circuit to have a larger reduction of V_{OC} as the cell becomes thinner. From a simple geometrical consideration of Figure 2, it is also evident that V_{OC} reduction by edge defect is larger if the cell area is smaller or if the edge dimension Z or the diameter D is not much larger than the base minority carrier diffusion length, i.e., $Z \not\gg L_B$ or $D \not\gg L_B$. These are physically obvious conditions under which the perimeter short-circuit will give a large reduction of the open-circuit voltage. They may also be illustrated numerically by the following examples.

Consider an experimental cell of 1 cm^2 (Z=1cm or D=1cm) and L_B=1000 μm which is the order of that reported for the highest-V_{OC} diffused-silicon cell [5]. Let us also assume a cell thickness of 500 μm, then we have Z/L_B=10, X_B/L_B=0.5, A_1/A_0=0.6836, A_2/A_0=0.3164 and J_2/J_1=3.52 using (10) to (18). From (21), the computed open-circuit voltage reduction at 300°K is

$$- \Delta V_{OC} = (kT/q)\log_e(1.797) = 0.58(kT/q) = 15.2 \text{ mV}.$$

If the cell thickness is reduced to about 50 μm, which is approximately the optimum thickness for a thin BSF cell to get the maximum AM1 efficiency of about 17% [10], then X_B/L_B=0.05, Z/L_B=10, A_1/A_0=0.6404, A_2/A_0=0.3596 and J_2/J_1=63.19 using (10) to (18). From (21), the open-circuit voltage reduction would be increased to

$$- \Delta V_{OC} = (kT/q)\log_e(22.72) = 3.15(kT/q) = 81.46 \text{ mV}$$

at 300°K. This is quite a significant reduction or degradation of the open-circuit voltage by the presence of a defect.

To provide a rapid estimate of the effect of perimeter short-circuit, the amount of open-circuit voltage degradation is computed from Equation (21) and presented in Figure 3 (solid curves with L_I/L_B=1.0). The $- \Delta V_{OC}$ are given in mV at 297.15°K ($n_i=10^{10}$ cm^{-3} for Si) as a function of the normalized cell thickness, X_B/L_B (from 0.01 to 1, 2 or 4), and using the square root of the cell area or the cell linear dimension as the constant parameter (Z/L_B or D/L_B = 10 to 100). It is evident that the $- \Delta V_{OC}$ becomes more important in thinner cells.

The different choices of the distance-of-influence are also investigated. The results of $- \Delta V_{OC}$ with L_I/L_B=1 (solid curves), 2 and 4 (broken curves) are compared in Figure 3. It is evident from the three upper curves for Z/L_B=10 and the two lower curves for Z/L_B=100 that the choice of L_I have little effect in thin cells when $X_B/L_B \ll 1$. For thick cells or near $X_B/L_B \simeq 1$, using L_I/L_B=2 would give better estimate since L_I/L_B=1 gives zero ΔV_{OC}. However, in thick cells, ΔV_{OC} is small anyway as expected physically.

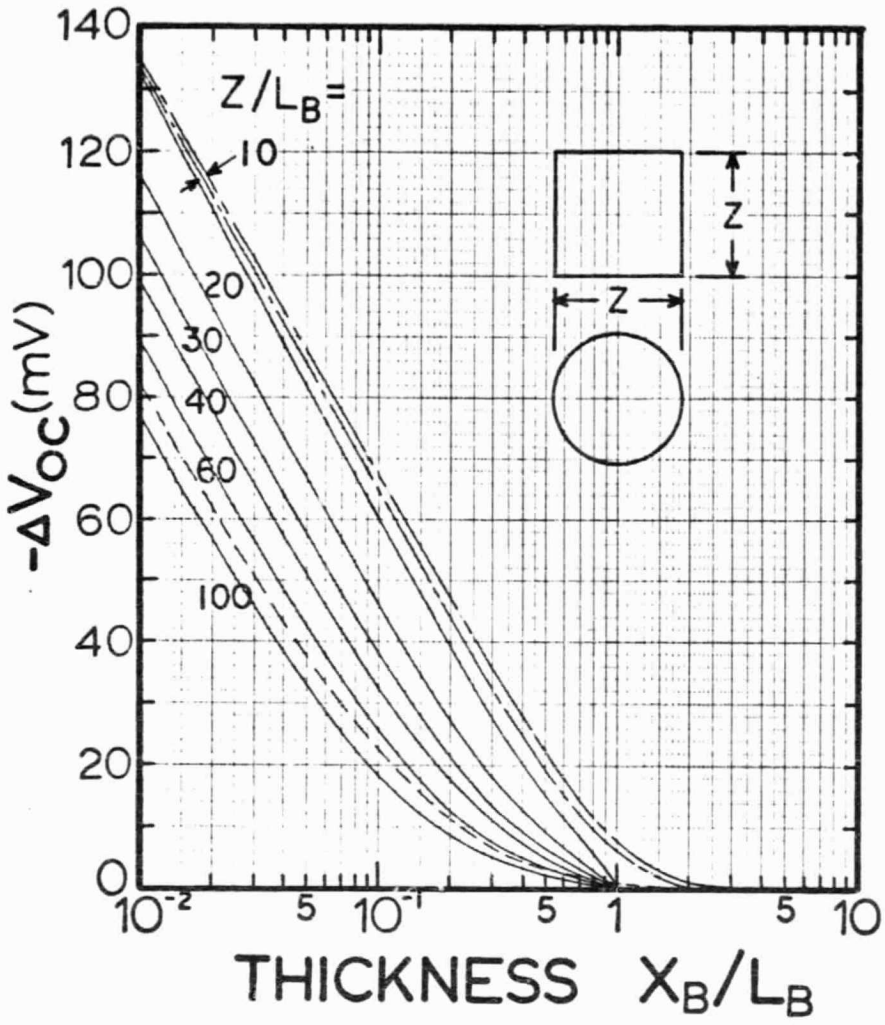

Fig. 3 The reduction of the open-circuit voltage as a function of the cell thickness of back-surface-field solar cells with edge defects across the BSF junction. The constant parameter is the cell diameter or cell edge normalized to base minority carrier diffusion length.

4. IMPERFECT EDGE SHORT CIRCUITS

The perfect short circuit across the entire perimeter of the low-high BSF junction, analyzed in the preceding section, can be extended to a more general situation in which the edge defect is not a zero-resistance or perfect short circuit but has a finite surface recombination velocity, to be denoted by S_D. The analyses just made for the perfect short circuit can be easily extended to this case using the two-region, one-dimensional analyses applied to the developed cell model. The solutions for the current density, J_1, and total current, I_1, are still given by Equations (1) or (10) and (3) or (8) respectively.

The solution for the perimeter region, Region II, given previously by Equations (2), (4), (9) and (11), needs to be modified. With a finite surface recombination velocity, S_D, the current density in the triangular region II is given by

$$J_{II} = q(D_B P_0/L_B) \frac{[\sinh(X/L_B) + (S_D L_B/D_B)\cosh(X/L_B)]}{[\cosh(X/L_B) + (S_D L_B/D_B)\sinh(X/L_B)]} \qquad (22)$$

which replaces Equation (2) and reduces to Equation (2) if $S_D=\infty$ for a perfect short circuit across the perimeter of the BSF low-high junction.

The ratio of the hyperbolic functions given in (22) replaces $\text{ctnh}(X/L_B)$ of Equation (4) and it can be integrated analytically since (22) is an exact differential if the linear transformation given by Equation (7) is used. The result can be put into the form of Equation (9) but the current density coefficient, J_2, is now given by

$$J_2 = [qD_B P_B/(L_I - X_B)] \log_e \left[\frac{\cosh(L_I/L_B) + (S_D L_B/D_B)\text{sihn}(L_I/L_B)}{\cosh(X_B/L_B) + (S_D L_B/D_B)\sinh(X_B/L_B)}\right] \qquad (23)$$

The asymptotic solution of J_2 given above for $S_D=\infty$ reduces to Equation (11), the correct asymptotic behavior. However, Equation (23) gives incorrect J_2 when $S_D=0$ since in this limit, $J_1=J_2$ and there is no open-circuit reduction. In order to

give the correct asymptotic solution at S_D=0, the cosh terms in Equation (23) are repalced by $\exp[(L_I/L_B)\tanh(X_B/L_B)]$ and $\exp[(X_B/L_B)\tanh(X_B/L_B)]$ so that

$$J_2 = [qD_BP_B/(L_2-X_B)] \log_e\left[\frac{\exp[(L_I/L_B)\tanh(X_B/L_B)] + (S_DL_B/D_B)\sinh(L_I/L_B)}{\exp[(X_B/L_B)\tanh(X_B/L_B)] + (S_DL_B/D_B)\sinh(X_B/L_B)}\right] \quad (24)$$

The reduction of the open-circuit voltage can now be computed from Equation (21) using J_1, A_0, A_1 and A_2 before and the new J_2 given by Equation (24). The normalized surface recombination velocity, S_DL_B/D_B, lies in the range of 10^{-2} to 10^3 since in practice, D_B=1 to 10 cm^2/sec and L_B=10^{-4} to 10^{-2} cm, while S_D=10^2 to 10^6 cm/sec. Thus, the diffusion velocity defined by D_B/L_B lies generally in the range of 10^3 to 10^4 cm/sec. Combining these with the extremes of S_D, we have $S_D/(D_B/L_B)$=$10^2/10^4$=10^{-2} at the lower end and $10^6/10^3$=10^3 at the upper end.

In Figure 4, the reduction of the open-circuit voltage is plotted as a function of cell thickness for a cell size of Z/L_B=10 and for surface recombination velocities of S_DL_B/D_B = ∞, 10^2, 10, 1, 10^{-1} and 0. This family of curves show that if the defect across the perimeter of the BSF junction is not a perfect short circuit, the open-circuit voltage reduction is decreased. As a numerical example, let D_B=10 cm^2/sec, L_B=10^{-1} cm and S_2=10^3 cm/sec. Then, the diffusion velocity is D_B/L_B=$10^2/10^{-1}$=10^3 cm/sec so that S_DL_B/D_B=1.0. For a cell of 100 μm thick, the open-circuit voltage is reduced by 32 mV by a imperfect perimeter defect compared with 60 mV if the defect is a perfect short circuit or S_D=∞.

The above example has a rather small area (A_0=Z^2= 1 cm^2) and Z/L_B=10. For a larger cell, the open-circuit voltage degradation by defective perimeter will be smaller. However, the degradation can be decreased by a factor of two if the surface recombination velocity is decreased from a nearly perfect short-circuit value of 10^6 cm/s to a medium value of 10^3 cm/s as indicated by the

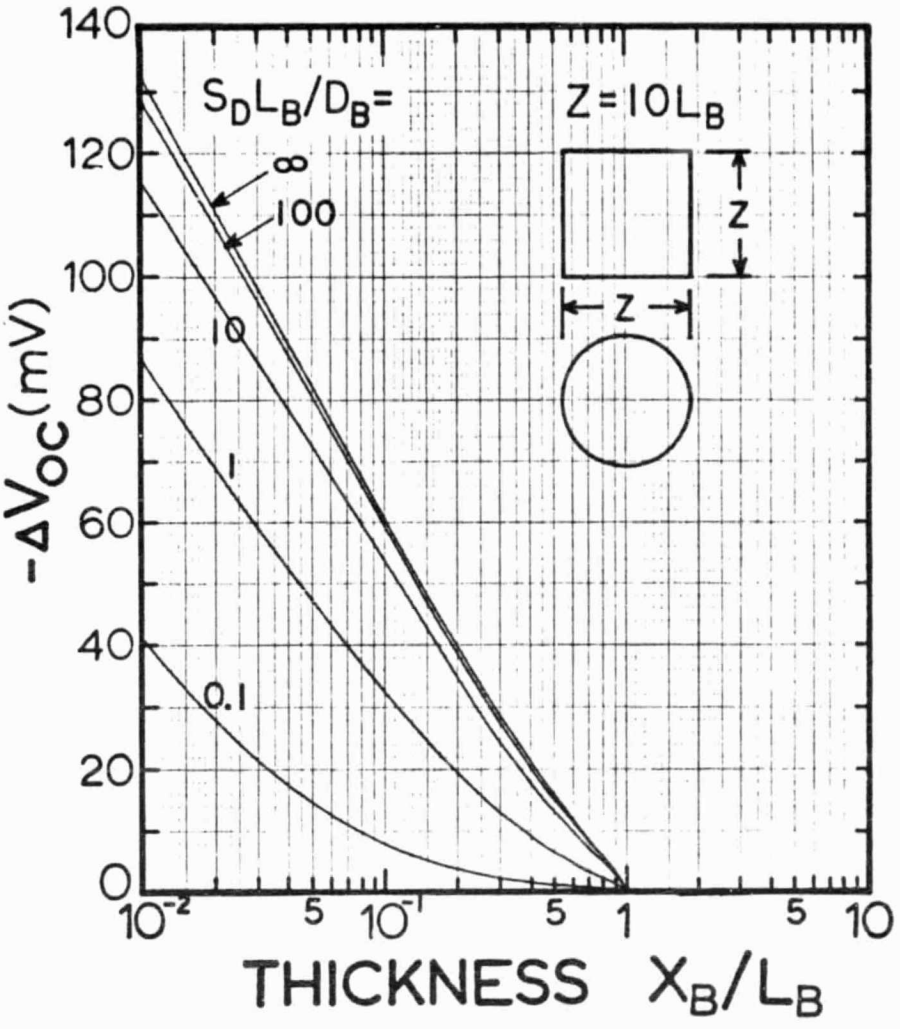

Fig. 4 The reduction of the open-circuit voltage as a function of the cell thickness of back-surface-field solar cells with imperfect edge defects across the BSF junction. The cell diameter or size is ten times the base minority carrier diffusion length. The constant parameter is the effective recombination velocity of the edge defect, S_D, normalized to the diffusion velocity of the minority carriers in the base, D_B/L_B.

two curves in Figure 4 with $S_D L_B/D_B = 1$ and 10^3 (between 10^2 and ∞).

In Figure 5, the reduction of the open-circuit voltage is also presented as a function of the normalized surface recombination velocity with the cell thicknes, X_B/L_B, as the constant parameter. It is evident from this family of curves that open-circuit voltage degradation begins to saturate when the surface recombination velocity of the perimeter defect is greater than ten times diffusion velocity, i.e., $S_D L_B/D_B > 10$. Both this figure and Figure 4 show that the $-\Delta V_{OC}$ is less than (kT/q) or 26 mV when the cell thickness is greater than about $0.35L_B$ in a cell whose BSF junction perimeter is completely short-circuited.

5. SUMMARY AND CONCLUSION

The effects of electrical short circuits across the back-surface-field junction at the perimeter or the edge surface of a solar cell is analyzed by applying the low-level one-dimensional analytical theory to a 'developed-cell' geometrical device model using the concept of distance-of-influence for the perimeter region of the cell. This perimeter or edge defect can cause a significant reduction of the open-circuit voltage and efficiency of a BSF cell. For small area, thin and large base-diffusion-length cells, the reduction of the open-circuit voltage and efficiency can be very large, so large that the edge defects can almost completely nullify the performance improvement offered by the back-surface-field junction. The results also illustrate the importance of edge or perimeter defects on the variation of the open-circuit voltage and efficiency in production lots of high-efficiency BSF solar cells.

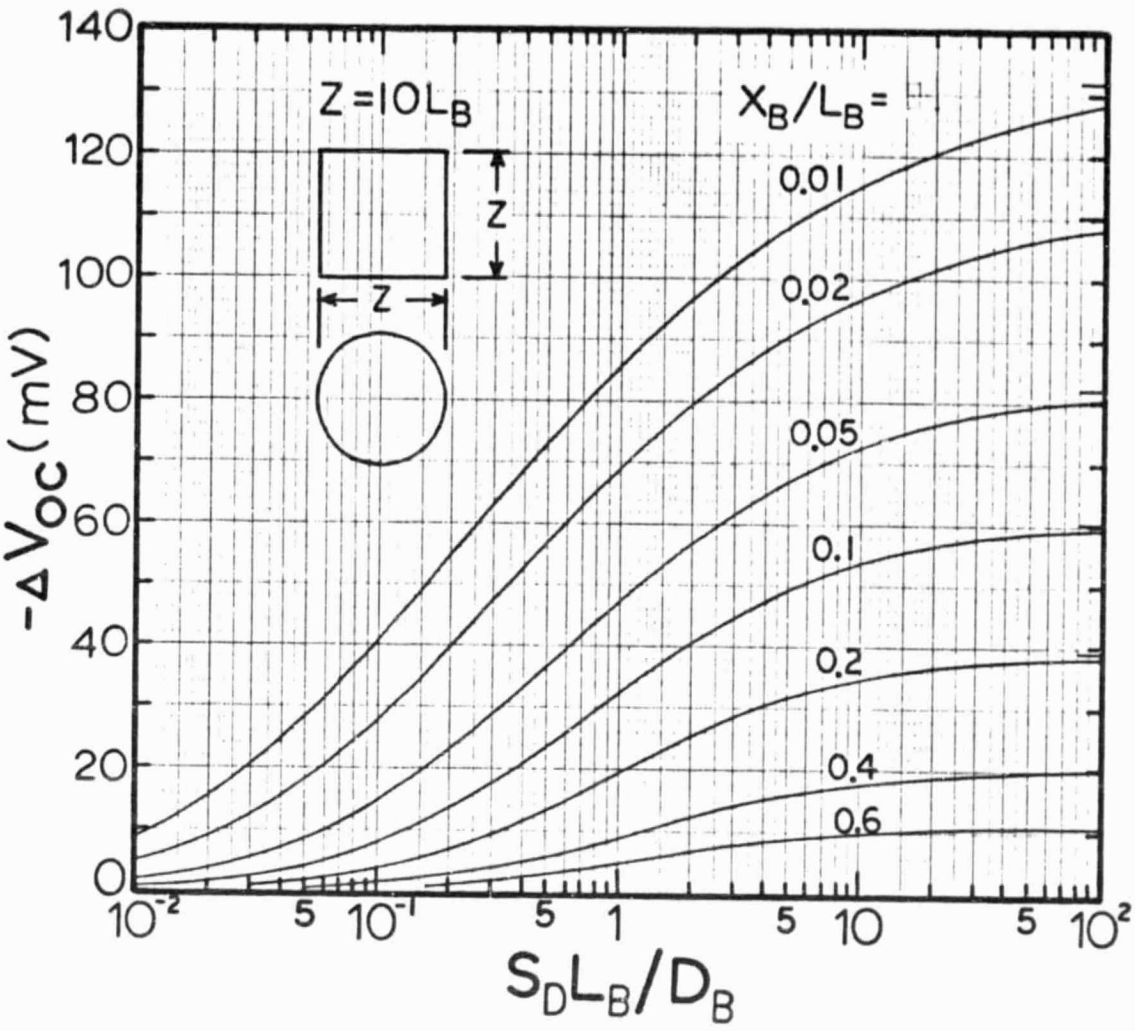

Fig. 5 The reduction of the open-circuit voltage as a function of the defect surface recombination velocity of solar cells with imperfect edge defects across the BSF junction. The cell diameter or size is ten times the base minority carrier diffusion length. The normalized cell thickness, X_B/L_B, is the constant parameter.

6. APPENDIX

In this appendix, the accuracy of the developed perimeter approximation, used to evaluate the integral given by Equation (4), is checked against an exact numerical evaluation of this integral. The exact integral uses the circular transformation

$$X^2 = X_B^2 + y^2 \tag{A.1}$$

instead of the linear transformation given by Equation (7). Thus, the exact and the approximate expressions for the integral given by Equation (4) are

$$I_2(\text{appro}) = \sqrt{(L+W)/(L-W)}\ \log_e[\sinh(L)/\sinh(W)] \tag{A.2}$$

and

$$I_2(\text{exact}) = \int_0^{\sqrt{L^2-W^2}} \text{ctnh}(\sqrt{y^2+W^2})\ dy \tag{A.3}$$

where $L=L_I/L_B$ and $W=X_B/L_B$. Equation (A.2) is similar to J_2A_2/Z_2 where Z_2 is the effective length of Region II given by the [ ] term in Equation (15) or (18) for the area A_2.

The percentage error, defined by $100[1 - I_2(\text{Appro})/I_2(\text{exact})]$, is computed numerically as a functon of cell thickness with the distance-of-influence, L_I/L_B, varied from 1 to 4. The largest error occurs in the thin cell range where X_B/L_B=0.01 to 0.2. The error varies from 10% to 14%. As X_B/L_B increases beyond 0.2 towards 1.0 or L_I/L_B, the error decreases rapidly towards zero. The results are graphed in Figure 6.

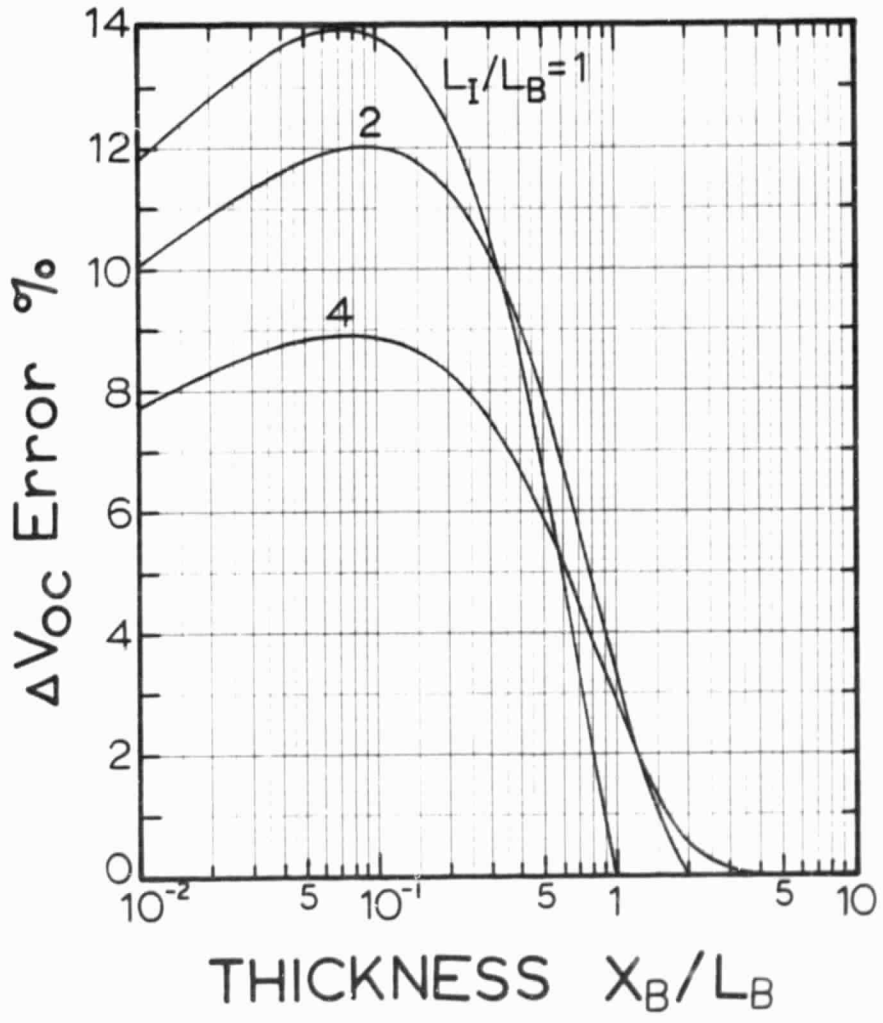

Fig. 6 The percentage error of the open-circuit-voltage computed from an analytical approximation to the integral, plotted as a function of the cell thickness.

7. REFERENCES

1. Michael P. Godlewski, Cosmo R. Baraona and Henry W. Brandhorst, Jr., "Low-High Junction Theory Applied to Solar Cells," Conference Record of the Tenth IEEE Photovoltaic Specialist Conference, pp.40-49, IEEE Catalog No. 73CH0801-ED (1973)

2. C. T. Sah. P. Chan, C. K. Wang, R. L. Y. Sah, K. A. Yamakawa and R. Lutwack, "Effect of Zinc Impurity on Silicon Solar Cell Efficiency," IEEE Transaction on Electron Devices, Vol. ED-28, pp. 304-313, March 1981.

3. J. Mandelkorn and J. H. Lamneck, Jr. "Simplified Fabrication of Back Surface Electric Field Silicon Cells and Novel Characteristics of Such Cells," Proc. 9th Photovoltaic Specialist Conference, pp. 66-72, IEEE Catalog No. 72CH0613-0-ED, May 2-3, 1973

4. R. N. Hall, Lecture Notes, IRE 1953 Electron Device Research Conference on Transistor and Semiconductor Material Seminars held at the University of Illinois, Urbana, IL.

5. J. G. Fossum and E. L. Burgess, "High Efficiency p+/n/n+ Back-Surface-Field Silicon Solar Cells," Applied Physics Letters, Vol. 33, pp. 238-240, August 1, 1978; J. G. Fossum, R. D. Nasby and E. L. Burgess, "Development of High-Efficiency p+/n/n+ Back-Surface-Field Silicon Solar Cells," Conference Record of the 13th IEEE Photovoltaic Specialist Conference, pp. 1294-1299, June 5, 1978. IEEE Catalog No. 78CH1319-3.

6. J. G. Fossum, "Physical Operation of Back-Surface-Field Silicon Solar Cells," IEEE Transactions on Electron Devices, Vol. ED-24, pp. 322-325, April 1977.

7. F. A. Lindholm and J. G. Fossum, "Physics Underlying Recent Improvements in Silicon Solar-Cell Performance," Technical Digest, IEEE International Electron Device Meeting, pp. 304-307, December 3, 1979. IEEE Catalog No. 79 CH1504-0ED.

8. C. T. Sah. K. A. Yamakawa and R. Lutwack, "Reduction of Solar Cell Efficiency by Bulk Defects Across the Back-Surface-Field Junction," to be published.

9. John R. Pierce, Traveling Wave Tubes, Van Norstrand, 1950

10. C. T. Sah, K. A. Yamakawa and R. Lutwack, "Effect of Thickness on Silicon Solar Cell Efficiency," to be published.

8. C. T. Sah, K. A. Yamakawa and R. Lutwack, "Reduction of Solar Cell Efficiency by Bulk Defects Across the Back-Surface-Field Junction," to be published (See preceding chapter).

9. John R. Peirce, Traveling Wave Tubes, Van Nostrand, 1950

10. C. T. Sah, K. A. Yamakawa and R. Lutwack, "Effect of Thickness on Silicon Solar Cell Efficiency," to be published (See Technical Report No. 4, March, 1981. DOE/JPL-954685-81/1)

III. REDUCTION OF SOLAR CELL EFFICIENCY BY BULK DEFECTS ACROSS THE BACK-SURFACE-FIELD JUNCTION#

1. INTRODUCTION

Back-surface-field solar cells contain a high-low (n+/n or p+/p) junction in the semiconductor near the back surface on which a metal-semiconductor ohmic contact is made. The potential barrier of the space-charge layer of this high-low junction prevents the emitter-junction injected and photogenerated minority carriers from reaching the ohmic contact on the back surface. Without the back-surface field, the minority carriers would reach the ohmic contact on the back surface and recombine with majority carriers at very high recombination rates. This would greatly increase the recombination current in a solar cell and decrease the efficiency and the open-circuit voltage. Without a back-surface field, the cell performance would decrease as the cell thickness is decreased since the ohmic high-recombination-rate back metal-semiconductor interface would be closer to the front injecting and collecting p/n junction. Thus, to achieve high efficiencies in solar cells, modern cell designs always contain a back-surface-field high-low junction.

The presence of a back-surface-field junction can increase the cell performance substantially over a cell without the back-surface-field junction. We shall call the cells without the back-surface-field junction the *back-surface-ohmic* cells and use the acronym BSF for back-surface-field and BSO for back-surface-ohmic cells in this paper. An illustration of performance improvement by the presence of a BSF is given in Fig.3.1 where the efficiencies of the BSF cells (n+/p/+ type) and the BSO (n+/p type) are given as a function of the base layer thickness, X_B. These curves were computed by numerically solving the one-dimensional Shockley Equations using the transmission line circuit model technique [1] for a low-level base minority-carrier diffusion

This chapter will be published in the April 1982 issue of the Journal of Applied Physics under the same title.

length of 577 μm under one AM1 (terrestrial) solar illumination. Such a long diffusion length was used to simulate state-of-the-art high-efficiency silicon solar cells [2].

Fig. 3.1 shows that the BSF cells have significantly higher efficiencies than the BSO cells as the thickness decreases. At 100 μm cell thickness, the BSF cell efficiency is 16.3% - 12.3% = 4% higher than the BSO cell.

The principal cell parameter that causes the lower efficiency in the BSO cells is the reduction of the open-circuit voltage in the BSO cells due to high recombination rate at the back-surface ohmic contact. This is illustrated in Fig. 3.2 for the two types of cells whose efficiencies were given in Fig. 3.1. In Fig. 3.2, the open-circuit voltage under one AM1 sun is given as a function of the cell thickness for the BSF and BSO cells. As an example, the open-circuit voltage in the back-surface-field cell of 100 μm thickness is 607 - 495 = 112 mV higher than the back-surface-ohmic cell.

The very large reduction of the cell performance due to the lack of a BSF high-low junction on the back surface just illustrated suggests that random defects across the BSF junction can significantly reduce the performance of high-efficiency cells and give rise to a large spread of cell characteristics in production lot quantities. The random defects that give rise to resistive shunts across the BSF low-high junction can be put into two groups: those that appear across the perimeter of the low-high BSF junction or on the edge of the cell and those that appear in the bulk of the low-high BSF junction. These are graphically shown in Fig. 3.3. The principal causes of these edge and bulk defects are mainly from the many manufacturing steps during the fabrication of the cells and they are tabulated in the following table. Their presence will reduce the cell performance from that of the ideal or perfect BSF cells, given by the upper curves in Fig. 3.1 and 3.2, to the shaded region below.

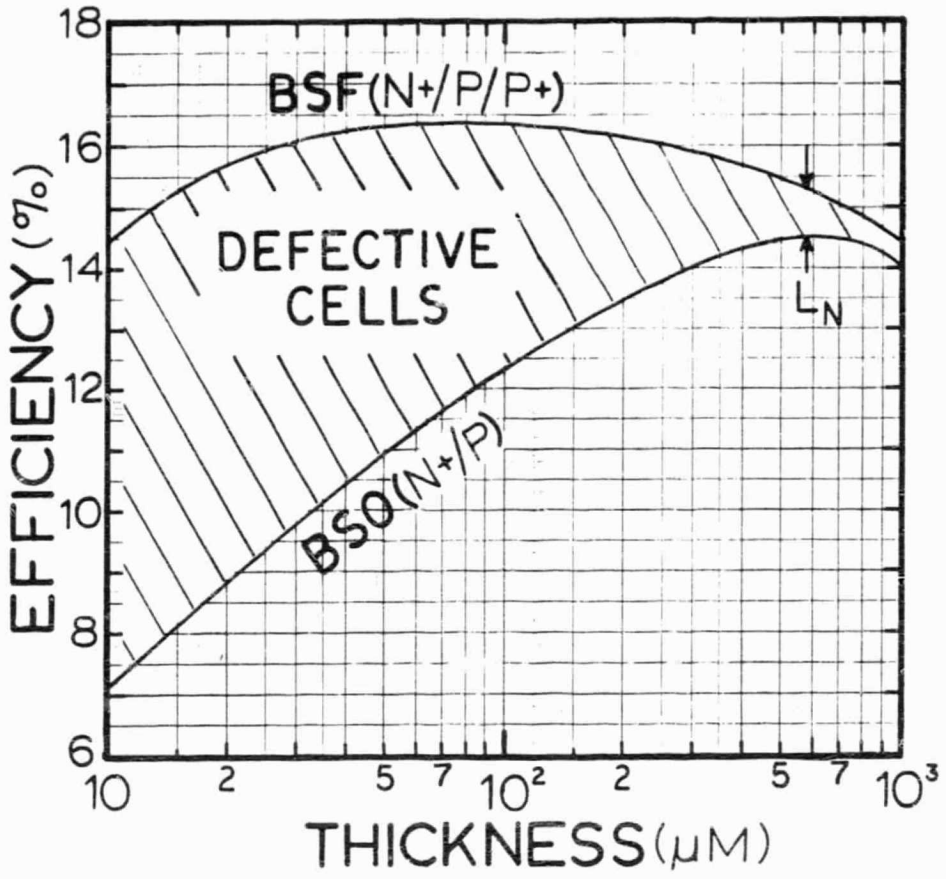

Fig. 1 AM1 efficiencies of BSF (back-surface-field) n+/p/p+ and BSO (back-surface-ohmic) n+/p silicon solar cells as a function of cell thickness with 577 μm base minority carrier diffusion length, computed by exact numerical solution of the one-dimensional Shockley Equations. Defective cells with defect across the BSF junction have efficiencies between the BSF and BSO cells.

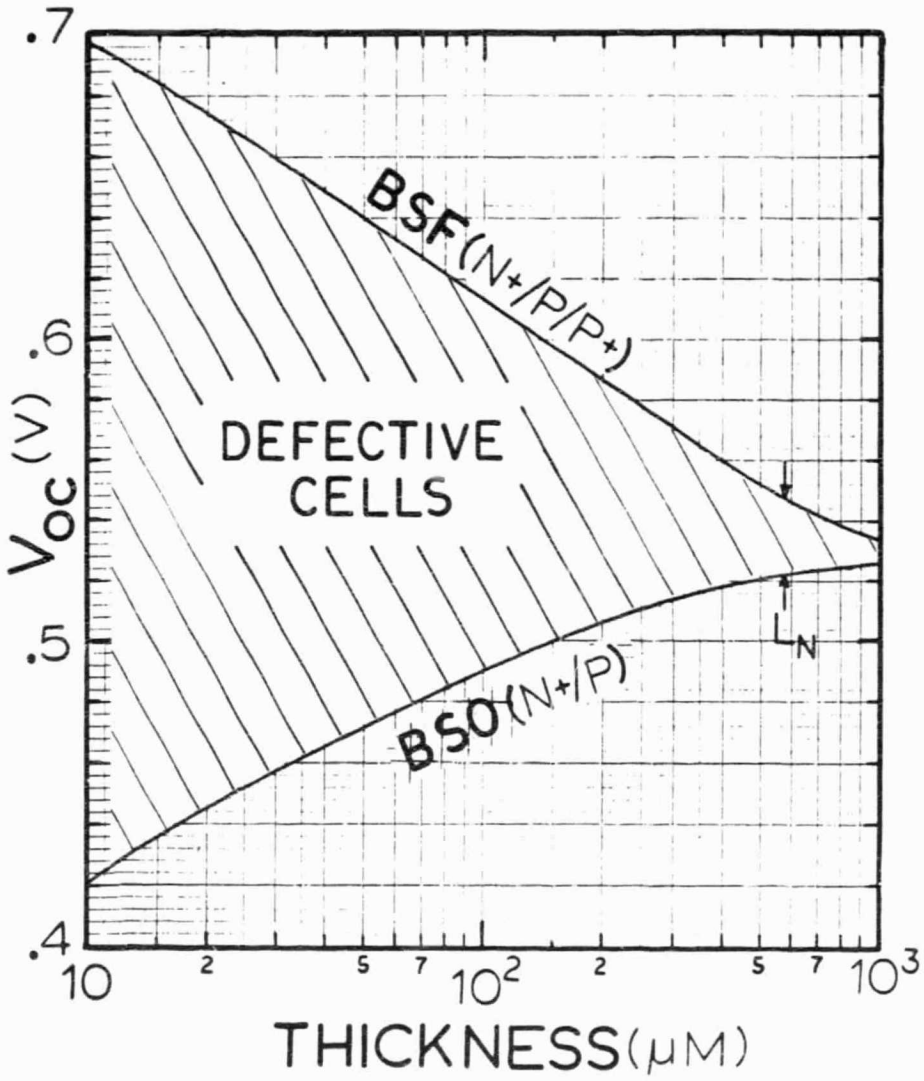

Fig. 2 AM1 open-circuit voltage of BSF (back-surface-field) n+/p/p+ and BSO (back-surface-ohmic) n+/p silicon solar cells as a function of cell thickness with 577 μm base minority carrier diffusion length, computed by exact numerical solution of the one-dimensional Shockley Equations. Defective cells with defect across the BSF junction have open-circuit voltages between the BSF and BSO cells.

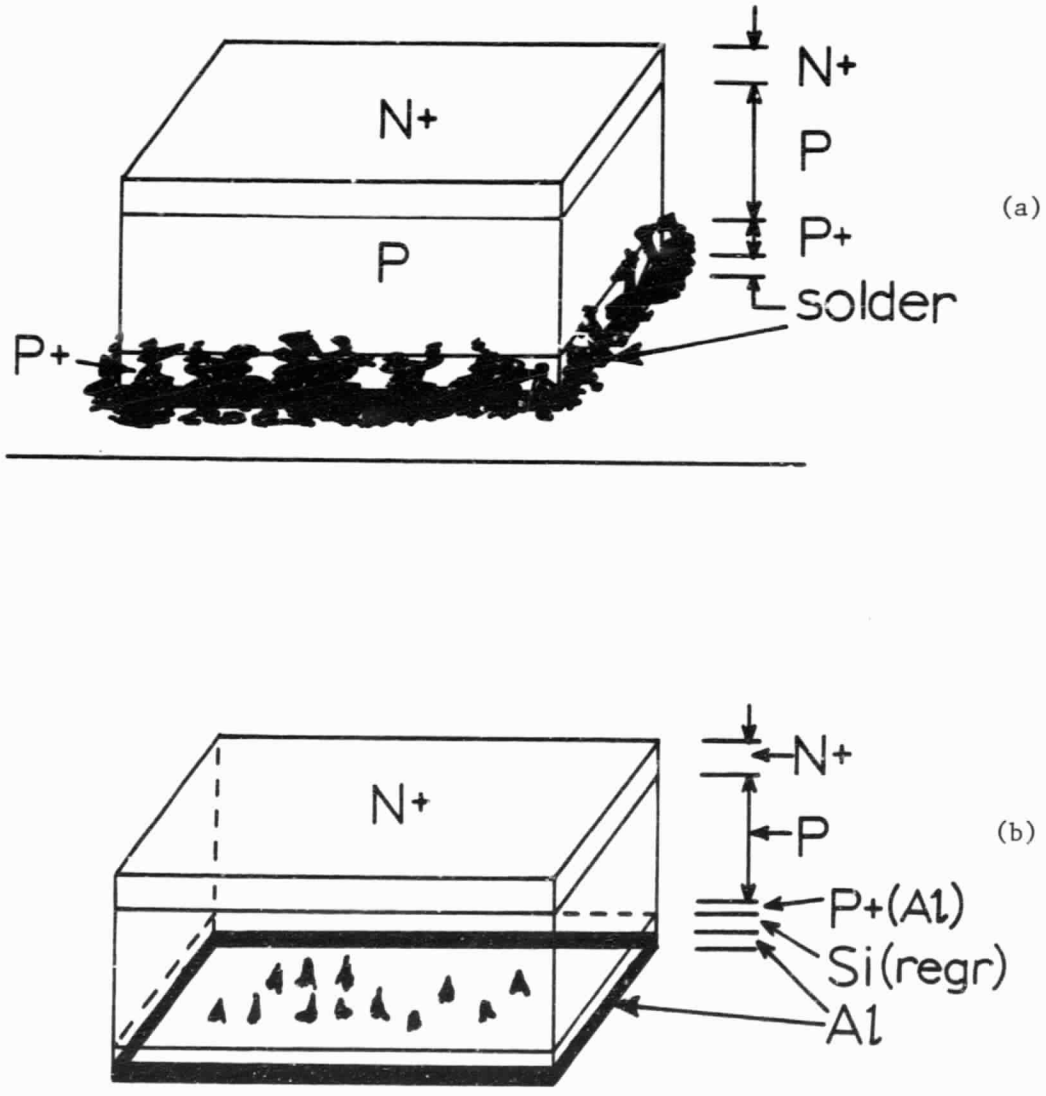

Fig. 3 (a) Edge and (b) bulk defects across the back-surface-field junction of a n+/p/p+ junction solar cell.

(A) Edge Defects

(1) Overflow of solder

(2) Imperfect perimeter surface etch

(3) Poor encapsulation

(B) Bulk Defects

(1) Poor alloying of the BSF junction

(2) Poor diffused BSF junction due to diffusion pipes

(3) Random back contact metal penetration

(4) Impurity segregation and cluster

These defects are even more detrimental to the cell performance if they appear across the front p/n junction. However, their degradation influence on the front junction is well known and manufacturing procedures are developed to minimize their presence across the front junction. Their influence on the performance of BSF junction have not been generally recognized nor analyzed.

In another paper, we have analyzed the effects on solar cell performance from edge defects across the BSF junction [3]. It is shown that these edge defects can significantly reduce the open-circuit voltage in thin high-efficiency cells. The reduction decreases when the area of the cell increases since the edge defects in a large area cell is less effective as a high-recombination sink for the injected minority carriers at the central portion of the cell which are far away from the edge of the cell in large area cells. However, the bulk defects across the BSF junction are distributed over the entire area of the cell and hence their performance-reduction influences cannot be reduced by increasing the area of the cell as in the case of edge defects. Thus, one would expect a much higher performance reduction caused by bulk defects than by the edge defects across the BSF junctions of high-efficiency solar cells.

The degradation of the solar-cell performance due to a distribution of bulk defects across the back-surface-field junction is analyzed in this paper. The device model employed is described in section 2 and the mathematical formulae are also given there. A detailed derivation of these formulae is given in the appendix. Families of curves are computed from these formulae and their physical significances are discussed in detail based on the three parameters which are used to characterize the defects: defect area, defect density and defect surface recombination velocity. The reduction of the open-circuit voltage due to the presence of the defect is presented as a function of defect area, density, cell thickness and defect surface recombination velocity. In section 3, the effects of short-circuiting defects are analyzed while in section 4, the effects of finite defect surface recombination velocity are described quantitatively. Numerical examples are given in each section to illustrate the importance of the particular defect parameter using numbers that are similar to those of the state-of-the-art high-performance silicon solar cells. A summary of this theoretical study is given in section 5.

2. DEVICE MODEL AND ANALYSES

The edge and bulk defects across the BSF junction of a solar cell are three-dimensional defects. They have random sizes and are randomly distributed. Thus, the nonlinear Shockley Equations which describe the diffusion, drift, recombination and generation of electrons and holes in a semiconductor cannot be solved analytically or numerically for solar cells which contain these random defects. Exact numerical solutions could be obtained for two limiting cases: (1) there is a negligible number of defect and (2) there is a very high density of defects which completely short circuit the BSF junction. These two ideal cases were computed and used as initial illustrations given in Figs. 3.1 and 3.2 to show the importance of the defects on the cell performance.

In order to obtain quantitative results for intermediate defect densities so that their effect on solar cell performance can be numerically estimated, approximate device models must be employed. A *developed perimeter* device model was constructed to analyze the effect of edge defects [3]. In this model, the solar cell is divided into two regions, a central region and a perimeter or edge region. The width of the edge region is determined by the low-level diffusion length of the minority carriers in the base. A parameter, called *the distance of influence*, was introduced to characterize the range of a defect and to relate the edge region width to the diffusion length. The simple one-dimensional low-level diffusion solutions of p/n junction current-voltage characteristics are then obtained for these two regions. The reduction of the open-circuit voltage was then computed numerically by connecting the two solar cells of these two regions in parallel.

The idea behind this developed perimeter model and the concept of distance-of-influence can also be applied to the randomly distributed bulk defects of random sizes across the BSF junction. To illustrate this defective

device model, a partial cell with several uniformaly space defects is shown in Fig. 3.4(a) which has three repetitive square unitcells enclosed by dashed boundaries. An enlarged top view of a unitcell is shown in Fig. 3.4(b). Extension of this uniform defect model to randomly distributed defects should become obvious after describing and analyzing the uniformly spaced defect model.

The unit cell is divided into three regions for analysis purpose. They showing the lateral influence of the defects. They are illustrated in Figs. 3.4 (b), (c) and (d) and described below.

(1) Region III

This is the central region of the unit cell which contains the defect. Its cross sectional area, A_3, is equal to the defect area, A_D.

(2) Region II

This is the first 'edge region' of the unit cell which surrounds the central region. The p/n junction in this region will experience the presence of the defective BSF low-high junction in region I. It has an area of A_2. Its width, W_2, is determined by the distance of influence or the range of the defect, L_I, and is given by [Fig. 3.4(c)]

$$W_2 = \sqrt{L_I^2 - X_B^2} \qquad (1)$$

where X_B is the thickness of the base layer.

(3) Region I

This is the second 'edge region' of the subcell which surrounds the first edge region, region II. The electrical characteristics of the p/n junction in this region will not be affected by the defect in region III since it is outside of the range or the distance of influence of the defect. Its area is denoted by A_1. This region does not exist if the defect density, D_D, is high or

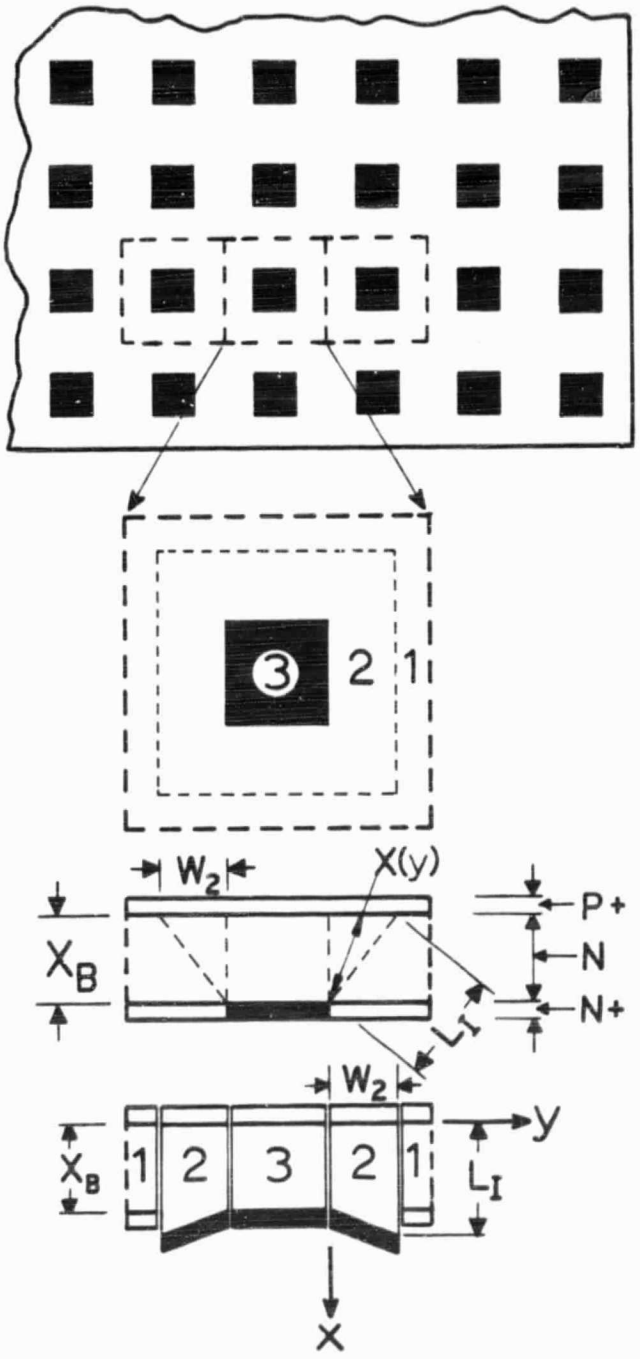

Fig. 4 (a) Top view, (b) expanded unit cell top view, (c) expanded cross sectional view, and (d) developed perimenter cross sectional view of a defective back-surface-field solar cell.

the distance-of-influence is large. The condition for the disappearance of this region or $A_1=0$ is when

$$L_I > \sqrt{X_B^2 - \tfrac{1}{4}[(1/\sqrt{D_D}) - \sqrt{A_3}]^2} \tag{2}$$

or

$$X_B < \sqrt{L_I^2 - \tfrac{1}{4}[(1/\sqrt{D_D}) - \sqrt{A_3}]^2} \tag{3}$$

This three-region device model for a bulk defect differs from the two-region device model for the edge defect in having a finite region III which contains the bulk defect. In the two-region device model for the edge defect, region III has zero area since the edge defect is on the perimeter surface of the cell and has zero projection onto the plane of the p/n junction.

Although analytical three-dimensional series solutions can be obtained in the three regions for the low-level dark diffusion current-voltage characteristics, simpler solutions will be worked out using the one-dimensional solution and developed perimeter model. The approximation in such a one-dimensional model is probably not much worse than the analytical three-dimensional low-level solution since in a real cell the defects have random size and are randomly distributed while the analytical three-dimensional solution needs to define the shapes of the subcell and defect. The one-dimensional solution, to be given below, is physically transparant and simple to grasp, and allow us to study the effect of defect density and size on the cell performance reduction using families of curves which can be computed with very little computing time. Three-dimensional analytical solution would give much more complex solutions which would not be as transparant and require much more computing time to generate the same families of curves to estimate the numerical reductions of cell performance due to the presence of the defects.

The cross-sectional view of the three regions of the unit cell is shown in Fig. 3.4(c). The developed model is shown in Fig. 3.4(d) where regions I and III have constant base thicknesses equal to the actual base layer thickness, X_B. Region II has a varying base thickness, X, increasing from X_B to L_I. The distance of influence or the range of the defect, L_I, is assumed to be proportional to the minority carrier diffusion length in the base, L_B. In the numerical calculations to be given later, it will be shown that the numerical results on the open-circuit voltage reduction will have reached an asymptotic and constant value when L_I is taken to be greater than about $1.5L_B$. Thus, all of the numerical results obtained in this paper are for $L_I=2L_B$.

The one-dimensional dark diffusion current solution for a p/n junction at low level with a back-surface field was first applied to BSF solar cells by Godlewski, Baraona and Brandhorst [4]. This solution is applied to all three regions of the defective unit cell. For the defect-free region I, a zero interface recombination velocity is assumed at the base-side of the BSF low-high junction. For the defective Region III, the defect is characterized by a finite interface surface recombination velocity, S_D, again on the base-side edge of the space-charge layer of the BSF low-high junction. For the worst defect, $S_D=\infty$, which corresponds to a defect that completely short-circuits the BSF junction. It will be shown in section 4 that when the normalized interface recombination velocity, S_D/v_D (where $v_D=D_B/L_B$ is the diffusion velocity of the minority carrier in the base layer), is greater than about 10, the open-circuit voltage degradation will have essentially reached its highest value and the defect acts essentially like a short circuit or the defective Region III is essentially a BSO (back-surface-ohmic) cell.

In region II, the one-dimensional dark diffusion current solution is also employed. The varying base layer thickness in Region II, in Fig. 3.4(c) and (d),

is taken care of by an average procedure which was also employed for the Region II of the edge defect [3]. In this average, the one-dimensional diffusion current density at each base layer thickness, X, is summed over the entire Region II, from $X=X_B$ to $X=L_I$ along the surface from $y=0$ to $y=W_2=\sqrt{L_I^2-X_B^2}$. The detailed algebra is given in the appendix.

The dark current-voltage characteristics of the three regions are summarized below. In Regions I and III, the current densities are constant across the plane of the junction so that the current in each region is just the current density times the area. In Region II, the varying current density is integrated over its area to give the total current whose detailed steps are given in the appendix. The dark currents are

$$I_1 = J_1A_1[\exp(qV/kT) - 1] \tag{4}$$

$$I_2 = J_2A_2[\exp(qV/kT) - 1] \tag{5}$$

$$I_3 = J_3A_3[\exp(qV/kT) - 1] \tag{6}$$

The dark current flowing in an ideal cell without any defects is given by

$$I_0 = J_0A_0[\exp(qV/kT) - 1] \tag{7}$$

The current densities and the areas of the three regions as well as in the defectless cell are given by

$$J_0 = J_1 = (qD_BP_B/L_B)\tanh(X_B/L_B) \tag{8}$$

$$J_2 = [qD_BP_B/(L_I-X_B)]\log_e\left[\frac{\exp[(L_I/L_B)\tanh(X_B/L_B)] + (S_DL_B/D_B)\sinh(L_I/L_B)}{\exp[(X_B/L_B)\tanh(X_B/L_B)] + (S_DL_B/D_B)\sinh(X_B/L_B)}\right] \tag{9}$$

$$J_3 = (qD_BP_B/L_B)\left[\frac{\sinh(X_B/L_B) + (S_DL_B/D_B)\cosh(X_B/L_B)}{\cosh(X_B/L_B) + (S_DL_B/D_B)\sinh(X_B/L_B)}\right] \tag{10}$$

$$A_0 = A_1 + A_2 + A_3 \tag{11}$$

$$A_2 = 4\sqrt{L_I^2-X_B^2}(\sqrt{L_I^2-X_B^2} + \sqrt{A_3}) \tag{12}$$

$$D_D = 1/A_0 \tag{13}$$

D_D is the areal density of the defect since A_0 is the unit cell area and

the unit cell was selected so that it contians only one defect as illustrated in the uniform model shown in Figs. 3.4(a) and 3.4(b). The other parameters in (8) to (13) have the conventional meaning. q is the magnitude of the electron charge. D_B, P_B, $L_B=\sqrt{D_B\tau_B}$ and τ_B are respectively the diffusivity, equilibrium concentration, diffusion length and lifetime of minority carriers in the quasi-neutral base layer under low-level condition. L_I is the range or distance-of-influence of the defect and is taken as $2L_B$ in this paper. X_B is the thickness of the quasi-neutral base layer. S_D is the effective interface recombination velocity of a defective low-high junction. S_D is used to represent defects which are not completely electric short circuits across the BSF low-high junction and defects which are due to a high-layer (p+ layer of the p/p+ low-high junction or n+ layer of the n/n+ low-high junction) of very high recombination rate or very low minority carrier lifetime. It can also represent partial penetration into the high-layer by the back ohmic contact metal or alloy as well as diffusion pipes.

There are three independent parameters which characterize the property of the defect: (i) the defect area, $A_D=A_3$, (ii) the defect density, $D_D=1/A_0$, and (iii) the surface recombination velocity at the defect, S_D. The area of Region II which experiences the presence of the defect is related to the defect area by (12). The area of Region I which is outside of the range or the influence of the defect is related to the defect area and density by (11). When a cell is very thin such that its thickness is less that given by (3), A_1 is zero.

The reduction of the open-circuit voltage, $-\Delta V_{OC}$, can be computed by comparing the total current of a perfect cell, I_0, with the total current of a defective cell which is $I_1+I_2+I_3$ at a constant photocurrent, I_L. Let the open-circuit voltage across the defective cell be $V_{OC}+\Delta V_{OC}$ and that across the

perfect cell be V_{OC}, then at open-circuit or zero load current, we have

$$I_L = I_1 + I_2 + I_3 = (J_1A_1+J_2A_2+J_3A_3)\{\exp[q(V_{OC}+\Delta V_{OC})/kT] - 1\} \quad (14)$$

for the defective cell and

$$I_L = I_0 = J_0A_0\{\exp[q(V_{OC})/kT] - 1\} \quad (15)$$

for the perfect cell. Normally, $V_{OC}+\Delta V_{OC} >> (kT/q)$ so that we can drop 1 compared with $\exp[q(V_{OC}+\Delta V_{OC})/kT]$ or $\exp[q(V_{OC}/kT)]$ in (14) and (15). Then, the reduction of V_{OC} is independent of the photocurrent, I_L, or the open-circuit voltage V_{OC} which can be eliminated between (14) and (15). This gives

$$-\Delta V_{OC} = (kT/q)\log_e[(A_1/A_0) + (J_2A_2+J_3A_3)/J_0A_0] \quad (16)$$

Numerical solutions and families of curves have been computed from the general solution given by (16) using (8) to (13) for the current densities and the areas. A little algebra of (16) will show that all the length parameters can be normalized to the diffusion length, L_B. Thus, the normalized variables are X_B/L_B, A_D/L_B^2 where $A_D=A_3$, and $D_DL_B^2$ where $D_D=1/A_0$. The defect surface recombination velocity, S_D, can also be normalized to a minority carrier diffusion velocity, $v_D=D_D/L_D$. Thus, the reductions of the open-circuit voltage are graphed as a function of these normalized parameters. An important general result is that the reduction of the open-circuit voltage is independent of the area of the cell but depends on the areal density of the defect, D_D. Although our analysis was made for a periodic unit cell of the uniform defect model, this general result is valid for randomly distributed defects. In that case, D_D would be the average density of the defect over the entire cell which may vary from one subcell to the next subcell.

These numerical solutions, plotted as a function of thickness of the quasi-neutral base layer (or roughly the cell thickness since the n+ and p+ layers of the diffused n+/p and p/p+ junctions are less than one micron thick), with the three defect parameters, A_D/L_B^2, $D_DL_B^2$ and D_D, as constants are given in the next two sections with their physical interpretations.

3. EFFECT OF SHORT-CIRCUIT BULK DEFECT ON OPEN-CIRCUIT VOLTAGE

We shall first investigate the worst bulk defect which is the defect that completely short circuits the BSF low-high junction over the defective area, A_D. In this case, $S_D=\infty$, and the current densities in Regions II and III given by (9) and (10) simplify to

$$J_2 = [qD_BP_B/(L_I-X_B)]\log_e\left[\frac{\sinh(L_I/L_B)}{\sinh(X_B/L_B)}\right] \tag{17}$$

and

$$J_3 = (qD_BP_B/L_B)\mathrm{ctnh}(X_B/L_B) \tag{18}$$

3.1 Dependence on the Distance-of-Influence

Our model relies on the parameter L_I which is the range or the distance-of influence of the defect. It was assumed in the model that outside of this range or distance-of-influence, the defect will not affect or increase the dark recombination current and hence nor the open-circuit voltage. Thus, a test of the goodness of this model would be to determine how much the results will change with different choices of L_I. For this test, we assumed a defect area of 100 μm^2, a diffusion length of 100 μm so that $A_D/L_D^2 = 10^{-2}$. We also assume a normalized defect density of $D_DL_B^2 = 0.1$. The fractional defective area in this case is $A_DD_D=10^{-3}$ or 0.1% of the cell area is defective.

The reduction of the open-circuit voltage, $-\Delta V_{OC}$, computed from (16), at three cell thicknesses, X_B/L_B=0.01, 0.1 and 1.0, are shown in Fig. 3.5. It is evident that for thin cells (X_B/L_B=0.01 and 0.1) the results do not change much if the range or distance-of-influence is assumed to be 1.5 times the diffusion length or greater. For the thicker cell (X_B/L_B=1.0), the reduction of the open-circuit voltage by the defective area is small (only about 10 mV), but in order to get this result, the distance of influence must take a value greater than twice the diffusion length. Thus, in the remaining calculations, $L_I=2L_B$ is selected.

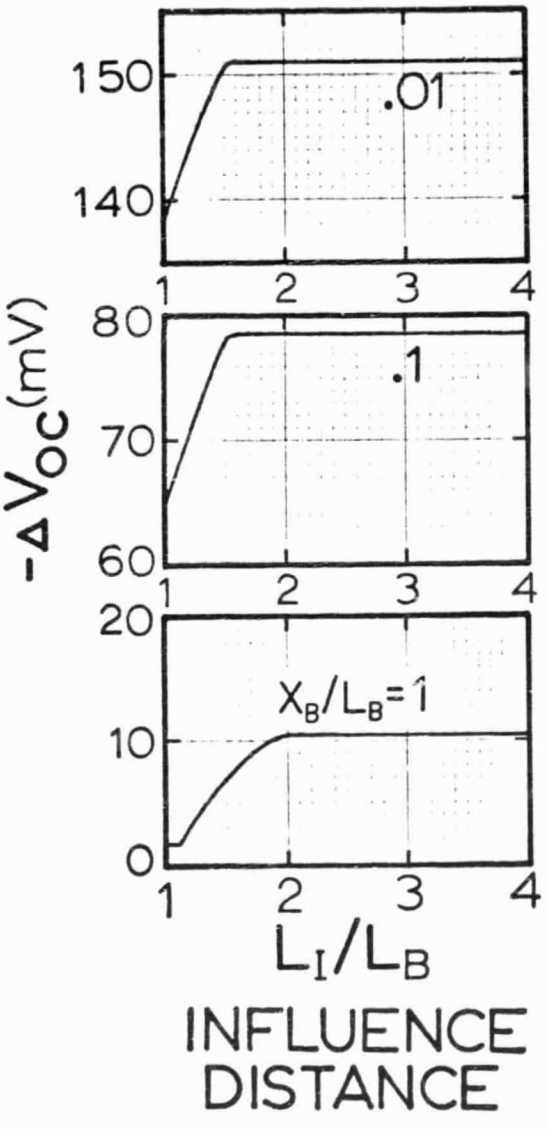

Fig. 5 The sensitivity of the open-circuit-voltage reduction on the choice of the distance of influence.

3.2 Dependence on the Defect Area

The dependence of the open-circuit-voltage reduction on the defect area, A_D, or the area of Region III shown in Fig. 3.4(b) is illustrated in Fig. 3.6. Here, the reduction of the open-circuit voltage is given as a function of the normalized defect area, A_D/L_B^2, for three cell thicknesses, X_B/L_B=0.01, 0.1 and 1.0. The constant defect density is $D_D L_B^2$=0.1. We also used L_I=2L_B and S_D=∞. The results in Fig. 3.6 show that the open-circuit reduction, $-\Delta V_{OC}$, reaches constant values when the defect area is smaller than about 0.01 times the diffusion length squared, L_B^2. This asymptotic behavior can be understood from the geometry of the device model. From Fig. 3.4(b), it is evident that when A_3 or the defect area A_D becomes small, its contribution to the base recombination current becomes small. The increase of the base recombination current comes entirely from Region II when $A_3 \to 0$. The relative contribution from the two regions, II and III, is slightly smaller than their area ratio, A_2/A_3, since the p/n junction in Region II is further away from the defect than in Region III. When A_3 becomes small compared with L_B^2, A_2 approaches a constant. From (12), when $\sqrt{A_3}$ or $\sqrt{A_D}$ is about 10 times smaller than $\sqrt{L_I^2-X_B^2} = 2L_B\sqrt{1-(X_B/2L_B)^2}$, then A_2 is essentially a constant given by $4(L_I^2-X_B^2)$.

This insensitivity to the defect area is an important result since in practice the defect area is probably small compared with the diffusion length squared in high-efficiency cells where the diffusion length is substantially greater than 10 μm. Thus, in practice, A_D/L_B^2 is less than about 0.01.

The effect of defect area can also be examined from the opposite direction. Fig. 3.6 shows that open-circuit degradation, $-\Delta V_{OC}$, begins to increase when the defect area is greater than about $0.1L_B^2$. This corresponds to a fractional defective area of $D_D A_D$=0.1x0.1=0.01 in this example or 1% of the area is defective.

This insensitivity is also the basis of taking A_D/L_B^2=0.01 in the analysis of the dependence on L_I given in the preceding section, 3.1.

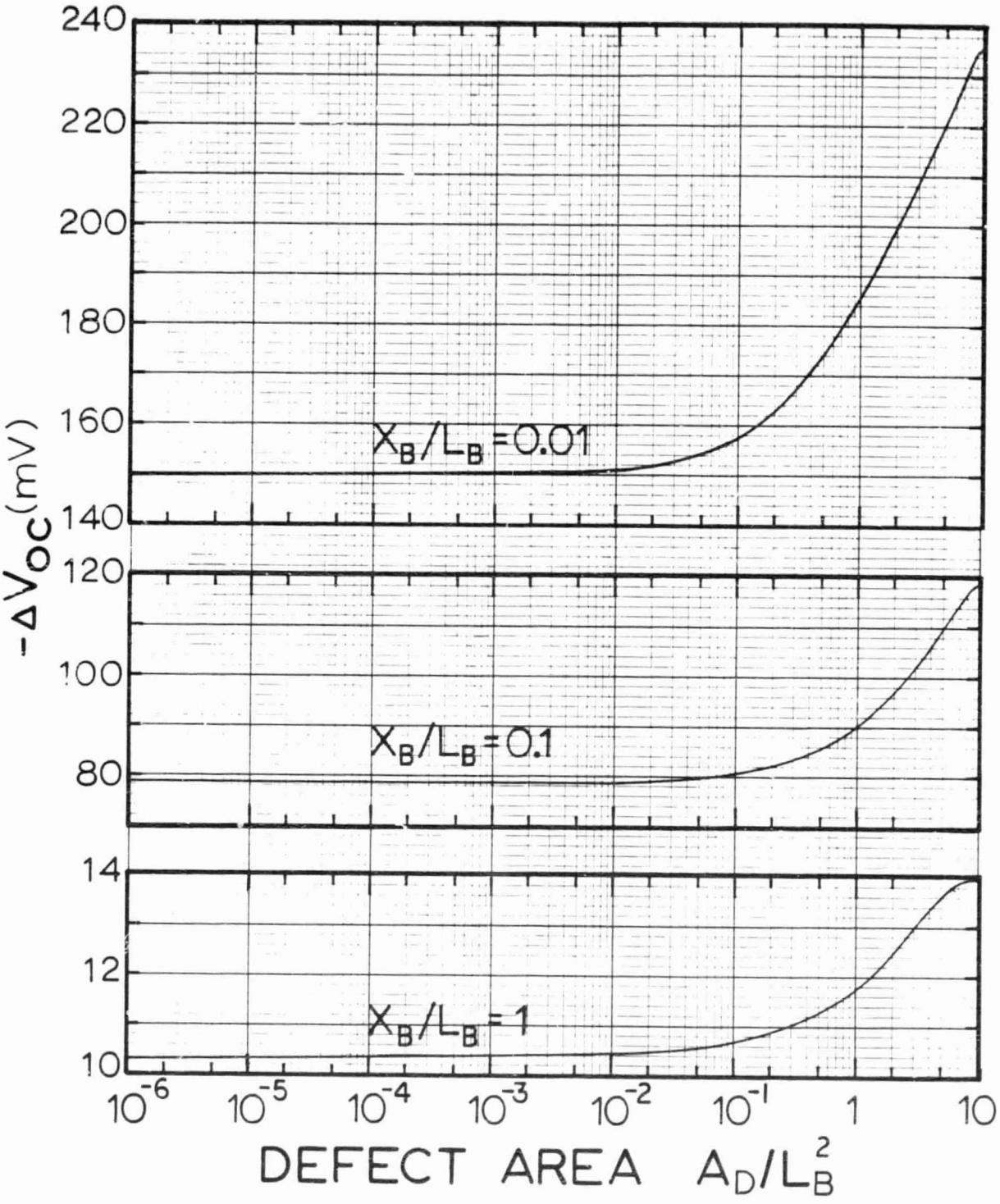

Fig. 6 The reduction of the open-circuit-voltage of a BSF solar cell as a function of defect area with cell thickness as the constant parameter.

3.3 Dependence on the Defect Density

In the preceding section, it was shown that increased recombination or reduction of open-circuit voltage came mainly from region II, the peripheral region that surrounds the defective area, Region III, since in practice, the size of the defective area is much smaller than the diffusion length. This illustrated the importance of the peripheral area surrounding the defect.

As the defect density increases, the number of defect increases for a given total cell area. Thus, the total surrounding area (the sum of the areas of each Region II) also increases since it is proportional to the number of defect. The dependence of the open-circuit-voltage reduction, $-\Delta V_{OC}$, on the defect density is expected to be large. This is illustrated in two ways: $-\Delta V_{OC}$ is plotted as a function of defect density, $D_D L_B^2$, with (i) defect area, A_D/L_B^2 kept constant or (ii) fractional defective area, $D_D A_D$, kept constant. These are shown in Figs. 3.7(a) and (b). The large dependence and increase of the open-circuit-voltage reduction with increasing defect density is evident in Fig. 3.7(a) when the defect area, A_D/L_B^2, is kept at constant values. When the fractional defective area reaches unity, V_{OC} reaches the value of a BSO cell which has no BSF low-high junction and $-\Delta V_{OC}$ also reaches its highest value which is the difference between the BSF and BSO cells. For the example shown in Fig. 3.7, this asymptotic value for $-\Delta V_{OC}$ is 235.8 mV.

The general trend of rapid increase of $-\Delta V_{OC}$ with increasing defect density is also evident in Fig. 3.7(b) when the fractional defective area is kept at constant values. The increase is somewhat slower than when the defect area is kept constant since as D_D increases, A_D decreases in order that $A_D D_D$ is constant and there is a decrease of $-\Delta V_{OC}$ at large A_D.

The important practical implication of this result is that the defect

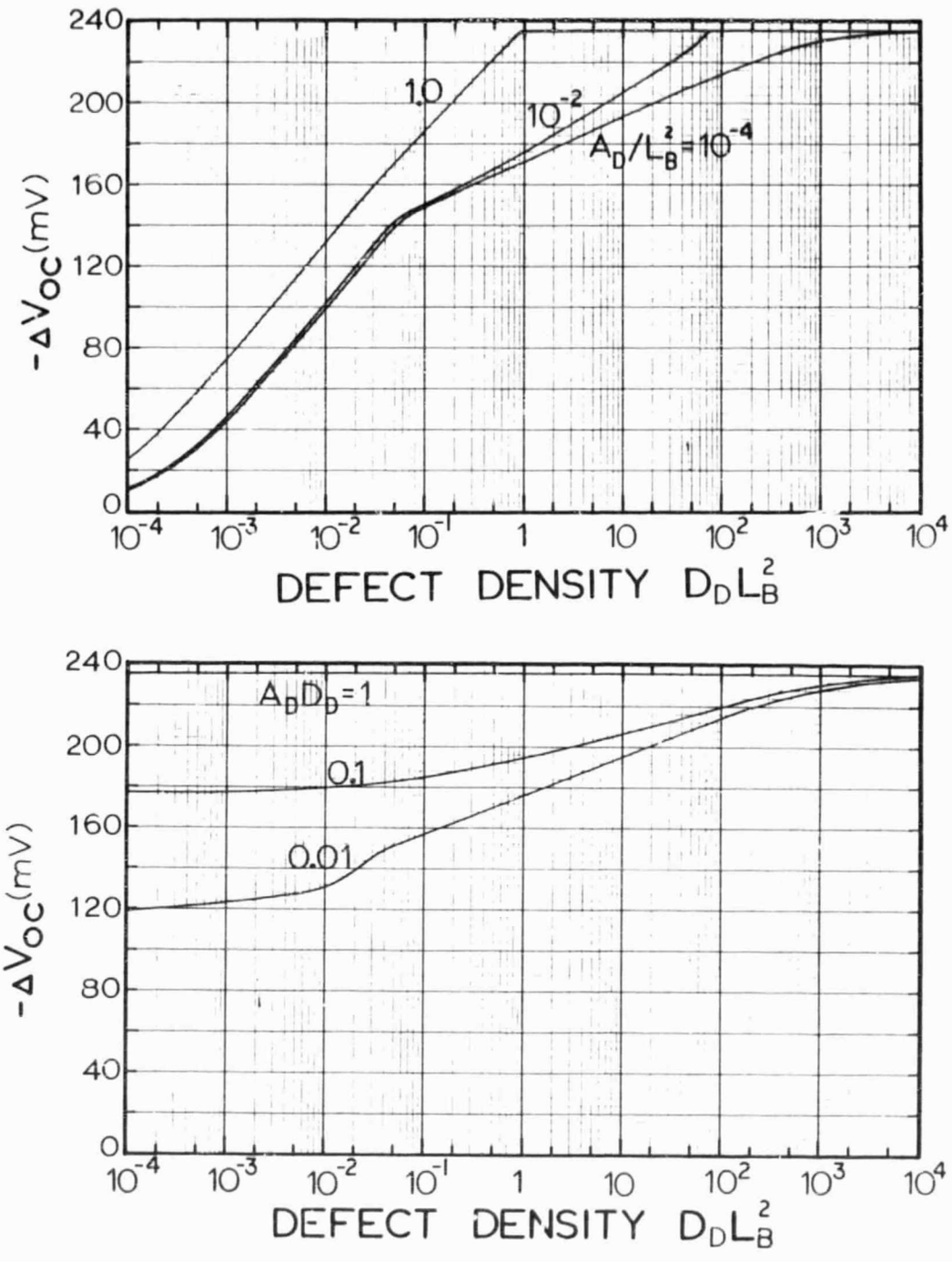

Fig. 7 The reduction of the open-circuit-voltage of BSF solar cells as a function of defect density with defect area as the constant parameter (top figure) and fractional defective area as the constant parameter (lower figure).

density should be kept as low as possible in order to obtain the maximum benefits from the BSF junction. For two cells each having 1% defective area, the one with the smaller defect density and larger individual defect area will give higher open-circuit voltage and efficiency. Thus, if a choice must be made in a practical situation between defect density and individual or average defect area, better open-circuit voltage and efficiency is obtained by keeping the defect density low and defect area large. A cell with one defect will have a higher open-circuit voltage and efficiency than a cell with two defects of half area. The physical reason is that the one with two defects will have two peripheral areas, one surrounding each defect, which would give nearly twice as much recombination current as the one peripheral area in a cell with one defect.

3.4 Dependence on the Cell Thickness

The results of the analyses in the preceding three sections, 3.1, 3.2, and 3.3, enable us to select a range of values for the defect parameters, area and density, so that they fall into practical ranges. The dependence of the open-circuit-voltage reduction on the cell thickness will be investigated using these ranges of values. The defect area is set at $10^{-4}L_B^2$ since it was shown in Fig. 3.6 that $-\Delta V_{OC}$ is insensitive to the defect area when A_D/L_B^2 is smaller than about 0.01 and since in practical high-efficiency cells, L_B is usually greater than 30 or 100 μm and the defect area is not likely to be greater than 100 μm^2 or 10 μm on a side. Thus, in practice, A_D/L_B^2 is likely to be less than 0.01. The choice of $A_D/L_B^2=10^{-4}$ is made since below 10^{-2}, $-\Delta V_{OC}$, is nearly constant and approaches its asymptotic value at 10^{-4}.

$S_D = \infty$ is assumed and the dependence on this parameter is analyzed in a later section. $L_I=2L_B$ since the result becomes independent of L_I when it is greater than about 1.5 as discussed in Section 3.1.

The defect density is the constant parameter. The range of the normalized defect density, $D_D L_B^2$, is from about 10^{-4} to 10^{-1} for high efficiency cells which is estimated as follows. For a high efficiency cell, L_B is between 100 μm and 1000 μm. We let L_B=100 μm. D_D is equal to the number of defect divided by the cell area, $D_D=N_D/A_C$. A production cell has an area of about 50 cm^2 (3 inch diameter) or greater. We let A_C=100 cm^2. For a good cell fabrication process, the number of defect is probably considerably less than 1000 and let N_D=1 to 1000. Thus, for a high efficiency cell, the normalized defect density should be in the range of $D_D L_B^2=(N_D/A_C)L_B^2=(1/100)(100\times10^{-4})^2=10^{-4}$ to $(1000/100)(100\times10^{-4})^2=0.1$. Thus, for a low defect density cell, the defect density range is approximately $D_D L_B^2=10^{-4}$ to 10^{-1} while for highly defective cells, $D_D L_B^2 > 10^{-1}$.

The range of the normalized cell thickness, X_B/L_B, covers from about 10^{-2} or less to about 10. This range covers a diffusion length of 100 μm and cell thickness of 1 to 500 μm.

From the above estimates of the ranges of the parameters, the reduction of the open-circuit voltage as a function of cell thickness is computed from (16). The results for the entire defect density range of 10^{-3} to ∞ are shown in the upper part of Fig. 3.8. The expanded graph, for low-defect-density high-efficiency cells covering $D_D L_B^2=10^{-4}$ to 10^{-1}, is given in the lower part of Fig. 3.8 with a larger number of the density parameter per decade.

When the defect density is infinite (curve $D_D L_B^2=\infty$), the reduction of the open-circuit voltage reaches the asymptotic value which is the difference between a perfect BSF cell and a BSO cell which has no BSF junction at all. The upper part of Fig. 3.8 shows that the asymptotic dependence on cell thickness is approached when defect density, $D_D L_B^2$, is greater than about 10 to 100. For this limiting case, (16) simplifies to

$$-\Delta V_{OC} = 2(kT/q)\log_e[\mathrm{ctnh}(X_B/L_B)] \qquad (19)$$

which gives the linear dependence on the semi-log plot in Fig. 3.8 for thin cells.

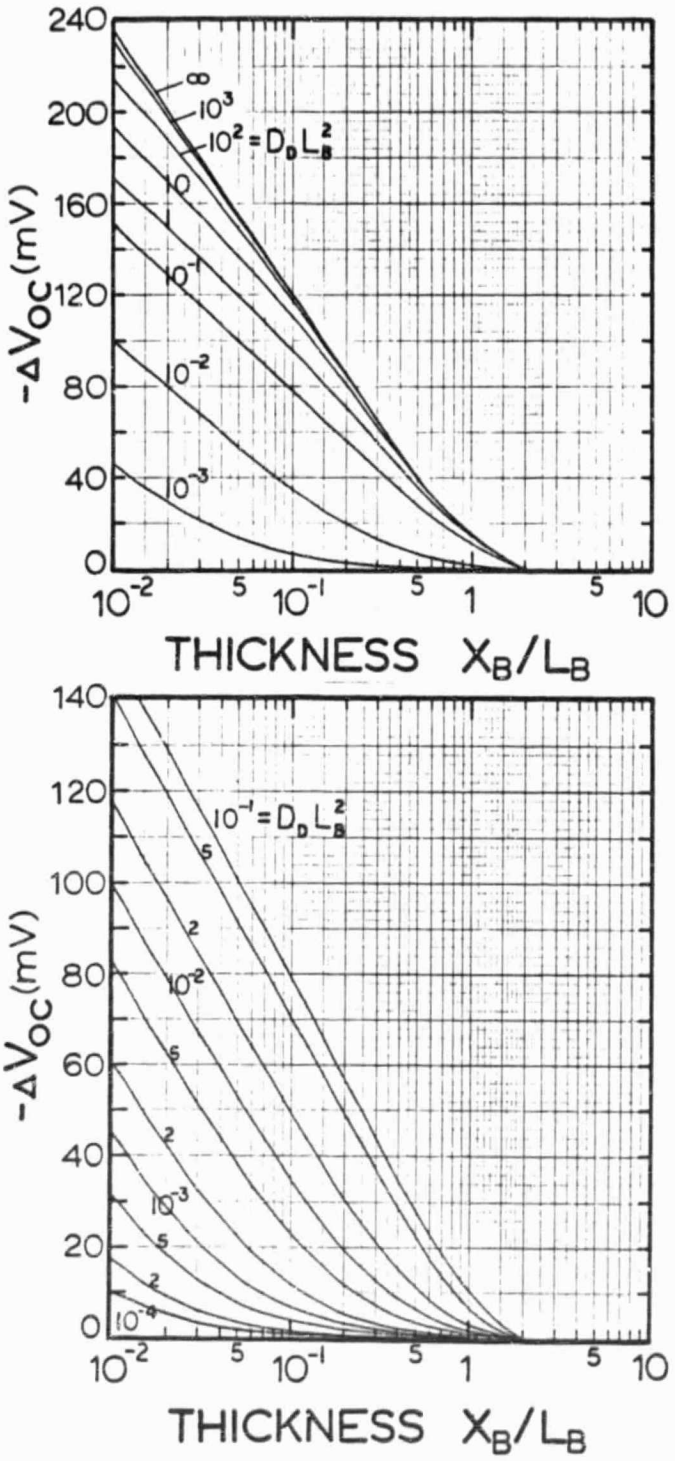

Fig. 8 The reduction of the open-circuit-voltage of BSF solar cells as a function of cell thickness with the defect density as the constant parameter.

A numerical example is given next to illustrate the possible importance of defective BSF junction on the open-circuit voltage. For this example, we use the parameters of the p+/n/n+ cell which has the highest reported V_{OC} of about 620 mV [2]. The reported values are τ_B=400 μs, L_B=775 μm, X_B=314 μm, X_B/L_B=0.4. Suppose that there is one short-circuiting defect per cm^2, then $D_D L_B^2 = 6.0 \times 10^{-3}$. Let us suppose that the normalized defect area, A_D/L_B^2, is less than 10^{-2} so that the result is independent of its area. This corresponds to a defect size of less than 80 μm on an edge, for example, the defect area can be taken as 1 μm^2. Then, $\Delta V_{OC} = -5.49$ mV from (9) or using Fig.3.8. If the defect density increases to 2 per cm^2, then $\Delta V_{OC} = -10.0$ mV. These two numerical examples show that reduction of the open-circuit voltage in a high-efficiency cell due to defects across the BSF junction may be quite significant even for fairly thick cells.

V_{OC} reduction is substantially larger if the cell is thinner. For example, maximum efficiency of the above cell would be reached when the cell thickness is reduced to about 80 μm as indicated in Fig. 1 or $X_B/L_B = 0.1$. Using the above numerical example and supposing that D_D=1 defect/cm^2, then $\Delta V_{OC} = -25.697$ mV while for D_D= 2 defect/cm^2 we have $\Delta V_{OC} = -38.26$ mV. These two numerical results show that the presence of 1 or 2 defects in 1 cm^2 of cell area would reduce the expected improvement of V_{OC} of approximately 60 mV by as much as a factor of 2 to only 30 mV when the cell thickness is reduced from the conventional 300 μm to an optimum 70 μm.

3.5 Dependence on Diffusion Length

In the preceeding analyses and numerical examples, the minority carrier diffusion length in the base layer, L_B, is the normalization parameter for length and area. Dependence of V_{OC} on defect density, defect area and cell

thickness was analyzed by keeping the diffusion length a constant. In some practical situations, such as debugging a fabrication process, evaluating radiation hardness and damage and others, it may be important to know how much the cell performance will be changed by the presence of defective BSF junctions when the minority carrier diffusion length or lifetime is changed.

Instead of presenting yet another family of curves of $-\Delta V_{OC}$ vs L_B, we make use of Fig. 3.8 to illustrate the dependence of ΔV_{OC} on L_B. From the two parts of this figure, it is evident that if we keep the cell thickness, X_B, and defect density, D_D, constant and increase L_B, then X_B/L_B will decrease which would increase the reduction of V_{OC} but $D_D L_B^2$ will increase also which will further increase the reduction of V_{OC} or $-\Delta V_{OC}$.

For example, if the diffusion length is increased by a factor of 10 from $L_B/X_B=1$ to 10 and $D_D L_B^2$ is correspondingly increased by a factor of 100, say from 10^{-3} to 10^{-1}, then $-\Delta V_{OC}$ would be increased from 0.147 mV to 78.349 mV. This would substantially nullify the expected improvement of V_{OC} when L_B is increased or the minority carrier lifetime is improved by some processing or annealing procedures.

On the other hand, if a cell has some defects across the BSF junction, loss of lifetime or diffusion length due to radiation or other reasons may not decrease the open-circuit voltage as much as a cell which has no defects across the BSF junction. This is for the reason that V_{OC} is already lowered in the defective BSF cell and decrease of L_B would make the defective BSF areas less effective in reaching the front junction to increase its recombination current. This interesting result indicates that one could increase the radiation resistance or make V_{OC} less sensitive to radiation induced recombination center over a wider range of radiation dose when some localized defective areas are introduced into the BSF junction which would reduce V_{OC} initially but also stablize it with respect to the change of L_B.

4. EFFECT OF BULK DEFECT WITH INTERMEDIATE RECOMBINATION VELOCITY ON OPEN-CIRCUIT VOLTAGE

In practice, the defects across the BSF junction may not be completely short-circuiting the BSF junction electrically. In addition, some defective BSF junction areas may contain a high concentration of defects or recombination centers which are distributed in the entire layer of the high-layer (n+ layer of a n/n+ BSF junction or p+ layer of a p/p+ BSF junction). These and other defective BSF junction areas can be represented by an effective surface or interface recombination velocity across a defective area, S_D. This was included in the current densities for Regions II and III given by (9) and (10) in section 2. S_D is the effective surface recombination velocity of minority carrier at the boundary plane on the base side of the space-charge layer of the low-high junction. It includes all the recombination in the space-charge layer of the low-high junction as well as the recombination in the high-layer and on the contact surface of the back metal-semiconductor contact.

It is evident from (9) and (10) that the proper normalization for S_D is $D_B/L_B=\sqrt{D_B/\tau_B}$ which is the minority carrier diffusion or recombination velocity in the base layer. Physically, we can consider the two recombination processes in the two regions, base and BSF regions, as two serial processes. If base recombination is large, then it dominates. If S_D is large, we have two possible situations: thin and thick base. For thin base, $X_B \ll L_B$, then S_D dominates but the recombination current is determined by base thickness. For thick base, base recombination dominates and S_D will have little effect.

The dependence of the reduction of the open-circuit voltage on the BSF defect surface recombination velocity is illustrated by a family of curves shown in Fig. 3.9. In this figure, $A_D/L_B=10^{-4}$, $D_D L_B^2=0.1$, $L_I=2L_B$ and $S_D/(D_B/L_B)$ is the constant parameter with a range of 0.01 to 100. The reduction of the

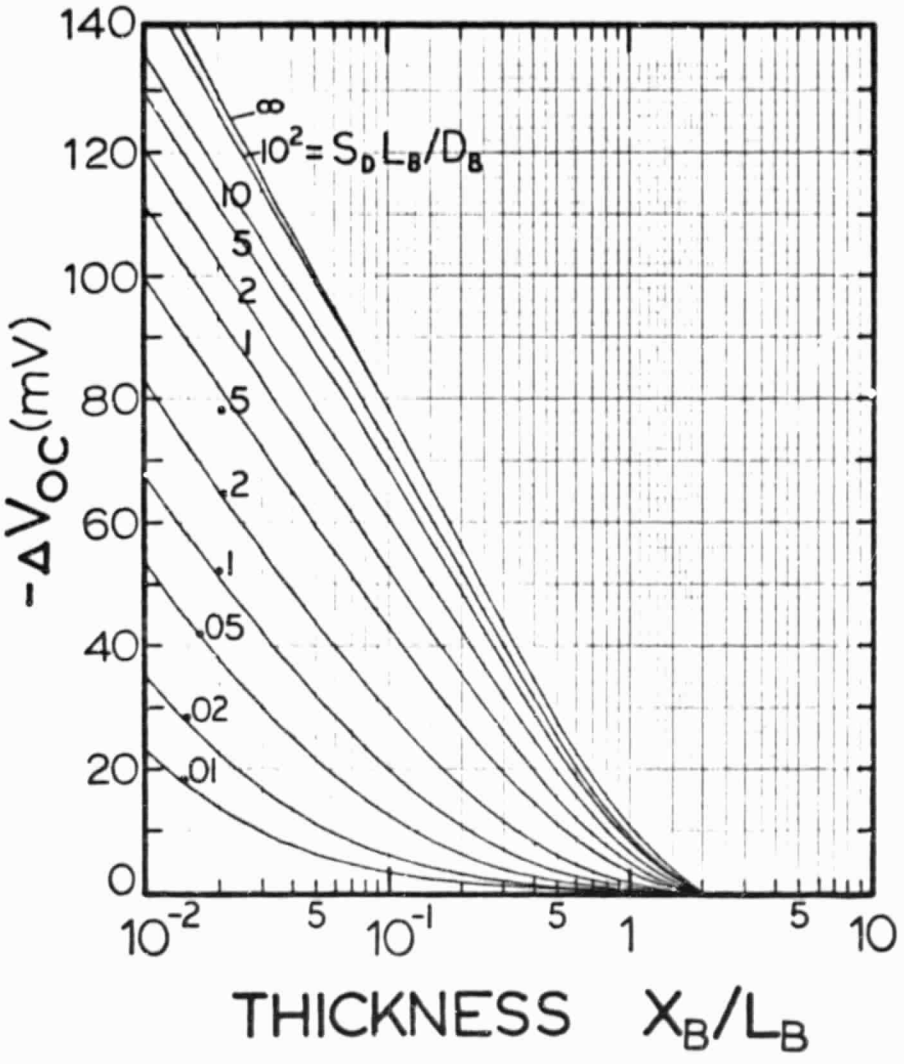

Fig. 9 The reduction of the open-circuit voltage of BSF solar cells as a function of cell thickness with the defect surface recombination velocity as the constant parameter.

open-circuit voltage, $-\Delta V_{OC}$, has essentially reached its limiting value when the defective surface recombination velocity is greater than ten times the base diffusion velocity or $S_D > 10D_B/L_B$.

In a practical high efficiency cell, $D_B \approx 10$ cm^2/sec and $L_B \approx 100$ to 1000 μm or 0.01 to 0.1 cm so that D_B/L_B = 1000 to 100 cm/sec. Thus, the limiting or highest $-\Delta V_{OC}$ is reached when S_D is greater than 10^3 to 10^4 cm/sec. This range of S_D is readily attained and exceeded when physical defects are present across the BSF junction. Smaller values are given by defects which are more spread out into the p+ or n+ layer of the low-high junction.

The main point shown in Fig. 3.9 is that reducing the defect surface recombination velocity will not improve V_{OC} or decrease V_{OC} reduction since it is necessary to reduce S_D to less than 100 cm^2/sec to have any significant gain. It is more effective to reduce the defect density or the number of defect than to reduce the defect surface recombination velocity since the base diffusion-recombination velocity of a high efficiency solar cell is rather low, 100 cm/sec to 1000 cm/sec and since in practice, it is difficult to achieve surface recombination velocity of values less than about 100 cm/sec for interfaces and bare or oxidized surfaces and probably more difficult to achieve values equal to or less than this for a defect surface.

The results of bulk defect can also be compared with that of edge defect treated in another paper [3]. At a given $S_D/(D_B/L_B)$ such as 1.0, bulk defect reduces V_{OC} more than edge defect. Consider a small cell to emphasize edge defect. For the same reduction of V_{OC}, S_D of edge defect must be more than ten times that of a bulk defect, again because bulk defects have much larger peripheral areas (Region II) than edge defects.

5. SUMMARY AND CONCLUSION

High-efficiency solar cells contain a low-high back-surface-field (BSF) junction (n/n+ or p/p+) to provide a large potential barrier which prevents the photogenerated and front-junction injected minority carriers from reaching the high-recombination-rate ohmic contact on the back surface. Such an isolation greatly reduces the recombination current and substantially increases the open-circuit voltage and energy-conversion efficiency. The low-high junction or the back-surface field layer is very thin (about 1 μm) and can easily be shunted electrically by material and manufacturing defects introduced during crystal growth and cell fabrication processes. This paper gives a mathematical analysis of the effect of defects, across the back-surface-field junction and located away from the cell edge, on the solar cell performance. Analysis of the edge defect is given in another paper [3].

In this paper, several families of design curves are presented which show how much the open-circuit voltage of a back-surface-field solar cell is reduced as a function of the cell thickness, defect area, defect density and interface or surface recombination velocity at the defective area.

The defects across the BSF junction are randomly distributed and have random shapes and sizes which defy exact analytical or numerical solution. The random defects are modeled by an uniform device model which is characterized by three defect parameters: the average defect area, the average defect density (per unit area) and the effective surface recombination velocity of the defective area. A *developed perimeter* device model is employed in order that the approximate one-dimensional analytical diffusion solutions of p/n junction with BSF can be applied to a defective BSF solar cell. In this model, a defective cell with many defects is divided into many one-defect unit cells. A one-defect unit cell is further divided into three regions (Fig. 3.4): a central region,

Region III, which is the projection of the defect onto the front p/n junction plane, and two concentric surrounding or peripheral regions, Region II and I. The one-dimensional solutions are applied to Regions I and III. The cross-section of the middle region, Region II, is developed so that the one-dimensional solution can also be applied to this region of varying thickness. Its width is determined by a distance parameter, L_I, which is the range or the distance of influence of the localized defect. It is the maximum distance at which the p/n junction injection-recombination current can still be influenced by a localized defective BSF junction area. This distance of influence is shown to be about two diffusion lengths of the minority carriers in the base region (Fig. 3.5). The main results of this paper are summarized below.

The reduction of the open-circuit voltage is nearly independent of the defect area when it is smaller than about $0.1L_B^2$ or when its dimension is less than about 30% of the minority carrier diffusion length in the base (Fig. 3.6). This insensitivity on defect area, when the area is small, arises from the fact that a defect will increase recombination and reduce open circuit voltage not only on the front junction area which is the projection of the defective BSF area (Region I) but also the junction area surrounding the projection (Region II). As the defect area decreases, the peripheral recombination area (Region II) will stay relatively constant, giving rise to a defect-area-independent V_{OC} reduction. In practice, there should be little defect-area dependence since in good cells, defects are mainly small size and not likely to be as large as $0.1L_B^2 \simeq 0.1 \times 100^2 = 1000\ \mu m^2$. This also means that small-area defects will be as damaging as large-area defects.

The main influence of the open-circuit voltage reduction comes from the density of the defect (Fig. 3.7). The reduction of V_{OC} increases with increasing defect density since there are more peripheral recombination areas,

one per each defect, when the number of defect in a cell increases. For example, if the fractional defective area is kept constant (such as the 0.01 or 1% curve of the bottom graph of Fig. 3.7) and if a single defect of 100 μm^2 is divided into 100 separate defects of 1.0 μm^2 each, the reduction of the open-circuit voltage will increase substantially because the total peripheral recombination area (sum of Region II) will have increased 100 folds. This general trend will persist even when three-dimensional effects and high-level condition are taken into account as the defect area becomes small and the defect current density increases.

Because of the importance of the perimeter region whose size is given by the range or distance-of-influence, the presence of even one defect of small area across the BSF junction will cause significant reduction of open-circuit voltage of a high-efficiency BSF solar cell. A numerical example showed that if there is 1 defect per cm^2 of cell area in a 320 μm thick BSF state-of-the-art high-efficiency cell (L_B=775 μm, V_{OC}=620 mV and EFF=17%), one would expect a reduction of open-circuit voltage of 5.5 mV. If there are 2 defects per cm^2, the reduction of V_{OC} would increase to 10 mV.

The reduction of V_{OC} due to defects across the BSF junction increases when the cell becomes thinner. This was the initial consideration that motivated this analysis since high-efficiency BSF cells reach their peak efficiencies when the cell thickness is decreased to about $0.1L_B$. The larger reduction of V_{OC} in thinner cells is again due to the lateral influence of the defects which increases recombination in peripheral region that surrounds the defect (Region II in Fig. 3.4) since this region increases in width when the cell gets thinner. As a numerical example, if the state-of-the-art high-efficiency cell just described has a thickness of 80 μm instead of 320 μm, then the reduction of V_{OC} is increased from 5.5 mV to 25.7 mV for 1 defect/cm^2

and from 10 mV to 38.3 mV for 2 defects/cm^2.

Families of design curves on the thickness dependences of V_{OC} are given in Fig. 3.8 with the defect density as the parameter.

Defective areas across the BSF junction may not be complete electric short circuits but shunts with non-zero resistance. This was represented by an interface or surface recombination velocity to characterize the defective area. The effect of the surface recombination velocity on V_{OC} reduction was analyzed which showed that V_{OC} is improved only when it is substantially smaller than ten times the diffusion velocity of the minority carriers in the base, D_B/L_B (Fig. 3.9). For high-efficiency cells, the diffusion velocity is not more than about 100 to 1000 cm/sec. Thus, to have any improvement, the defect surface recombination velocity must be made substantially smaller than 100 to 1000 cm/sec. In practice, a defective region rarely has recombination rate and velocity less than about 1000 cm/sec. Thus, a defective region acts essentially as an electrical short circuit across the BSF junction, otherwise it is a good area. There are few inbetween.

From the results of this analysis, it is evident that material and fabrication defects across the BSF junction of high-efficiency cells can be the major deterrent to high open-circuit voltage and high efficiency even if only a few or even one defect is present across the back-surface-field junction.

6. APPENDIX

6.1 Analysis for Region II Surrounding the Defect

The analyses which led to the current density expressions given by equations (8), (9) and (10) in the text are given in this appendix. For Regions I and III, the current density equations, J_1 and J_3, are the standard solutions of a p/n junction with a BSF junction whose surface recombination velocity is 0 (Region I) and S_D (Region III which has the defect). These solutions are one-dimensional low-level diffusion solution in the quasi-neutral base region of a p+/n/n+ or a n+/p/p+ diode with a constant bulk impurity concentration. The surface recombination velocity, S_D, of the defect in Region III can be thought of as an effective recombination velocity if a refined model is needed to represent defects which are extended into the n+ or p+ layer of the BSF junction or point defects or small defect clusters which are distributed in this layer. In such cases, S_D is given by [4]

$$S_D = (D_+/L_+)(P_+/P_B)\,\frac{[\sinh(X_+/L_+) + (S_+L_+/D_+)\cosh(X_+/L_+)]}{[\cosh(X_+/L_+) + (S_+L_+/D_+)\sinh(X_+/L_+)]} \qquad (A.1)$$

where D_+, L_+, and P_+ are the diffusivity, diffusion length and concentration of the minority carriers in the heavily doped n+ or p+ layer. X_+ is the thickness of the n+ or p+ layer and S_+ is the surface recombination velocity of the ohmic contact on the back surface of the semiconductor. P_B is the minority carrier concentration in the quasi-neutral base region. Because of the very large ratio of P_B/P_+ since the BSF layer is much more heavily doped than the base layer, S_D is quite small due to the reduction by the factor (P_+/P_B). This factor represents the Boltzmann factor of the potential barrier height across the low-high junction. As a numerical example, D_+=1 cm^2/sec, L_+= 1 μm, $(D_+/L_+)=10^4$ cm/sec, $P_+=10^{20}/10^{19}=10$ cm^{-3} and $P_B=10^{20}/10^{15}=10^5$ cm^{-3}. Then, $(D_+/L_+)(P_+/P_B)=10^4(10/10^5)=1$ cm/sec. The fraction in (A.1) involving the hyperbolic functions is of the order of 1 so that S_D cannot be substantially

larger than 1 cm/sec.

If there is substantial recombination in the space charge region of the low-high junction, then the total S_D would be the sum of that given by (A.1) and the effective surface recombination rate of the space charge layer, S_{SC}, which is approximately given by thickness of the space charge layer divided by the lifetime, $S_{SC}=W_{SC}/\tau_{SC}=c_{sc}N_{TT}W_{SC}=c_{sc}N_{TTS}$ where c_{sc} is effective capture rate of electrons and holes in the space charge layer (cm^3/sec), N_{TT} is the volume density of the recombination centers in the space charge layer, and N_{TTS} is the areal density of the recombination center averaged over the entire volume of the space charge layer and W_{SC} is the thickness of the space charge layer. S_{SC} is also not too large, for example, if W_{SC}=1 μm, τ_{SC}=1 μs, then, S_{SC}=100 cm/s.

Thus, these examples show that these distributed defects in the BSF layer and BSF junction can essentially be considered as perfect BSF junctions since their effective surface recombination velocity is less than about 1000 cm/sec and they will have rather small effect on the reduction of the open circuit voltage. The large reduction of V_{OC} comes from more serious defects which are essentially short circuits across the BSF junction.

The analysis for Region II is aided by the *developed perimeter* model shown in Fig. 3.4(c) where x is the coordinate perpendicular to the p/n junction and y is the coordinate along the direction joining the nearest neighbor defects in the plane of the p/n junction. X is the variable thickness of the base of Region II and is a function of y, X=X(y). The total current in Region II is then

$$I_2 = \int_0^{W_2} J_{II}(X,y)dy \; Z_{II} \qquad (A.2)$$

where Z_{II} is the effective length or the circumference of Region II while W_2 is its width given by (1) which is repeated below.

$$W_2 = \sqrt{L_I^2 - X_B^2} \qquad (A.3)$$

The one-dimensional low-level dark diffusion current density is given by

$$J_{II}(X,y) = q(D_B P_0/L_B) \frac{[\sinh(X/L_B) + (S_D L_B/D_B)\cosh(X/L_B)]}{[\cosh(X/L_B) + (S_D L_B/D_B)\sinh(X/L_B)]} \qquad (A.4)$$

where D_B, $L_B=\sqrt{D_B\tau_B}$ and τ_B are the diffusivity, diffusion length and lifetime of the minority carriers in the quasi-neutral base at low injection levels. P_0 is the excess minority carrier concentration at the base-side edge of the p/n junction and is given by

$$P_0 = P_B[\exp(qV/kT) - 1] \qquad (A.5)$$

where P_B is the minority carrier concentration in the base, q is the magnitude of the electron charge, k is the Boltzmann constant and T is the cell temperature. S_D was defined in (A.1).

In order to get an explicit analytical solution for the total current flowing in region II from (A.2), a linear approximation is made to the quadratic relations between the variable base thickness, X, and the position y, so that (A.2) can be integrated analytically using the current density expression given by (A.4). The exact quadratic relations is given by $X^2 = X_B^2 + y^2$ as evident from the geometry shown in Figs. 3.4(b) and (c). The linear approximation is given by

$$X \simeq x = X_B + [(L_I - X_B)/\sqrt{L_I^2 - X_B^2}]\, y \qquad (A.6)$$

so that the end points are correct and correspond to those shown in Fig. 3.4(d):

$$X = x(y=0) = X_B$$

and

$$X = x(y=W_2=\sqrt{L_I^2 - X_B^2}) = L_I$$

The difference between the exact quadratic and the approximate linear relations was demonstrated to be small in analyzing the edge defects [3], giving a maximum error of less than 14%. Similarly small errors would be expected here for bulk defects across the BSF junctions.

The analytical solution of I_{II}, using the linear approximation of (A.6) and the current density given by (A.4) in the integral (A.2), is

$$I_2 = qD_BP_0[\sqrt{L_I^2-X_B^2}/(L_I-X_B)]Z_{II}\ \log_e\left[\frac{\cosh(L_I/L_B) + (S_DL_B/D_B)\sinh(L_I/L_B)}{\cosh(X_B/L_B) + (S_DL_B/D_B)\sinh(X_B/L_B)}\right] \quad (A.7)$$

The asymptotic solution of (A.7) for $S_D=\infty$ approaches the correct limit, however, the solution for $S_D=0$ is incorrect since in this case, there would be no V_{OC} reduction and (A.7) should reduce to the form of a constant J_{II} or constant base layer thickness which are

$$J_{II}(X=X_B,y) = q(D_BP_0/L_B)\ \tanh(X_B/L_B) \quad (A.8)$$

and

$$I_2(S_D=0) = q(D_BP_0/L_B)\ \tanh(X_B/L_B)\ A_2 \quad (A.9)$$

where A_2 was given in (12). But, (A.7) does not reduce to (A.9).

In view of the approximations already made, we shall remedy this by another approximation so that the limiting solutions are correct. This is achieved by replacing the two cosh terms in (A.7) by exponential terms so that they give the correct solution of (A.9) when $S_D=0$. The replacements are: $\cosh(L_I/L_B)$ replaced by $\exp[(L_I/L_B)\tanh(X_B/L_B)]$ and $\cosh(X_B/L_B)$ replaced by $\exp[(X_B/L_B)\tanh(X_B/L_B)]$. The new approximate solution for the total current in Region II which gives the correct asymptotic result when $S_D=0$ is then

$$I_2 = q[D_BP_0\sqrt{L_I^2-X_B^2}/(L_I-X_B)]Z_{II}\ x$$
$$\log_e\left[\frac{\exp[(L_I/L_B)\tanh(X_B/L_B)] + (S_DL_B/D_B)\sinh(L_I/L_B)}{\exp[(X_B/L_B)\tanh(X_B/L_B)] + (S_DL_B/D_B)\sinh(X_B/L_B)}\right] \quad (A.10)$$

This can then be simplified to the form given by (5) with J_2 defined by (9).

6.2 Uniform Models for Square and Circular Defects

In Figure 3.4 we have illustrated the developed perimeter model of a square unit cell which contains a square-shaped defect. We shall show that the results obtained in the text are also applicable to a square unit cell which contains a circular-shaped defect if the width of Region II is redefined and allowed to overlap into the four adjacent unit cells. The results listed in (11), (12) and (13) for the areas of the three regions of a square defect are derived as follows. From Fig.3.4(a) and (b), it is evident that $A_2+A_3=(2W_2+\sqrt{A_3})^2$ for a square defect of area A_3 and side $\sqrt{A_3}$ where $W_2=\sqrt{L_I^2-X_B^2}$ is the width of Region II. Since the unit cell area, A_0, is given by the sum of the area of the three regions, $A_0=A_1+A_2+A_3$ and the defect density is given by $D_D=1/A_0$, then the areas of Region II and I can be expressed by the defect density, D_D, and the defect area A_3 which will use the symbol A_D. Thus, $A_1=A_0-(A_2+A_3)$ and $A_2=(2W_2+\sqrt{A_3})^2-A_3$ or

$$A_1 = D_D^{-1} - A_D[1 + 2(W_2/\sqrt{A_D})]^2 - A_D \qquad (A.11)$$

$$A_2 = A_D[1 + 2(W_2/\sqrt{A_D})]^2 - A_D \qquad (A.12)$$

$$W_2 = \sqrt{L_I^2 - X_B^2} \qquad (A.13)$$

(A.12) reduces to (12) if W_2 given by (A.13) is substituted into (A.12) and noting that we wrote $A_D=A_3$. The length of Region II, Z_{II}, is defined by $A_2=W_2Z_{II}$ which may be equated to (A.12) of (12) to give $Z_{II}=4(W_2+\sqrt{A_D})=4(\sqrt{L_I^2-X_B^2}+\sqrt{A_D})$. In the final results given by (4) to (13), Z_{II} does not enter explicitly.

For a circular or round defect in a square unit cell, the results are readily obtained in the same way as above and are given by

$$A_1 = D_D^{-1} - A_D[1 + \sqrt{\pi}(W_2/\sqrt{A_D})]^2 - A_D \qquad (A.14)$$

$$A_2 = A_D[1 + \sqrt{\pi}(W_2/\sqrt{A_D})]^2 - A_D \qquad (A.15)$$

$$W_2 = \sqrt{L_I^2 - X_B^2} \qquad (A.16)$$

The factor, 2, in (A.11) and (A.12) for a square defect is replaced by $\sqrt{\pi} = 1.77$ for a circular or round defect shown in (A.14) and (A.15). Thus, if we redefine the width of Region II, W_2, by $W_2' = \sqrt{\pi/4}\, W_2 = 0.866 W_2$, then the areas A_1 and A_2 for the round defect have the same expressions as those for the square defect.

6.3 Randomly Distributed Defects

The developed perimeter device model for a defective unit cell shown in Fig. 3.4 for a square-shaped defect and a square unit cell can be extended to randomly distributed defects with random distribution of defect area. The results obtained in the text in terms of the defect density and area are still applicable if these are average density and area over the random distributions and if there is a sufficient number of defects so that statistical average is meaningful. In practice, there are few defects in high-efficiency silicon solar cells manufactured under controlled conditions so that the discrete model of one or few defects uniformly distributed which was described in Fig.3.4 should be a better approximation than a randomly distributed model of many defects.

Two brief and simple illustrations are given to show how the device model can be extended to random defects. It should be noted first that the extension to random defects is considerably simplified using the three-region defect model since it is developed to use the one-dimensional solutions in all three regions. Thus, the only random parameters that need to be averaged statistically are the areas of the three regions, A_1, A_2 and A_3. These areas do not interact with the current densities and the minority carrier distributions in these three regions due to the one-dimensional approximation which would have required the solution of the three-dimensional diffusion equation with random boundary conditions.

Consider first the simplest case in which the defect area, A_D, is varied but still maintains a square shape and constant density or uniform separation. In this case, a statistical average needs to be carried out for the areas A_1, A_2 and A_3 or A_D over the random distribution of A_D using the expressions given by (A.11) and (A.12) or (11) and (12) for A_1 and A_2 which are functions of A_D. The averaged areas, $\bar{A}_1$, $\bar{A}_2$ and $\bar{A}_3=A_D$, are to be used to compute the total current in the three regions using (4), (5) and (6), and the open-circuit reduction using (16). $\bar{A}_1$ is given by $D^{-1} - \bar{A}_2 - A_D$ so that only $\bar{A}_2$ needs to be evaluated. From (12) or (A.12), it is evident that we need to compute the statistical average of $\sqrt{A_3}$. If we assume that the size or the edge of the defect, $Z_3=\sqrt{A_3}$, is randomly distributed, then $\overline{\sqrt{A_3}} = \bar{Z}_3$ and $A_D=\overline{(Z_3^2)}\simeq(\bar{Z}_3)^2$.

Consider next a more complicated example in which the defect spacing is randomly distributed. Let the defect area be constant and square and let their sides be parallel to the x or y axis. Then, the area A_2 given by (A.12) or (12) needs to be modified since Region II from adjacent square unit cells may overlap and counted twice. This overlap area must be subtracted out of (12) or (A.12). To get an expression of the random size of the overlap area, let us denote the center-to-center spacing between the adjacent unit cells by S_x and S_y along x and y directions and S_x and S_y are random variables. Then, there will be no overlap when $S_x > 2W_2+Z_3$ and $S_y > 2W_2+Z_3$ where $Z_3=\sqrt{A_3}=\sqrt{A_D}$. Denote this non-overlap separation by $S_L=2W_2+Z_3$, then the overlap area between the two adjacent square unit cells is given by $A_{22} = (S_L-S_x)(S_L-S_y)$. The non-overlap area of Region II for each unit cell is then $A_2 - A_{22}$. If the spacing is still smaller such that some of the overlapped area spreads into Region III, then it must be subtracted out of A_{22} or the net non-overlap area of Region II is $A_2-A_{22}+A_{32}$ where A_{32} is the area of Region III which is overlapped

by the Region II from an neighboring unit cell. The area which must be used to compute the current flowing in Region II using (5) is now the statistical average of $A_2-A_{22}+A_{32}$ over the random distribution of S_x and S_y which vary from 0 to ∞ or to the dimension of a cell.

From these two examples, the procedure for extension to more general random distributions of defect density and area as well as shape is evident, although the algebra is somewhat complicated. They also demonstrate the simplicity of treatment for random defects from the use of the three-region developed perimeter device model for the defect.

7. REFERENCES

1. C. T. Sah, P. C. H. Chan, C. K. Wang, R. L. Y. Sah, K. A. Yamakawa and R. Lutwack, "Effect of Zinc Impurity on Silicon Solar-Cell Efficiency, " IEEE Trans. Electron Devices, ED-28, pp.304-313, March, 1981

2. J. G. Fossum and E. L. Burgess, "High Efficiency p+/n/n+ Back-Surface-Field Silicon Solar Cells," Applied Physics Letters, 33, pp. 238-240, August 1, 1978; J. G. Fossum, R. D. Nasby and E. L. Burgess, "Development of High-Efficiency p+/n/n+ Back-Surface-Field Silicon Solar Cells," Conference Record of the 13th IEEE Photovoltaic Specialist Conference, pp. 1294-1299, June 5, 1978. IEEE Catalog No. 78CH1319-3.

3. C. T. Sah, K. A. Yamakawa and R. Lutwack, "Reduction of Solar Cell Efficiency by Edge Defects Across the Back-Surface Field Junction: - A Developed Perimeter Device Model," to be published.

4. Michael P. Godlewski, Cosmo R. Baraona and Henry W. Brandhorst, Jr., "Low-High Junction Theory Applied to Solar Cells," Conference Record of the 10th IEEE Photovoltaic Specialist Conference, pp.40-49, 1978. IEEE Catalog No. 73CH0801-ED.

IV. THICKNESS DEPENDENCES OF SOLAR CELL PERFORMANCE#

1. INTRODUCTION

Decreasing the semiconductor thickness of junction solar cells not only reduces the semiconductor material cost but also improves the efficiency if the cell has a back-surface field and is not too thin: - not less than about one average optical absorption length ($\sim$ 10 μm in Si) or about one tenth of the base carrier diffusion length in high-efficiency cells ($\gtrsim$16% AM1 in Si). The improvement in thin cells arises from the smaller minority carrier recombination volume when the cell is thin. Large number of curves on the performance of solar cells as a function of thickness have been computed and given by Hovel [1] for cells on silicon and other semiconductors. The performance parameters presented include the open-circuit voltage, V_{OC}, the short-circuit current density, J_{SC}, the fill factor or curve factor, FF, and the efficiency, EFF, for both space (AM0) and terrestrial (AM1) solar illuminations.

The theory used by Hovel was the analytical one-dimensional low-level p/n junction diode theory, including emitter space-charge-layer recombination current. Because of the low-level assumption, some important features of the dependences of these performance parameters on the thickness of the cell are missing in his families of curves. Two most obvious ones are: (i) base resistivity loss when the cell is thick (above about 100 μm), when the resistivity is high and when the solar intensity and cell current are high (concentrator photovoltaic energy conversion) and (ii) emitter and back-surface-field layer recombination when the cell is very thin. These factors are related to high injection level effects which cannot be taken into account readily using low-level analytical theory of minority carrier diffusion and drift in p/n junctions such as those employed by Hovel and later workers. In addition to these two effects not taken into account by the low-level

---

This chapter will be published as an article in Solid-State Electronics in 1982 with the same title. It has been accepted for publication.

theory, there are some additional high-level effects which are dependent on specific material properties, such as the variation of the diffusivity and lifetime of the minority carriers in the base layer with injection or illumination level. The purpose of this short note is to demonstrate the importance of these two universal effects on the performance parameters, in particular, the fill factor and the efficiency.

2. DEVICE MODEL

The one-dimensional device equations were numerically solved using the transmission line technique [2]. The input parameters are the dopant impurity concentration profile, the variation of the electron and hole mobility with dopant concentration, the concentration and the thermal capture and emission rates of electrons and holes at the recombination center, the deveice temperature, the AM1 solar irradiance spectra and the silicon absorption coefficient. Complete transmissions at the front and back surfaces of the cell are assumed. A model recombination center of zinc is used although the results are generally valid for other recombination centers and for assumed minority carrier lifetimes. The latter is a procedure most frequently used by solar cell theorists. The device structure parameters used in our numerical analysis are identical to those used in reference [2].

3. ANALYSIS OF RESULTS AND COMPARISONS WITH LOW-LEVEL THEORY

The results of our calculations for the intrinsic cell [3] are presented in Figs. 1 to 4 which contain open-circuit voltage, short-circuit current fill factor and efficiency as a function of cell thickness from 10 to 1000 μm. Both a back-surface-field (BSF) n+/p/p+ and a back-surface-ohmic (BSO) n+/p cell structure are computed. The recombination center density selected, 10^{12} Zn/cm^3, gives a minority carrier diffusion length of about 577 μm. This was chosen to simulate current state-of-the-art high-efficiency silicon solar cells whose

residual recombination center could be an impurity-vacancy complex. However, the minority carrier diffusion length of a production high-efficiency cell will be similar to that assumed in this numerical example. The resistivity of the p-type silicon used in this example is about 25 ohm-cm or a dopant impurity concentration of 5×10^{14} boron/cm^3.

The open-circuit voltage and the short-circuit current are given in Figures 1 and 2. These curves can be compared with those given by Hovel based on the one-dimensional low-level analytical theory. For ease of comparison, Hovel's curves of V_{OC}, J_{SC}, FF and EFF are reproduced here in Figure 5. It is evident that our exact numerical solutions for V_{OC} and J_{SC} have thickness dependences very similar to those giver by Hovel, shown here as Fig. 5(a) and 5(b). The magnitude difference between Hovel's and our J_{SC} [compare Figure 1 with Figure 5(a)] comes from the differences in the solar spectra used since his AM2 spectrum has a slightly lower intensity than our AM1 spectrum. given in reference [2]. The resistivity (10 ohm-cm vs our 25 ohm-cm) and diffusion length (232 μm vs our 577 μm) differences contributed to the differences in V_{OC}. The main feature is that the thickness dependences of these two parameters, J_{SC} and V_{OC}, are not very different using the low-level (Hovel) and the exact (our) solutions.

The similarity ceases for the other two performance parameters, the fill factor and the efficiency. The differences in the fill factor is particularly important in pointing out the series resistance effect and the high injection level effect which are the principal causes of low efficiency in thin film cells. The fill factor and the efficiency are given in Figures 3 and 4 which may be compared with the low-level results given in Fig. 5(b) and 5(c).

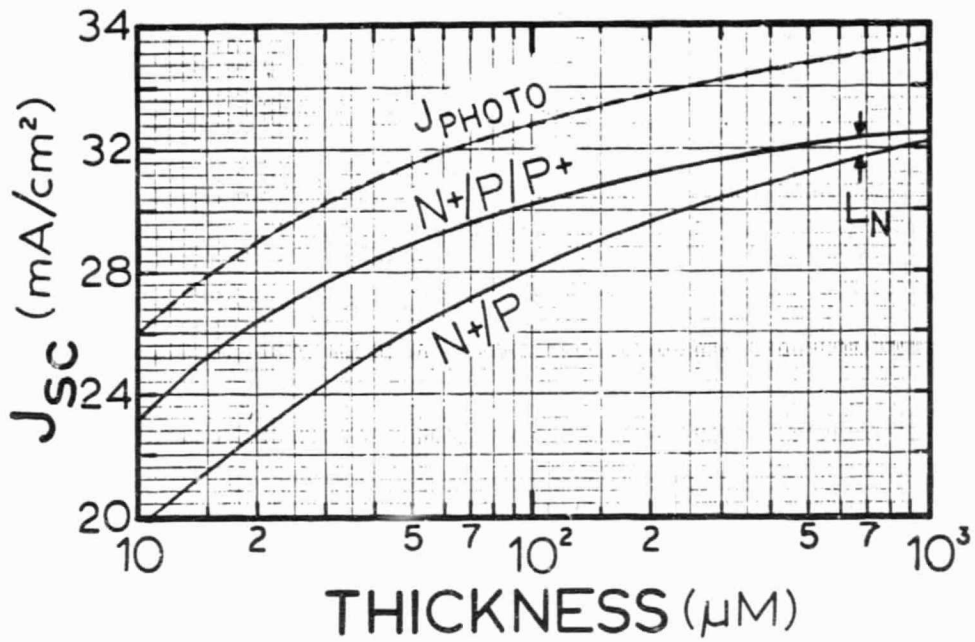

Fig. 1 The short-circuit current density at AM1 in a BSF silicon n+/p/p+ and a n+/p solar cell as a function of cell thickness. The total available photo current is also given. These are computed from the exact solution of the Shockley Equations. The base diffusion length is 577 μm.

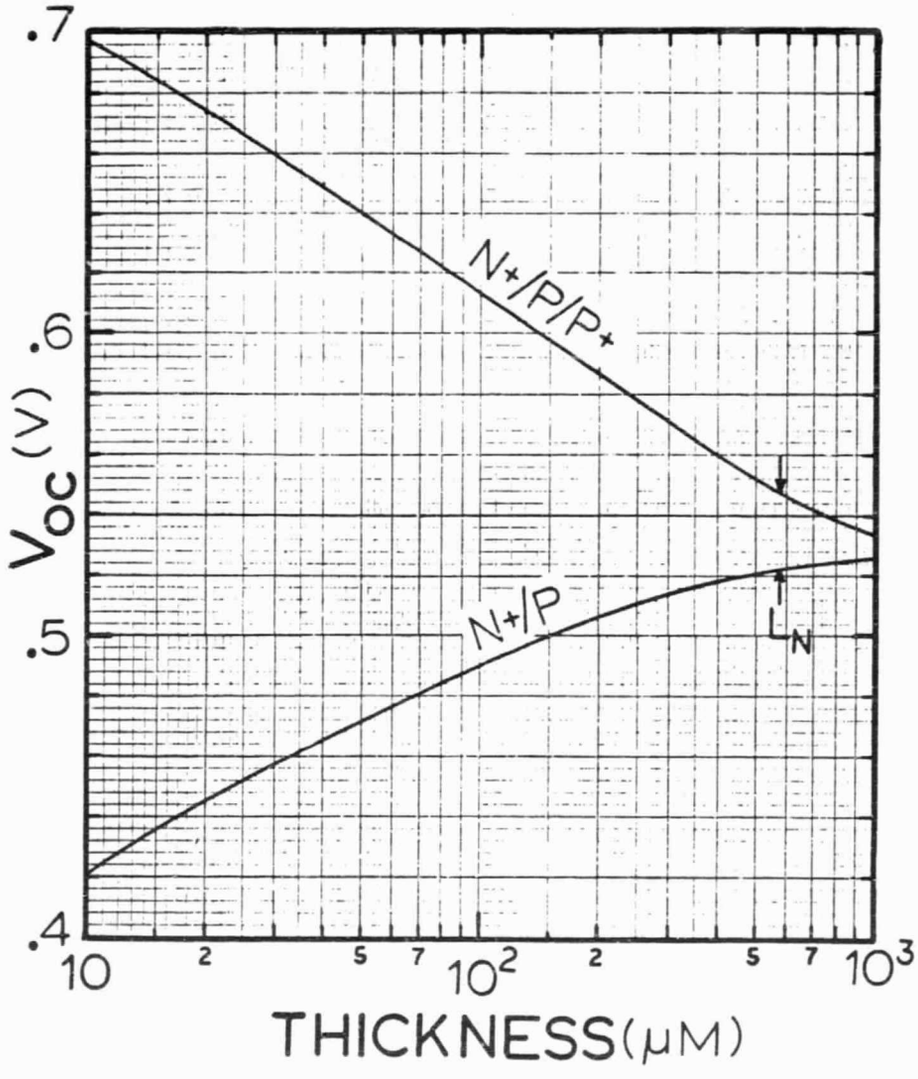

Fig. 2 The open-circuit voltage at AM1 in a BSF n+/p/p+ and BSO (Back-Surface-Ohmic) n+/p silicon solar cell as a function of cell thickness.

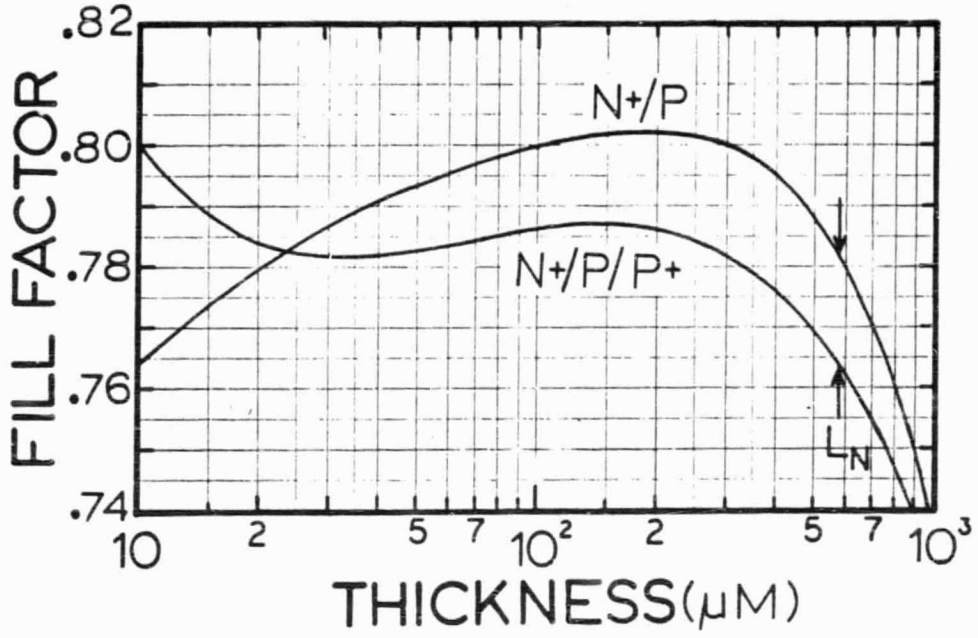

Fig. 3 The fill factor at AM1 in a BSF n+/p/p+ and a BSO n+/p silicon solar cell as a function of cell thickness.

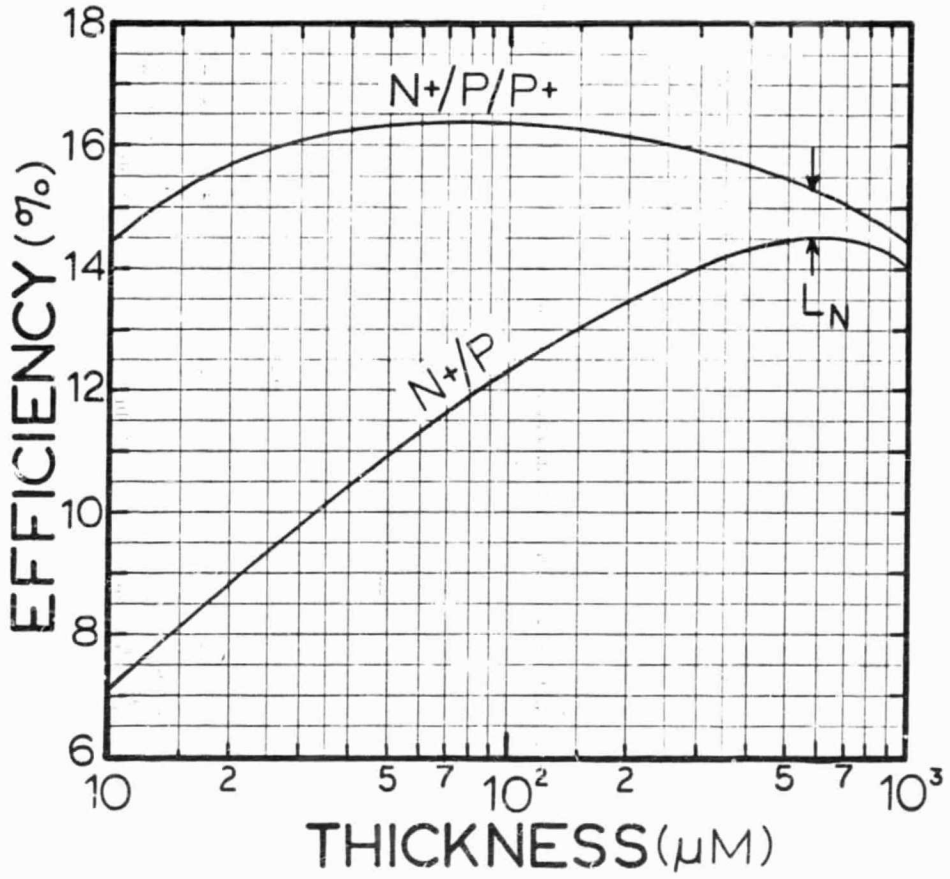

Fig. 4 The AM1 efficiency of a BSF n+/p/p+ and a BSO n+/p silicon solar cell as a function of cell thickness.

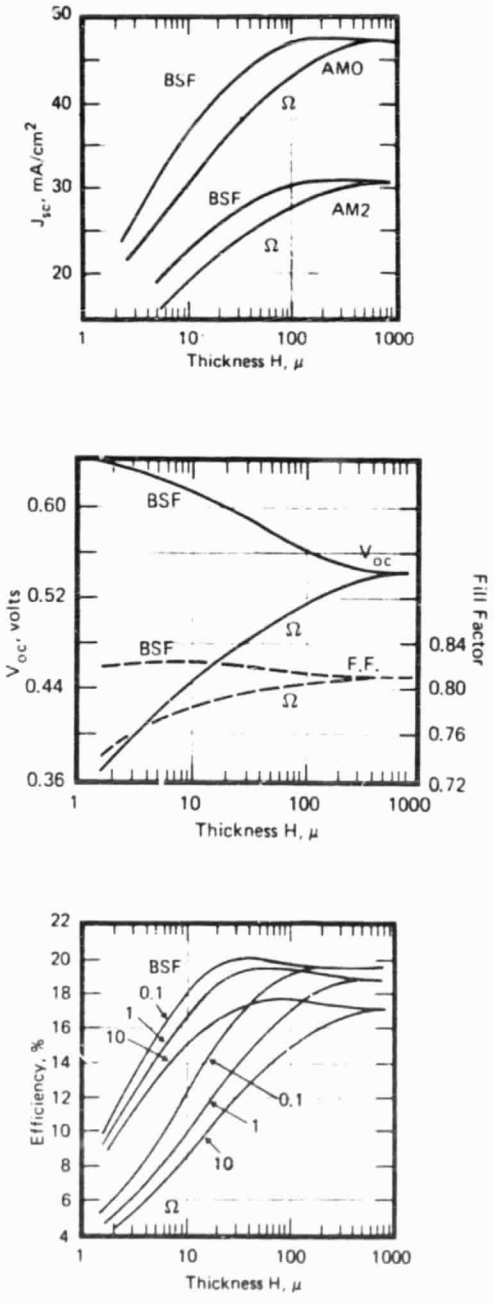

Fig. 5 The short-circuit current, the open-circuit voltage, the fill factor, and the efficiency at AM1 in silicon BSF and BSO solar cells as a function of cell thickness computed from the one-dimensional low-level analytical theory by Hovel [1].

Comparison of Fig. 5(b) with Figure 3 shows that there are marked differences in the fill factor computed from the low-level approximation and the exact numerical solution. The three main differences are listed below.

(1) The BSF cell (n+/p/p+) has a lower fill factor than the BSO (n+/p) cell when the thickness is greater than about 25 μm or about $0.043L_B$ (L_B=577 μm). The low-level approximation predicts just the reverse over the entire thickness range: FF in the BSF cell is always higher than the BSO cell.

(2) The fill factor peaks between 100 and 300 μm from the exact theory and drops rapidly when the cell thickness increases about 400 μm or $0.5L_B$. The low-level approximation shows that the FF flattens out to a constant and ideal diode value when the thickness is greater than 200 μm and maintains this constant even at infinite thickness.

(3) The fill factor of the BSF cell increases towards the ideal diode value when the thickness is less than about 25 μm while that of the BSO cell decreases continually as the thickness decreases. The low-level theory does not show a significant reversal of the FF in the BSF cell while in the BSO cell it decreases continually when the thickness decreases.

These differences can be accounted for by the majority carriers and high-level injection which are neglected in the low-level minority carrier diffusion theory. The differences given in (1) is due to the fact that high injection level condition sets in in the base of the BSF cell earlier than the BSO cell because the photogenerated minority carrier density in the base of the BSF cell is higher while it is lower in the BSO cell because of the high recombination rate at the ohmic contact of the BSO cell. This difference cannot be accounted for by

refinement of the low-level theory short of including the high level effect.

The difference stated in (2) is due to the large series bulk resistance of the majority carriers when the cell is thick. In the exact numerical solution, this bulk resistance is automatically included while in the low-level minority carrier diffusion theory, it is not included since the majority carriers are excluded in the low-level analysis. The low-level theory can be refined to take into account of the bulk series resistance very approximately if an equivalent resistance is added in series with the ideal one-dimensional cell and this external series resistance is made proportional to the cell thickness.

The increase of the fill factor of the BSF cell towards the ideal diode value (above 0.8) in Figure 3 as the cell thickness decreases (item 3) is due to the increasing dominance of emitter recombination when the cell is very thin since base recombination volume decreases with cell thickness. In our example, the emitter thickness is fixed at 0.25 μm. The reason for reaching the ideal diode value is that the emitter is heavily doped and hence almost always at the low-level condition of an idea diode.

For the BSO cells, the fill factor decreases with decreasing thickness in both the exact and approximate theories [Fig. 3 and Fig. 5(b)]. This is due to the decreasing open-circuit voltage as the cell becomes thinner. One can readily show that the FF values given in these figures are nearly equal to those predicted by the ideal low-level base recombination theory, $I_{SC}=I_0\exp(qV_{OC}/kT)$.

There are also differences in the AM1 efficiency obtained by the exact numerical and the approximate analytical theories, particularly when the cells are thick. This is illustrated by comparing Figure 4 with the 10 ohm-cm curves in Fig. 5(c). For thick cells, the low-level theory predicts a constant efficiency while the exact numerical solution shows that the efficiency decreases continually with increasing thickness. This is due to the series bulk resistance effect which is not taken into account in the ideal analytical theory.

4. REFERENCES

1. Harold J. Hovel, Solar Cells, Academic Press, 1975, Chapter 5.
2. C. T. Sah, P. C. H. Chan, C. K. Wang, R. L. Y. Sah, K. A. Yamakawa, R. Lutwack,"Effect of Zinc Impurity on Silicon Solar-Cell Efficiency," IEEE Transaction on Electron Devices, ED-28, 304-312, March 1981.
3. Series bulk resistance is automatically included in the exact one-dimensional intrinsic cell model employed by us. Contact resistance is assumed to be zero. Lateral resistance loss due to front metal grid lines is a two-dimensional effect not accoutable by the one-dimensional model used in our one-dimensional model.

5. ACKNOWLEDGEMENT

The author would like to thank Fred A. Lindholm for several suggestions to improvement the manuscript and an anonymous reviewer for Solid-State Electronics whose detailed comments were taken into account in the revised manucript given here.

V. THERMAL RECOMBINATION AND GENERATION PROPERTIES OF ELECTRONS AND HOLES AT THE DOUBLE DONOR TITANIUM CENTER IN SILICON

1. INTRODUCTION

To achieve high energy-conversion efficiency at a reasonable price in silicon solar cells, the densities of the residual metallic impurities in the starting silicon material must be reduced at a refinement cost which is consistent with the price-performance economics requirement of silicon solar cells in competition with other energy sources. High recombination rates of electrons and holes at the residual impurity centers in silicon will severely limit the highest efficiency that is achievable in a solar cell containing these residual impurities. The starting metallurgical grade silicon material contains many metallic impurities at high concentrations. These impurities must be removed by chemical refinement processes before single silicon crystals can be grown. The various crystal growth processes can also remove a significant fraction of the remaining impurities but it is more economical to remove most of the residual metallic impurities by a prior chemical refinement process which is the proven and traditional purification sequence in the production of integrated circuit grade silicon single crystals.

The importance of achieving low residual metallic impurity concentration in order to reach the highest energy conversion efficiency in silicon solar cells is only recognized recently [1]. In fact, the purity requirement on solar grade silicon for high efficiency performance (>17% AM1) is even more severe than the highest quality silicon single crystal required for the current and future high-density very-large-scale high-performance integrated circuits. Thus, it is important to determine accurately what is the absolute concentration of an impurity that can be tolerated in a highest-efficiency silicon solar cell

design when the efficiency of the cell is specified by the economics requirement of a praticular application, such as terrestrial or space power generation. In order to provide this information, the electronic properties of the residual impurity in a single crystal silicon must be accurately known so that a first-principle computer calculation can be carried out for a particular solar cell design to determine the relationship between the cell performance (such as short-circuit current density, J_{SC}, the open-circuit voltage, V_{OC}, fill factor, FF, and maximum energy conversion efficiency, EFF) and the concentrations of the metallic impurities. The electronic property that controls the solar cell performance is the thermal recombination rate of electrons and holes since photogenerated electron-hole pairs by solar illumination can produce electrical power only if they are not lost by recombination at the impurity recombination centers. The thermal recombination rates are represented by six parameters which characterize the thermal capture and emission processes of electrons and holes at the localized states produced by the residual impurity centers in a semiconductor. These are the thermal capture rates, c_n and c_p, the thermal emission rates, e_n and e_p, and the thermal activation energies, E_{Tn} and E_{Tp}, of electrons (subscript n) and holes (subscript p) respectively. At thermal equilibrium or low applied electric field in a junction solar cell, the six kinetic parameters are not all independent and only three parameters are needed. The others can be computed using the equilibrium electronic properties of the semiconductor determined by other means; such as $e_n e_p = c_n c_p n_i^2$ where n_i is the known intrinsic carrier density; $E_{Tn}+E_{Tp}=E_G$ where E_G is the energy gap; and $e_n = c_n N_C \exp(-E_{Tn}/kT)$ and $e_p = c_p N_V \exp(-E_{Tp}/kT)$ where N_C and N_V are the effective density of state in the conduction and the valence band respectively.

There are many residual impurities in a metallurgical grade silicon, such as Al (7×10^{19} atom/cm^3), B (6×10^{17}), Ca (1.2×10^{19}), Cr (2×10^{19}), Cu (3×10^{18}), Fe (2×10^{20}), Mg (2×10^{17}), Mn (6×10^{18}), Mo (2×10^{18}), Ni (5×10^{18}), P (5×10^{17}),

Ti (2.5×10^{19}), V (1.2×10^{19}), Zr (2×10^{18}) and others. In addition, impurities can be introduced during the crystal growth, such as oxygen from the molten silicon container made of fused quartz, carbon from the growth ambient, molybdenum and tungsten from the apparatus or container material and others. Impurities can also be introduced during the purification of the metallurgical grade silicon from specific purification processes such as Zn (5×10^{18} to 5×10^{19} Zn/cm^3), Mo and other possible metallic contaminations from the crystal grower or the boat or the container for the molten silicon. Although many of these metallic impurities have very low distribution coefficients between the molten and solid silicon so that their concentration in the solid or the crystal can be many orders of magnitude smaller than that in the melt due to impurity segregation during crystal growth. Such a reduction may still be insufficient to reduce the impurity concentrations to a sufficiently low level so that high-efficiency solar cell can be fabricated. Estimates have been made for Ti based on the preliminary recombination parameter data which indicated that Ti concentration must be less than about 3×10^{12} Ti/cm^3 in a p+/n/n+ BSF (back-surface-field) silicon solar cell in order to get 17% AM1 efficiency. At an equilibrium segregation or distribution coefficient of 2×10^{-6} for Ti in Si, a one-pass crystal growth or zone refining process would reduce the Ti concentration from 2.5 $\times 10^{19}$ Ti/cm^3 in the feedstock Si to about $2.5 \times 10^{19} \times 2 \times 10^{-6} = 5 \times 10^{13}$ Ti/cm^3 along 80 to 90% of the crystal length but this is still too high to give 17% AM1 efficiency. Thus, highly efficient and economical chemical refining processes are needed to purify the metallurgical grade silicon before it is used for single crystal growth. The refining processes must provide a final silicon crystal, single or poly, with less than about 3×10^{12} Ti/cm^3 and similar amounts of other metallic impurities

so that high-efficiency (17%) solar cells can be fabricated.

To determine the electron-hole recombination parameters for each impurity in silicon which may degrade or control and limit the highest acheivable efficiency of the final solar cell requires extensive and detailed measurements. Because of the minute concentration of these impurities, they cannot be detected by conventional analytical or microchemical analysis and neutron activation techniques. In addition, these techniques would only give the total impurity concentration of each species and not their electrically active concentration nor the recombination parameters. Thus, alternative and electrical techniques must be employed. The most sensitive of these are the diode transient techniques which rely on the detection of the minute time dependence of the concentration of the electrons and holes trapped at the impurity centers in the space charge layer of a semiconductor junction. These include many possible variations first proposed by Sah and demonstrated by him and his graduate students [2] and further refined, extended and computerized by them and other workers. A comprehensive review has been given by Miller, Lang and Kimerling [3] who had themselves contributed to many of the refinements and automated data acquisition techniques.

In this report, measurements of the thermal capture and emission rates and thermal activation energy of electrons and holes at the Ti centers in Si are described using two Constant Voltage Capacitance Transient (CVCT) methods. The results are carefully analyzed to show that they are consistent with the double donor model of substitutional Ti center, expected from the electronic shell structure of Ti atom in the tetrahedral covalent bond model of crystalline Si.

A historical review of the recombination parameter measurement data of Ti center is first given which is followed by a summary of what are believed

to be the most reliable or accurate results to date. A theoretical interpretation of these latest results is then given to show that they are consistent with the covalent bond model of silicon and the electronic shell structure of Ti. Here, we present a new method of analyzing the theoretical charge states of an impurity or defect center in a semiconductor based on the equilibrium statistics of the distribution of the trapped electrons and holes and their spin and configuration degeneracy and entropy.

2. HISTORICAL REVIEW OF RECOMBINATION PARAMETER MEASUREMENTS

(A) The first reported measurements of the energy levels or thermal activation energies of Ti related centers in silicon were given by Sah on October 12, 1976 during the LSSA PIM (Low-Cost Silicon Solar Array Project Integration Meeting) sponsered by JPL (Jet Propulsion Laboratory) at Pasadena. At that time, the Impurity Effects on Silicon Solar Cell programs had just started with two major efforts undertaken by Monsanto and Westinghouse Research Laboratories. Single crystal silicon intentionally doped with metallic impurities during crystal growth were produced by Dow Corning for Westinghouse and within Monsanto for this study. Some crystal slices were made available by JPL for our measurements. Two Schottky barrier runs were made quickly using a p-type silicon slice doped with Ti during growth from Westinghouse (Crystal No. W-008-Ti-001). The slice had an elongated quarter-pie shape of approximately 1/8" by 1/2" and 14 mil thickness. Four-point-probe resistivity measurements gave a V/I=16.1 ohms for a probe spacing of 500 μm. The computed resistivity is then $\rho=A(V/I)$ $=0.1575 \times 16.1=4.06$ ohm-cm which is consistent with Westinghouse-provided data of 4.2 to 3.1 ohm-cm. The carrier or hole concentration is then 3.6×10^{15} cm^{-3} at room temperature (300°K). 30 mil diameter Mg dots were evaporated onto the chemically polised side of the surface and a blanket aluminum was evaporated to the back side. 100x100 mil^2 dices with four diodes per dice were cut from

the wafer and mounted onto a 8-pin gold-plated TO-5 header using a low temperature epoxy (Epotek 410). A 30-mil diameter Mg dot on the top surface was then covered with a drop of the same epoxy and a gold preform was used to cover the epoxy dot. This assembly was then cured at 80°C for two hours in a dry nitrogen ambient. After curing, a one-mil gold wire was then bonded to the gold preform ultrasonically and to the post of one of the 8 pins.

VSCTS (Voltage Stimulated Capacitance Spectra) was then taken from 77 to 300°K which revealed three peaks at approximately 90K, 160K and 170K. The two lower temperature peaks were negative, revealing that they were minority carrier or trapped electron emission peaks while the higher temperature (170K) peak was positive and due to thermal emission of holes trapped at a level below the midgap. The minority carrier signals and peaks were obtained by forward biasing the diodes which apparantly gave some electron injection from the Mg metal into the p-Si in the Schottky Barrier diode. A typical capacitance transient decay curve is shown in Fig. 1 which consisted of fast positive transient due to thermal emission of trapped majority carriers (holes in p-Si) at the lower level and a longer negative transient due to thermal emission of trapped minority carriers (electrons) at the upper level.

These capacitance transients were then measured at many temperatures around the three VSCTS peak temperatures and analyzed by a two-exponential nonlinear least-square-fit routine to give both the preexponential factor and the decay rate or thermal emission rate constants, e_p for hole emission and e_n for electron emission. These rate constants were then plotted as a function of 1000/T and least-square-fitted to the Arrhenius equations

$$e_n^t = A_m(T/300)^m \exp[-(E_C-E_T)/kT] \quad \text{(electron emission)} \quad (1)$$

or

$$e_p^t = A_m(T/300)^m \exp[-(E_T-E_V)/kT] \quad \text{(hole emission)} \quad (2)$$

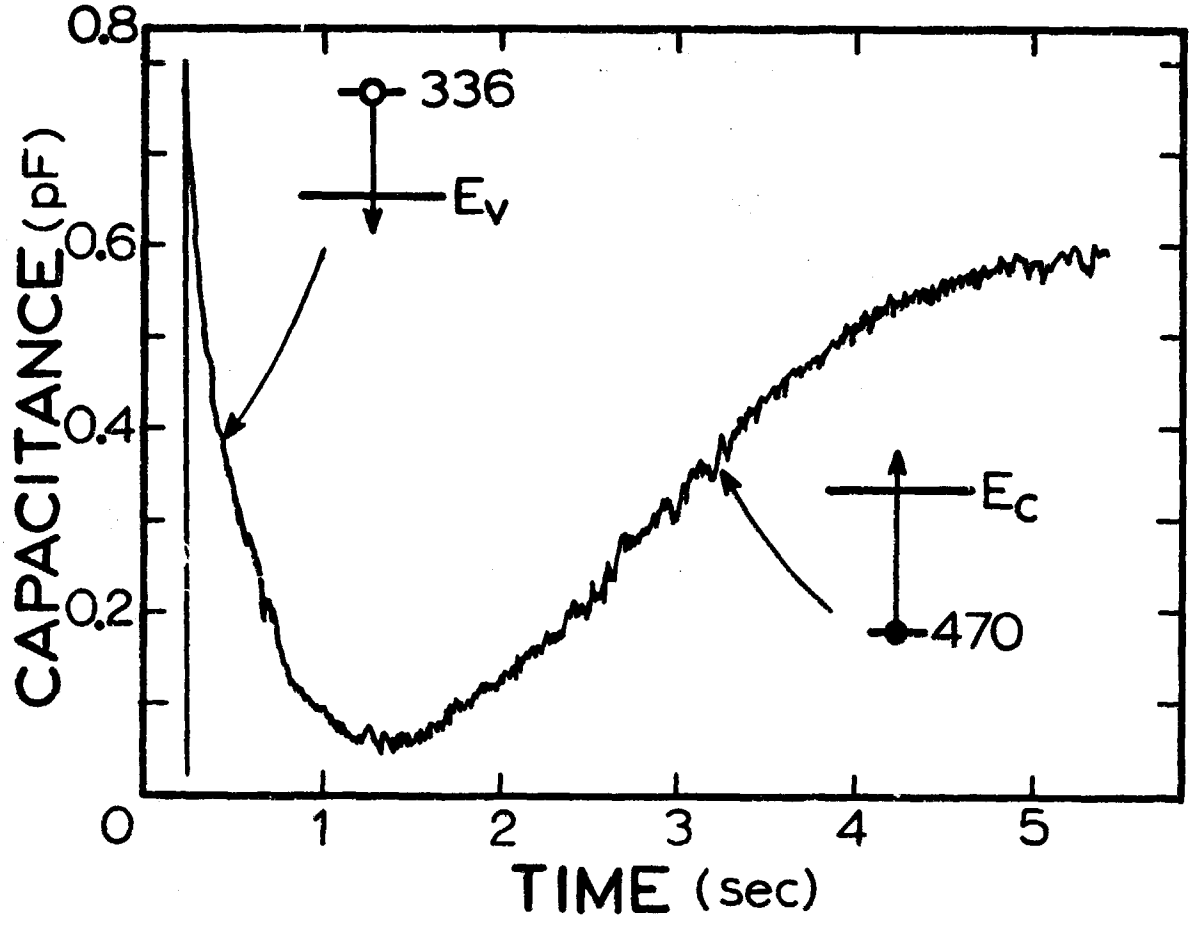

Fig. 1 A typical capacitance transient of a Mg/p-Si Schottky barrier diode on Ti-doped silicon. Crystal W-008-Ti-001.

The experimental results were represented by the following equations for the thermal emission rates and activation energies.

E_C - 182 mV Level

$$e_n = 3.6 \times 10^{11} (T/300)^2 \exp(-182 mV/kT)$$

E_C - 470 mV Level

$$e_n = 5.6 \times 10^{13} (T/300)^2 \exp(-470 mV/kT)$$

E_V + 336 mV Level

$$e_p = 1.1 \times 10^{11} (T/300)^2 \exp(-336 mV/kT)$$

At this earlier date, it was fairly certain that the two shallow levels, E_C-182 and E_V+336 were associated with Ti and the data were fairly accurate. The data for the deeper level, E_C-470, were not as accurate and there were some doubts concerning its origin, especially if it is associated with surface traps since the Schottky barrier diode was made on a p-type silicon surface.

(B) The next sets of data were reported by Monsanto in their final report of a JPL contract, completed in September 1976 [4] but not distributed until late 1978. There was no capacitance transient measurements reported on their impurity doped silicon crystals. Impurity concentrations were determined by microanalysis techniques and lifetimes were determined by photoconductive decay and the open-circuit voltage decay measurements. These provided some indications of the minority carrier capture rates at the Ti levels in the p-type and n-type silicon. However, the lifetimes and the capture rates were not and could not be correlated with the specific Ti deep levels since no energy level measurements were available to the Monsanto group before the end of the contract.

(C) The next sets of data were reported by Northrop in their final report covering a contract from December 1976 to October 1977 but it was not

distributed until December 1978 [5]. In this work, the diffusion length of the minority carriers was measured on the impurity doped silicon wafers from Monsanto and Westinghouse/Dow-Corning, using a scanning electron microscope which gave very accurate, and we believe, rather reliable data. The minority carrier lifetimes were then computed from $L=\sqrt{D\tau}$ where L is the diffusion length measured and D is the diffusivity computed from $D=(kT/q)\mu$ using the published mobility of electrons and holes in silicon, μ_n and μ_p. The diffusion-length lifetime data were also correlated with the photoconductive decay and open-circuit voltage decay lifetimes obtained by Northrop as well as reported by Monsanto and Westinghouse on their impurity-doped silicon crystals. This correlation curve was the basis for calculating the minority carrier capture rates at the Ti levels to be presented in subsection E by us. Again, no correlation of the lifetime data were made with the specific Ti levels since reliable and accurate Ti level information were not available at that time.

(D) The next set of data on the thermal activation energies as well as the thermal emission and capture rates of electrons and holes were reported by Westinghouse in their 11-th Quarterly Contract Report in July, 1978 [11]. Measurements were made for many impurities using the VSCTS (Voltage Stimulated Capacitance Transient Spectroscopy). It is also known as DLTS - Deep Level Transient Spectroscopy or JTS - Junction Transient Spectroscopy but DLTS and JTS are all inclusive names for all the possible variations first reported by Sah and his graduate students [2] and reviewed by Miller, Lang and Kimerling [3], while VSCTS is a specific member of the DLTS or JTS family. There were considerable variations among these first atempts as revealed by the table given on the next page. Part of these were probably due to the uncertainty in the identification of the VSCTS peaks and to noise and calibration accuracy of the early instrumentation. These were mostly resolved in their later data

reported in their 16-th Quarterly Contract Report to be described in subsection (H) and in their papers to be described in subsections (F), (G) and (I).

TABLE 1 RECOMBINATION PROPERTIES AT Ti CENTERS IN Si

(Westinghouse Data, July 1978, p.110 [6])

Crystal No.	Diode Type	Energy Level (mV)	Density (cm^{-3})	Emission Cross-Section (cm^2)	Emission Rate (cm^3/sec)
W-008	m/p	E_C - 340	7.0E14	4.0E-16	4.0E-9
		E_V + 290	7.0E13	4.7E-14	4.7E-7
W-008	n/p	E_C - 260	1.5E13	?	
		E_V + 290	2.6E13	?	
W-033	?/p	E_C - 270	4.0E12	4.5E-17	4.5E-10
W-065	?/n	E_V + 450	3.6E13	3.6E-16	3.6E-09
		E_V + 250	3.0E13	1.2E-15	1.2E-08

(E) A comprehensive analysis was then made by Sah of all the published data to date and reported in March, 1979 [7]. At that time, the most accurate thermal emission and activation energy measurements were those reported by Sah and described in subsection (A). In addition, a detailed analysis was also made of all the minority carrier lifetime data reported by Westinghouse, Monsanto and Northrop. The lifetimes, corrected using the correlation curve between the diffusion length lifetime and the photoconductive and open-circuit voltage decay lifetimes were plotted as a function of the Ti concentration, either measured by the microanalysis techniques or estimated from an assumed liquid-solid segregation coefficient. The τ vs N_{Ti} data of twelve Ti-doped n-Si and p-Si from Westinghouse and four from Monsanto were plotted on the $\log\tau$ vs $\log N_{Ti}$ scale in Fig. 2. Since $\tau=(cN_{Ti})^{-1}$ or $\log\tau=-\log C-\log N_{Ti}$ where C is the thermal capture

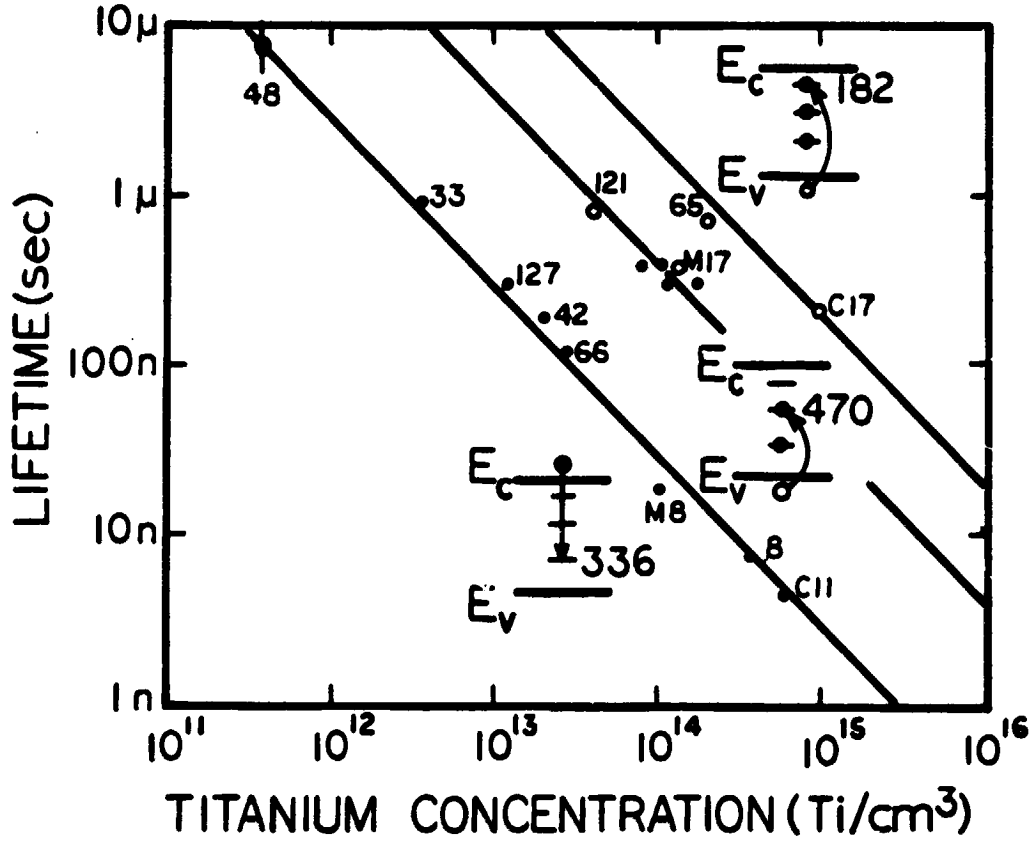

Fig. 2 The minority carrier lifetime computed from diffusion length measurements as a function of the Ti concentration from microanalysis of many p-type and n-type Si crystals doped with Ti during growth. Solid dots are p-Si and electron lifetime and circles are n-Si and hole lifetime. Numbers with character M or C in front are crystals grown by Monsanto while those without are grown by Dow-Corning/Westinghouse.

rate of the minority carriers, three best-guess lines were drawn in Fig. 2. Three lines were chosen because the points seem to group along the three lines shown in Fig. 2 and because the preliminary measurements gave three thermal activation energies as described in subsection (A). Later analysis indicated that the deep level at E_C-470 mV was due to a thermally induced center not related directly to the double donor Ti center. From these three lines, three minority carrier capture rates could be calculcated at the lifetime measurements temperature (300°K). The results [7] are summarized below.

E_C-182 Acceptor Level

$c_n = 1.3 \times 10^{-8}$ (cm^3/s)

$e_n = 3.6 \times 10^{11} (T/300)^2 \exp(-182/kT) = 3 \times 10^8$ (1/s)

$c_p = 5. \times 10^{-9}$ (Fig. 2) (cm^3/s)

$e_p = 2.2 \times 10^{-5}$ (297°K) (1/s)

E_C-470 Donor Level

$c_n = 2. \times 10^{-6}$

$e_n = 5.6 \times 10^{13} (T/300)^2 \exp(-470/kT) = 6 \times 10^5$

$c_p = 2.5 \times 10^{-8}$ (Fig. 2)

$e_p = 9.2$ (297°K)

E_V+336 Donor Level

$c_n = 3.7 \times 10^{-7}$ (Fig. 2)

$e_n = 1.6$ (297°K)

$c_p = 8.2 \times 10^{-9}$

$e_p = 1.1 \times 10^{11} (T/300)^2 \exp(-336/kT) = 2 \times 10^5$

The numerical values shown above were computed at 297°K. The two upper levels, E_C-182 and E_C-470 mV detected from minority carrier emission transients were

tentatively attributed also to the Ti center with the shallower level, E_C-182, designated as an acceptor while the deep level, E_C-470, as a donor based on the electronic shell configuration of Ti, $(Ar)3d^2 4s^2$, whose two 4s electrons are weakly bounded and can give rise to the two donor states at E_C-470 and E_V+336. It was further speculated that the shallow E_C-182 level may be the oxygen-vacancy level rather than Ti related. Later results indicate that the identification of the E_V+336 level as the second Ti donor level is correct but the first Ti donor level lies at E_C-228.65 mV instead of E_C-470 mV so that the level at E_C-182 mV was probably the second Ti donor level. The difference in energy (182 vs 228.65) was partially due to the inaccuracy of the original data analysis since it was a minority carrier transient and might have some field dependences. The data were used to compute the characteristics of Ti-doped solar cells made from the 14 Westinghouse crystals [7]. The measured and computed J_{SC}, V_{OC}, EFF were in good agreement but the agreement with the measured fill factor was poor. It was speculated that this poor agreement was probably due to a large contact resistance which was not taken into account in the theoretical transmission line equivalent circuit model. It was also noted that the agreement was good at low Ti concentrations but poor when the Ti concentration reached $4x10^{14}$ Ti/cm^3 in crystal W-008. It was suggested [7] that impurity segregation and cluster may have reduced the experimental J_{SC} and EFF. It was also noted this was the first Ti-doped Si crystal grown and its quality may have been affected by some unknown and uncontrolled growth parameters. In any case, the computer model was demonstrated to give good correlation with actual experimental solar cell data as a function of the Ti concentration, even though the recombination model was still uncertain, because the recombination parameters were accurately measured and used as the input parameter for the computer calculations. It also demonstrated that to get

a 17% AM1 efficiency cell, the Ti concentration must be less than $2.5 \times 10^{12} cm^{-3}$ and a p+/n/n+ cell structure must be used since the n+/p/p+ cell structure was less efficient because electron lifetime in Ti-doped p-Si is lower than hole lifetime in Ti-doped n-Si.

(F) The recombination properties of the Ti centers in Si were extensive and carefully investigated by many experiments carried out by Chen, et. al. at Carnegie-Mellon and reported in November, 1978 which was published in September 1979 [8]. Both Westinghouse Ti-doped Si and Ti diffused Si were used to fabricate both diffused and Schottky barrier diodes on both n-Si and p-Si. Three electron and three hole trapping levels were observed with a 40 MHz VSCT Spectrometer using double boxcar correlation technique. Two of these six levels were shown to be directly proportional to the Ti concentration and were attributed to a single Ti center. They are E_C-264 mV and E_V+290-35 mV. They were both designated as donor levels since a 360 ohm-cm n-Si was diffused by Ti and did not show acceptor or p-type conversion. The other four levels were attributed to thermal generation at high diffusion temperature or unintentionally incorporated impurities during processing.

Detailed majority carrier capture rates were also measured which indicated that hole capture into the second Ti donor level, E_V+290 mV was thermally activated with an activation of 35 mV. This gave an effective thermal activation energy of holes of E_V+290-35=E_V+255 mV.

Hall effect measurements were also carried out for the n-Si sample giving a electron activation energy of E_C-220 mV instead of the E_C-264 mV determined by VSCTS method. The capture rates and cross sections at 300°K are $\sigma_{nc}=3.5 \times 10^{-15}$ cm^2 and $c_n=3 \times 10^{-8}$ cm^3/s for the first donor level at E_C-264 mV and $\sigma_{pc}=1.7 \times 10^{-17}$ cm^2 and $c_p=2 \times 10^{-10}$ cm^3/s for the second donor level at E_V+255 mV.

Unfortunately, detailed least-squares-fit results of the emission rate data were not given and only a graphic comparison could be made with earlier and subsequent and more accurate data.

(G) More detailed capacitance transient measurements were made by Westinghouse and these were reported in three publications, a paper in the Solid State Electronics Journal [9], their 17-th Quarterly Contract Report [10], and a IEEE Transaction on Electron Devices Journal article [11]. The two levels identified by Chen as those from Ti are now reported also by Westinghouse who also gave values for the majority carrier capture rates in two of these references. These were $\sigma_{pc}=5.3\times10^{-18}cm^2$ or $c_p=5.3\times10^{-11}cm^3/s$ at the E_V+300 mV level [10] and $\sigma_{nc}=1.04\times10^{-14}cm^2$ or $c_n=1.04\times10^{-7}cm^3/s$ at the E_C-260 mV level and $\sigma_{pc}=8.3\times10^{-16}cm^2$ or $c_p=8.3\times10^{-9}cm^3/s$ at the E_V+300 mV level. These values were self-inconsistent (for example, $\sigma_{pc}=5.3\times10^{-18}cm^2$ and $8.3\times10^{-16}cm^2$ or a factor 156.6 different) and they were different from those given by Chen which was described in sub-section (E). The values given by Chen are considered more reliable.

(H) The Ti levels were also measured by a JPL in-house group [12] using solar cells fabricated by Westinghouse on the Dow-Corning Ti-doped p-type Si. Measurements were made on either mesa or photo lithographically etched n+/p diodes. The VSCTS data showed three majority carrier peaks and one minority carrier peak, at E_V+0.18, E_V+0.27, E_V+0.37 and E_C-0.24 eV. Only the E_V+0.27 level appears in the original wafer while the other appears after high temperature diode or cell diffusion. The other levels were attributed to Titanium-Oxygen complexes since titanium is highly electronegative. This model is similar to the Aluminum-Oxygen complex which was observed in Al-doped silicon [13].

(I) More extensive capacitance transient spectroscopy was also obtained [14] by Cheng and Leung in a JPL in-house work using the Westinghouse Ti-doped p-Si materials and solar cells as well as silicon ribbons, by the web dendritic process (Westinghouse) and edge-defined-growth process. The results are $\sigma_n = 5 \times 10^{-12}$ cm^{-2} and $\sigma_p = 5.5 \times 10^{-18}$ cm^{-2} for the E_V+280 mV Ti level at 200K. They also reported an estimate for the E_C-240 mV of $\sigma_e > 4 \times 10^{-15}$ cm^2.

(J) We have carried out extensive and highly accurate measurements of the thermal emission rates and activation energies of trapped majority carriers at the Ti levels in n-type and p-type Si prepared by Westinghouse/Dow-Corning as well as Ti-doped Si diffused and Schottky Barrier diodes provided by Westinghouse. These results are summarized below.

$\underline{E_V + 305 \text{ mV}}$

$$e_p = 5.45 \times 10^{11} (T/300)^2 \exp[-305.34/kT] \quad \text{(1/sec)} \qquad (1)$$

where the reduced chi square is 1.036 and the rms deviation of the two constants are 5.45±1.13 and 305.34±2.31. The large uncertainty in the pre-exponential factor was due to the small number of temperatures (nine). The results are accurate since the rms deviation of the emission rate is only 1.99%.

$\underline{E_C - 231 \text{ mV}}$

$$e_n = 1.42 \times 10^{10} (T/300)^2 \exp[-231.34/kT] \quad \text{(1/sec)} \qquad (2)$$

where the reduced chi square is 0.73 and the rms deviation of the two constants are 1.42±0.080 and 231.34±0.54. The results are quite accurate and has a rms deviation of only 1.16%. The capacitance decay curves were taken at thirteen temperatures in the range of 101.60 to 121.81K.

The thermal capture rate measurements have not been obtained for all of the electron and hole transitions. The majority carrier capture rates can be

obtained by partial-trap-filling experiments over a wide range of temperatures below the maximum temperature where the thermal emission becomes too fast to be measured by the capacitance meter. Above this temperature, current transient must be monitored under partial-trap-filling. The minority carrier capture rates were measured either by injecting minority carriers into the space charge region so that they can be captured to give a junction transient or by junction current switching transient. Thus far, measurements are made on the hole capture rate at the second donor level, E_V+305 mV, using the technique of partial-trap-filling by majority carriers. The data of our experiments as well as those of others are given in Table 2 and plotted in Fig. 3.

It is evident that there are wide disagreements among the hole capture rate data given by Westinghouse's two reports and Carnegie-Mellon as noted earlier. Our data at much lower temperatures than those of Carnegie-Mellon appear to lie on a reasonably smooth curve in Fig. 3. There are some spreads in our data taken on different diodes which are illustrated in Fig. 3 where the data symbols are indicated in Table 2. ◉ are for the diffused n+/p diode TiP152D1; ◭ are for the Schottky barrier diode TiP137S1; and ◭ are for the Schottky barrier diode TiP152S1. The following results are evident. (1) c_p is the lowest in the Schottky barrier diode, TiP137S1 (◭) which has the highest boron concentration among these three diodes (4.69×10^{15} boron/cm^3). (2) c_p is higher in the SB diode TiP152S1 (◭) than in the diffused n+/p diode TiP152D1 (◉). (3) All three sets of data of c_p from our measurements are higher than the values extrapolated from the Carnegie-Mellon-Westinghouse high-temperature data (●).

One important point to note is that the thermal activation energies and emission rates of our three diodes were all nearly equal to each other, assuring that the capture measurements were at the same Ti center.

Table 2 Hole Capture Rate at Ti Center in p-Si

Diode No.	Temperature (K)	1000/T	c_p (cm^3/sec)	Source of Data - Comments
TiP152D1 (n+/p)	77.01	12.98	1.620E-11	This work. ◎ in Fig.3. $N_{AA}=5.96\times10^{14}$ cm^{-3}
	90.00	11.11	2.477E-11	
	99.66	10.03	3.018E-11	
	109.99	9.092	3.608E-11	
	128.92	7.757	4.733E-11	
	136.95	7.302	5.373E-11	
	144.95	6.900	5.505E-11	
TiP137S1 (m/p)	109.82	9.106	2.532E-11	This work. ◭ in Fig.3. $N_{AA}=4.69\times10^{15}$ cm^{-3}
	129.05	7.749	3.617E-11	
	136.75	7.313	4.434E-11	
	144.90	6.901	5.454E-11	Large series resistance prevented low temperature measurements.
TiP152S1	77.01	12.98	1.931E-11	This work. ◭ in Fig.3.
	109.87	9.102	4.593E-11	
	144.98	6.898	6.010E-11	
Diffused & Schottky	179.89	5.559	0.761E-10	Chen-Milnes-Rohatgi [8]. ● in Fig.3. Read off the figure from [8] as accurately as possible.
	196.14	5.098	0.957E-10	
	201.90	4.953	1.03 E-10	
	213.80	4.677	1.17 E-10	
	221.43	4.516	1.29 E-10	
	241.66	4.138	1.54 E-10	
	250.25	3.996	1.68 E-10	
	?		8.3 E-09	Westinghouse [11].
	?		5.29 E-11	Westinghouse [10].
	200	5.000	5.05 E-11	JPL Cheng-Leung [14].

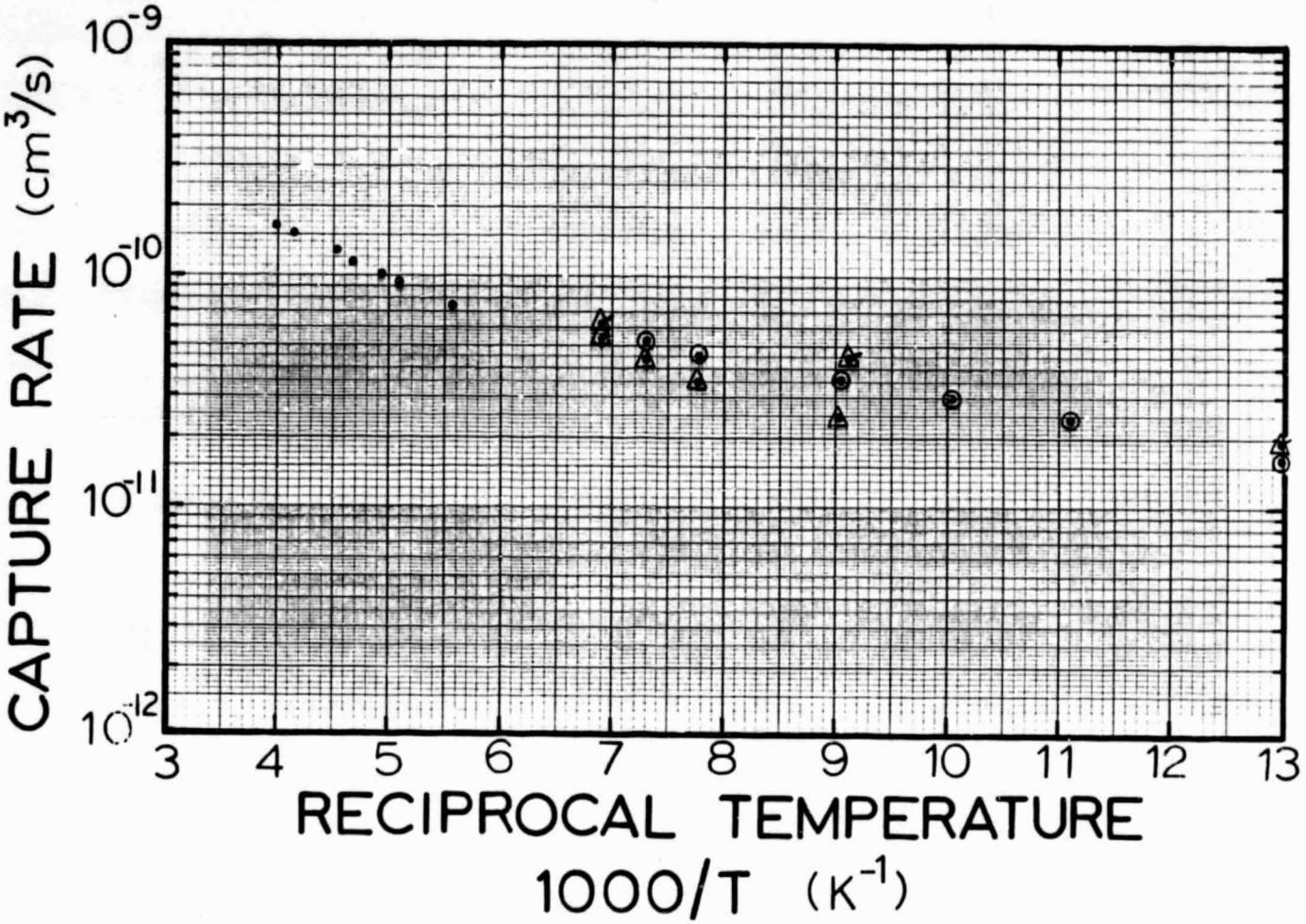

Fig. 3 Temperature dependence of the hole capture rate at the second Ti donor level, E_V+305 mV, in p-type silicon.

The capture rate plotted in Fig. 3 is the quantity measured directly from the experiment. The data presented by Chen-Milnes-Rohatgi in the Carnegie-Mellon paper [8] was given as capture cross section. A conversion back to the capture rate required the use of an thermal velocity expression for holes since it is temperature dependent. The rms velocity, $\theta_p=\sqrt{3kT/m_p}$, is used where m_p is the density-of-state effective mass of the valence band. m_p is slightly temperature dependent and is computed using $m_p/m = 0.64742[1+(T/193.472)^3]x[1+(T/142.739)^3]/\{[1+(T/202.056)^3][1+(T/166.785)^3]\}$. The capture rate is computed from the measured filling time constant using $c_p=(P\tau_f)^{-1}$ where τ_f is the filling time constant and P is the hole concentration. Deionization correction is also made to compute P from the boron concentration, N_{AA} which is measured from C^{-2} vs V at 300K. The formula for computing P is $P = 2N'_{AA}/[1+\sqrt{1+4N'_{AA}/K_A}]$ where $K_A=(N_V/g_A)\exp[-(E_A-E_V)/kT]$, $N'_{AA}=N_{AA}-N_{Ti}$ and $N_V=2.51x10^{19}(T/300)^{3/2}(m_p/m)^{3/2}$. $E_A-E_V=0.0444$ eV and $g_A=2$ are assumed. The deionization correction is significant but not very large.

If a line is drawn through these data, a rough or poor fit can be made to give a Arrhenius equation for the hole capture cross section which is

$$\sigma_{pc} = 6.2x10^{-17} \exp[-34.85/kT] \quad cm^2 \tag{3}$$

This would change the thermal activation energy for hole emission by 34.85 mV.

The electron capture rate has not been measured because it is very large and the filling time required is below 10 ns making it impossible to perform the partial filling experiment due to pulse shape distortion by the loading of the Ti-doped diode. This filling time can be increased substantially if the resistivity of the Ti-doped n-type Si crystal is increased. At 30 ohm-cm, the hole concentration will be sufficiently low to allow for accurate measurements but high resistivity Ti-doped n-type silicon crystal is not available.#

It became available after the completion of the draft of this technical report.

3. THEORETICAL ANALYSIS

Although the complete set of four capture rates at the two Ti levels have not been obtained, the data on hand for the majority carrier capture rates can be used to delineate the electronic models and the charge states of the Ti levels in p-type and n-type silicon. This is possible by noting that at thermal equilibrium, the emission and capture rates are related by the mass action law. For holes trapped at the lower Ti level, this is

$$e_p = c_p N_V \exp[-(E_T-E_V)/kT] = \sigma_p \theta_p N_V \exp[-(E_T-E_V)/kT] \quad (4)$$

and

$$e_n = c_n N_C \exp[-(E_C-E_T)/kT] = \sigma_n \theta_n N_C \exp[-(E_C-E_T)/kT] \quad (5)$$

where we have used the definitions for the cross sections given by

$$c_p = \sigma_p \theta_p \quad (6)$$

and

$$c_n = \sigma_n \theta_n. \quad (7)$$

Here, $\sigma_p=\sqrt{3kT/m_p}$ and $\sigma_n=\sqrt{3kT/m_n}$ are the rms velocity of the holes and electrons respectively whose effective masses are m_p and m_n. In our previous data conversion, we have employed the density-of-state effective masses, m_P and m_N.

In the experiments of majority carrier capture and emission, such as holes at the lower Ti level, E_V+305 mV, both e_p and c_p can be measured independently but they are measured under drastically different conditions. The emission transient and rate is due to the thermal emission of the trapped carriers from the Ti centers in the junction space-charge region where there is a high electric field and hence it is a highly non-equilibrium process. The capture transient and rate is due to the thermal capture of carrier by the Ti centers in the quasi-neutral region and hence it is an equilibrium process. Because emission is not at thermal equilibrium, we define a separate emission cross section to distinguish it from the capture cross section. Thus, the four equations for the

four experimental measurements are

$$e_p = \sigma_{pe}\theta_p N_V \exp[-(E_T-E_V)/kT] \tag{8}$$

$$c_p^\circ = \sigma_{pc}^\circ \theta_p \tag{9}$$

$$e_n = \sigma_{ne}\theta_n N_C \exp[-(E_C-E_T)/kT] \tag{10}$$

and

$$c_n^\circ = \sigma_{nc}^\circ \theta_n \, . \tag{11}$$

which give four experimentally determinable cross sections, σ_{pe} and σ_{pc}° for holes and σ_{ne} and σ_{nc}° for electrons where the superscript $^\circ$ denotes equilibrium.

In addition to the equilibrium-nonequilibrium difference, the two cross sections for holes (or electrons) are also related through a factor which depends on the nature of the charge state or impurity potential which determines the spectrum of excited bound states, their spin and configuration degeneracy, as well as a configuration entropy due to lattice relaxation around the impurity. We shall develop or summarize these theoretical results which relates σ_{pe} to σ_{pc} and σ_{ne} to σ_{nc}. Thus, the experimental data can be used to determine which theoretical model is consistent with the measurements which would then allow a determination of the charge state or the impurity potential.

We shall first obtain the complete expression for the emission rate at thermal equilibrium in terms of the thermal equilibrium capture rate or cross section for a donor impurity level. Suppose that the donor impurity has five valence electrons with a ground state energy level at E_C-E_D and a degeneracy of g_D. Then, from the equilibrium mass action law or from balancing the electron emission and capture transition rates, $e_n^\circ N_D = c_n^\circ N P_D \equiv c_n^\circ N(N_{DD}-N_D)$ and using the equilibrium distribution function for the trapped electrons [15]

$$N_D = N_{DD}/\{1+g_D^{-1}\exp[-(E_F-E_C)/kT]\} \tag{12}$$

and the electron concentration given by

$$N = N_C \exp[-(E_C-E_F)/kT] \tag{13}$$

we have

$$e_n^\circ = c_n^\circ g_D^{-1} N_C \exp[-(E_C-E_F)/kT] \tag{14}$$

$$= (\sigma_{nc}^\circ/g_D)\theta_n N_C \exp[-(E_C-E_F)/kT] \tag{15}$$

Comparing the non-equilibrium experimental relationship, (10), with the theoretical equilibrium relationship, (14), we can write

$$\sigma_{nc}^\circ/\sigma_{ne} = g_D e_n^\circ/e_n = g_D/r_n \tag{16}$$

where $r_n \equiv e_n/e_n^\circ \geq 1$ since the emission rate in a high field will be larger due to binding potential barrier lowering and tunneling. For this donor impurity, the hole emission and capture cross sections are related by

$$\sigma_{pc}^\circ/\sigma_{pe} = (g_D e_p/e_p^\circ)^{-1} = (g_D r_p)^{-1} \tag{17}$$

where $r_p \equiv e_p/e_p^\circ \geq 1$.

A similar derivation can be made for an acceptor impurity level whose ground state has a g_A-fold degeneracy. The results for the acceptor impurity are different than those for the donor impurity given by (16) and (17) since holes are trapped at the acceptor level while electrons are trapped at the donor level. The cross section ratios at an acceptor level are given by

$$\sigma_{pc}^\circ/\sigma_{pe} = g_A/r_p \tag{18}$$

and

$$\sigma_{nc}^\circ/\sigma_{ne} = (g_A r_n)^{-1}. \tag{19}$$

If we take into account of the excited states and their degeneracy, then the degeneracy factor, g_D, must be replaced by a sum-over-state [15,16] given by

$$g_D = g_{D1} + g_{D2}\exp[-(E_{D2}-E_{D1})/kT] + g_{D3}\exp[-(E_{D3}-E_{D1})/kT] + \ldots. \tag{20}$$

where g_{Di} and E_{Di} $(i=1,2,3,\ldots)$ are the degeneracy and energy level of the i-th excited state. The ground state is i=1.

The different dependences of the capture-emission cross section ratio of a donor and an acceptor impurity, given by (16) and (17) for a donor and (18) and (19) for a acceptor, makes it possible to distinguish them from experimental measurements of the cross sections from the capacitance transient experiments. To demonstrate this possibility, we take the simplest situation in which there is no electric field dependence of the emission rate so that $r_n = r_p = 1$. Then, we have

Donor Level (Electron Trap)

$$\sigma^\circ_{nc}/\sigma_{ne} = g_D/r_n \leq g_D \geq 2 \tag{21}$$

$$\sigma^\circ_{pc}/\sigma_{pe} = (g_D r_p)^{-1} \leq g_D^{-1} \leq 1/2 \tag{22}$$

Acceptor Level (Hole Trap)

$$\sigma^\circ_{nc}/\sigma_{ne} = (g_A r_n)^{-1} \leq g_A^{-1} \leq 1/2 \tag{23}$$

$$\sigma^\circ_{pc}/\sigma_{pe} = g_A/r_p \leq g_A \geq 2 \tag{24}$$

These sets of equations show that the experimentally determined ratio of the capture to emission cross section will make it possible to determine if the level is a donor level or an acceptor level.

Let us apply the above result to the measurements made on the Ti levels. From the hole emission rate at E_V+305 mV given by (1), the hole emission cross section at 300°K is $\sigma_{pe} = 2.67 \times 10^{-15}$ cm^2. The hole capture cross section calculated from (3) is $\sigma^\circ_{pc} = 1.6 \times 10^{-17}$ cm^2. The ratio is $\sigma^\circ_{pc}/\sigma_{pe} = 1/167 = 0.006$. Thus, this lower Ti level must be a donor level. The small ratio indicates that $r_p = e_p/e^\circ_p \gg 1$ since g_D in (22) cannot be substantially greater than about 2. Part of this large ratio is due to electric field dependence but configuration entropy due to strong electron-phonon coupling and lattice distortion is likely to contribute. If it is due entirely to the latter, the entropy is $k \log_e 166 = 5k$ which is not unreasonable.

A similar calculation may be made for the electron emission rate at E_C-231 mV given by (2). The emission cross section at 300°K is $\sigma_{ne}=4.46\times10^{-17}cm^2$. The electron capture rate and cross section have not been measured in the Ti-doped n-Si but it has been measured in n-Si where Ti was introduced by diffusion. This was reported by Chen-Milnes-Rohatgi [8] to be a constant from 150 to 210°K with a value of $\sigma^\circ_{nc}=3.5\times10^{-15}$ cm^2. Using this value, the ratio is then $\sigma^\circ_{nc}/\sigma_{ne}=78.4$. Comparison with (21) to (24) shows that this Ti level must also be a donor level.

Thus, from the emission and capture cross section measurements of majority carriers at the two Ti level, we can conclude without doubt that the two Ti levels are donors. The most likely possibility is that Ti is a double donor with charge states 0, +1 and +2 and the upper level, E_C-231 mV the first donor level and the lower level, E_V+305 mV the second donor level.

The large ratios of the capture to emission cross sections suggest that there is considerable lattice relaxation from strong electron-phonon interaction since electron spin and electron configuration degeneracy cannot account for such large ratios neither can electric field enhancement of the hole emission rate at the lower level. Electric field enhancement of the electron emission rate at the upper level would give the wrong change since it would increase r_n or e_n/e°_n and make the $\sigma^\circ_{nc}/\sigma_{ne}$ ratio even smaller.

The conclusion here that the two Ti levels are donor-like are consistent with the conductivity-type conversion experiment of Chen-Milnes-Rohatgi in which they find no conversion of a 320 ohm-cm n-Si diffused with Ti, implying that all Ti levels must be donor like. The recombination coefficient measurements given here not only determines whether Ti is donor or acceptor but also provide additional indication that strong electron-phonon interaction occurs around the Ti impurity site to give a large configuration entropy.

The conclusion about the double donor nature of the Ti impurity in Si gives further support to the valence bond model. The electronic shell structure of Ti is $[(Ar)3d^2 4s^2]$ The radii of the two 4s electrons are large, 1.477A, compared with one-half of the nearest neighbor silicon spacing (2.35/2=1.17A). Thus, these two 4s electrons of the Ti atom are loosely bound in the Si crystal lattice and they are easily released to produce two bound states, the E_C-231 and the E_V+305 mV levels.

The electron capture cross sections and rates at these two donor levels are expected to be large due to attractive Coulomb potential. On the other hand, hole capture cross sections are expected to be small due to the repulsive Coulomb potential. Thus, the electron lifetime in p-Si should be considerably shorter than hole lifetime in n-Si, making the p+/n/n+ silicon solar cell containing Ti likely to have higher efficiency than the n+/p/p+ type. This was verified by computer design simulation [7].

A similar conclusion on solar cell efficiency can also be reached for the vanadium recombination center which is a double donor in silicon and other double donor recombination centers whose two levels are located in the two different halves of the silicon energy gap.

4. REFERENCES

1. C. T. Sah, P. C. H. Chan, C. K. Wang, R. L. Y. Sah, K. A. Yamakawa and R. Lutwack, "Effect of Zinc Impurity on Silicon Solar-Cell Efficiency," IEEE Transaction on Electron Devices, ED-28, 304-313, March 1981.
2. C. T. Sah, L. Forbes, L. L. Rosier, and A. F. Tasch, Jr., "Thermal and Optical Emission and Capture Rates and Cross Sections of Electrons and Holes at Imperfection Centers in Semiconductor from Photo and Dark Junction Current and Capacitance Experiments," Solid-State Electronics, 13, 759-788, June 1970.
3. G. L. Miller, D. V. Lang and L. C. Kimerling, "Capacitance Transient Spectroscopy," Annual Review of Material Science, 7, 377-348, 1977.
4. Henry W. Gutsche and Dale E. Hill, Determination of a Definition of Solar Grade Silicon," Final Report, ERDA/JPL 954338-76, October 1975 to September 1976. Monsanto Reserach Corporation, St. Peters, MO 63376.
5. Siegfried Othmer and Susan C. Chen, "Lifetime and Diffusion Length Measurements on Silicon Materials and Solar Cells," Final Report, ERDA/JPL 954614-77/1, December 16, 1976 to October 31, 1977, Northrop Research and Technology Center, Palos Verdes Pennsylvania, CA.
6. R. H. Hopkins, J. R. Davis, P. D. Blais, A. Rohatgi, P. Rai-Choudhury, M. H. Hanes and J. R. McCormick, "Effect of Impurities and Processing on Silicon Solar Cells," 11-th Quarterly Report, DOE/JPL-954331-78/3, July, 1978
7. C. T. Sah, "Study of the Effects of Impurities on the Properties of Silicon Materials and Performance of Silicon Solar Cell," Second Technical Report, DOE/JPL-954685-79/1, March 1979.
8. J. W. Chen, A. G. Milnes and A. Rohatgi, "Titanium in Silicon as a Deep Level Impurity," Solid-State Electronics, 22, 801-808, September 1979.
9. A. Rohatgi, J. R. Davis, R. H. Hopkins, P. Rai-Choudhury, P. B. McMullen and J. R. McCormick, "Effect of Titanium, Copper and Iron on Silicon Solar Cells," Solid-State Electronics, 23, 415-422, 1980.
10. R. H. Hopkins, J. R. Davis, et. al. "Effects of Impurities and Processing on Silicon Solar Cells, Volume 2: Analysis of Impurity Behavior," 17-th Quarterly Report, DOE/JPL-954331-80/9, January 23, 1980.
11. J. R. Davis, Jr.,A. Rohatgi, R. H. Hopkins, P. D. Blais, P. Rai-Choudhury, J. R. McCormick and H. C. Mollenkoph, "Impurities in Silicon Solar Cells," IEEE Trans. ED-27, 677-687, April 1980

12. A. M. Salama and L. J. Cheung, "The Effects of Titanium Impurities in n+/p Silicon Solar Cells," J. Electrochemical Soc. 127, 1164-1167, May 1980.

13. R. Marchand and C. T. Sah, "Studies of Thermally Induced Deep Levels in Al-doped Silicon," J. Applied Physics 48, 336-341, January 1977. R. Marchand, A. R. Stivers and C. T. Sah, "Recombination Centers in Aluminum-Doped Silicon Diffused in High Phosphorus Concentration," J. Applied Physics, 48, 2576-2580, June 1977.

14. L. J. Cheng and D. C. Leung, "Deep Levels in Impure Silicon," Proc. Sumposia on Electronic and Optical Properties of Polycrystalline or Impure Semiconductor and Novel Silicon Growth Methods," Edited by K. W. Ravi, R. O'Mara, Volume 80-5, 46-56, 1980, The Electrochemical Society, Inc. Pennington, NJ 08543.

15. William Shockley, ELECTRONS AND HOLES IN SEMICONDUCTORS, Chapter 10, 1950, d. Van Nostrand Co. Inc. New York, NY.

16. C. T. Sah and W. Shockley, "Electron-Hole Recombination Statistics in Semiconductors Through Flaws with Many Charge Conditions," Physical Review, 109, 1103-1115, February 15, 1958.